Localized and disease-selective drug delivery using adhesive hydrogels for treatment of locally advanced TNBC

by

Nuria Oliva Jorge

B.S., Institut Quimic de Sarria, Barcelona (2009)

Submitted to the Department of Health Sciences and Technology
in Partial Fulfillment of the Requirements for the degree of

Doctor of Philosophy

at the

MASSACHUSETTS INSTITUTE OF TECHNOLOGY

June 2016

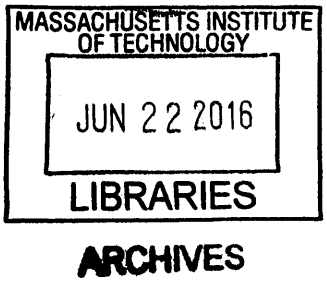

Signature of the author Signature redacted
Department of Health Sciences and Technology, IMES
May 10, 2016

Certified by Signature redacted
Elazer R. Edelman
Thomas D. and Virginia W. Cabot Professor of Health Sciences and Technology
Thesis Supervisor

Certified by Signature redacted
Natalie Artzi
Assistant Professor of Department of Medicine, HMS
Thesis Supervisor

Accepted by Signature redacted
Emery N. Brown, MD, PhD
Director, Harvard-MIT Program in Health Sciences and Technology
Professor of Computational Neuroscience and Health Sciences and Technology

Localized and disease-selective drug delivery using adhesive

hydrogels for treatment of locally advanced TNBC

by

Nuria Oliva Jorge

Submitted to the Department of Health Sciences and Technology

on May 16, 2016 in Partial Fulfillment of the requirements for the

Degree of Doctor of Philosophy

ABSTRACT

Triple negative breast cancer (TNBC) is an aggressive form of cancer that represents 20% of invasive breast cancers, and about 15% are locally advanced at time of presentation. TNBC is negative for estrogen and progesterone receptor, as well as for HER2, and hence it is not treatable with common endocrine treatment such as tamoxifen or Herceptin. Systemic neoadjuvant therapy has been established as the preferred therapeutic approach for locally advanced breast cancer, downstaging the disease and preventing mastectomy. However, complications of systemic chemotherapy are devastating. Local therapy would prevent high concentrations of circulating drug and reduce off-target tissue retention. Yet, the means to attain ideal release kinetics and selective uptake remain elusive.

I developed a novel class of biocompatible and biodegradable adhesive materials based on dendrimer and dextran that can coat the tumor and locally release doxorubicin in a controlled manner. Doxorubicin was conjugated to the dendritic component of the adhesive hydrogel to form a pro-drug capable of being released over time as the hydrogel degrades at a pre-programmed rate. The pro-drug was further modified with a ligand capable of sensing and discerning between healthy and cancer cells and facilitating uptake through receptor-mediated endocytosis (RME). The platform developed herein provides a paradigm shift in the way we treat cancer, in a local, selective and targeted manner, to impart optimal clinical outcome.

Thesis supervisors:
Elazer R. Edelman, MD, PhD
Title: Thomas D. and Virginia W. Cabot Professor of Health Sciences and Technology, MIT
Natalie Artzi, PhD
Title: Assistant Professor of Medicine, Brigham and Women's Hospital, HMS

Para ti, yaya – tu lucha me inspira y da fuerzas. Esta tesis es para Ti.

Table of Contents

BIOGRAPHICAL NOTE

Nuria Oliva Jorge graduated from Institut Químic de Sarrià (Barcelona, Spain) in 2009 with a B.S. in Organic Chemistry. After graduation, she joined the Artzi's group as part of the Edelman Lab as a Visiting Graduate Student, and started her Ph.D. in Medical Engineering and Medical Physics (MEMP) at the Harvard-MIT Division of Health Sciences and Technology (HST) within the Institute of Medical Engineering and Sciences (IMES) in 2011. She focused her Ph.D. on developing a novel class of adhesive hydrogels based on dendrimers and dextrans, and on utilizing them as a model platform to show how material performance and hence patient outcome are altered by tissue microenvironment in the settings of disease. She also studied how the cues of disease microenvironment can be leveraged to attain selective delivery of chemotherapeutic agents to cancer cells through rational material design and optimization for the treatment of locally advanced triple negative breast cancer. Some selected publications include:

1. J Conde, **N Oliva**, M. Atilano, HS Song and N Artzi. Self-assembled RNA triple-helix hydrogel scaffold for micro-RNA modulation in the tumor microenvironment. **Nat Mat** 15, 353 (2015).
2. **N Oliva**, S Unterman, Y Zhang, J Conde, HS Song, N Artzi. Personalizing Biomaterials for Precision Nanomedicine Considering the Local Tissue Microenvironment. **Adv Healthc Mat** 4(11), 1577. (Cover article, 2015).
3. J Conde, **N Oliva** and N Artzi; Implantable hydrogel embedded dark-gold nanoswitch as a theranostics probe to sense and overcome cancer multidrug resistance. ***PNAS*** 112(11), 1278 (2015).
4. **N Oliva**, M Carcole, M Beckerman, S Seliktar, A Hayward, J Stanley, NMA Parry, ER Edelman and N Artzi. Regulation of dendrimer/dextran material performance by altered tissue microenvironment in inflammation and neoplasia. ***Sci Transl Med,*** 7(272), 272ra11 (Cover article and Focus article, 2015).
5. N Segovia, M Pont, **N Oliva**, V Ramos, S Borros, N Artzi; Hydrogel Doped with Nanoparticles for Local Sustained Release of siRNA in Breast Cancer. ***Adv Healthc Mat,*** 4(2), 271 (2014).
6. **N Oliva**, S Shitreet, E Abraham, B Stanley, ER Edelman and N Artzi; Natural tissue microenvironmental conditions modulate adhesive material performance. **Langmuir**, 28(43), 15402 (2012).
7. N. Artzi, **N. Oliva**, C. Puron, S. Shitreet, A. Groothuis, A. Bon Ramos, G. Sahagian and E.R. Edelman; In vivo and in vitro tracking of erosion in biodegradable materials using non-invasive fluorescence imaging. **Nat Mat**, 10, 704 (2011).

ACKNOWLEDGEMENTS

Firstly, I would like to express my sincere gratitude to my advisors Prof. Edelman and Prof. Artzi for their continuous support of my Ph.D study and related research, for their patience, motivation, and immense knowledge. Prof. Edelman's guidance helped me in all the time of research and writing of this thesis. And Prof. Artzi, you have been a tremendous mentor for me, encouraging my research and allowing me to grow as a research scientist. At a personal level, you both have always been there when things have been difficult, and I cannot thank you enough for making me feel part of a family despite being so far from home. I could not have imagined having better advisors and mentors for my Ph.D. study.

Besides my advisors, I would like to thank the rest of my thesis committee: Prof. Bhatia and Prof. Anderson, for their insightful comments and encouragement, and for taking the time to be part of my Ph.D. project. It has been a very enlightening experience and I deeply appreciate your efforts.

I would also like to take the opportunity to thank my former advisor in Spain, Prof. Borrós, for believing in my potential and for giving me the opportunity to come to MIT in the first place – my scientific career started thanks to the trust he placed in me.

I'd like to thank the students and fellow lab mates that have been part of this project at different stages of it: Joao, Nathaly, Maria, Sivan, Rita, Mariana, Mario and Shani, for working hard, for contributing with stimulating discussions and great ideas, and for all the fun we have had in the last five years. I gained great collaborators and lifelong friends for the future to come. Also I thank my fellow lab mate and friend Farhad for simply being there when I needed focus and perspective.

Last but not the least, I would like to thank my family. First and most importantly my parents for giving up everything to support my career and make sure I achieved my goals. They are the living example of sacrifice and unconditional love, and I simply cannot thank them enough. Second, my husband and best friend, Tim, for supporting me every day of this journey that has been my doctorate degree. I am blessed with a partner who has been able to understand all the pressures and ups and downs inherent to this degree and has been by my side regardless. I'd also like to acknowledge the rest of my family – my grandparents, my aunts and uncles and my cousins for being a unified rock for me to lean on all these years, as well as my in-laws for blessing me with yet another family to rely on.

To all of you, thank you!

CHAPTER 1. General Introduction

Statement of the unmet clinical need

Triple negative breast cancer (TNBC) is an aggressive form of cancer that represents 20% of invasive breast cancers, and about 15% are locally advanced at time of presentation. It has been associated with younger age at diagnosis, with median age below 50 years (1). Women with TNBC experience the peak risk of recurrence within 3 years of diagnosis, and the mortality rates appear to be increased for 5 years after diagnosis (2). TNBC is negative for estrogen and progesterone receptor, as well as for HER2, and hence it is not treatable with common endocrine treatment such as tamoxifen or Herceptin. Current approaches for treatment involve neoadjuvant therapy with systemic chemotherapy, with the aim of downstaging the disease and reducing the amount of breast tissue removed (3), followed by total or partial mastectomy and several cycles of radiation and adjuvant chemotherapy. While effective, this treatment modality has deleterious side effects in the patient. As an alternative, these patients would benefit from a shift in treatment approach by delivering the same class of chemotherapy currently being used and known to be highly effective, but in a local, sustained and cancer-specific manner rather than systemically. The proposed approach would consist on the use of biodegradable adhesive hydrogels that can coat the tumor and release a pro-drug type molecule in a sustained manner over time. The pro-drug, once released from the hydrogel, would sense cancer-specific cues that could in turn trigger the uptake by these cells and elicit cancer-specific cytocidal effect. This approach will reduce chemotherapy side effects both systemically and locally, while enhancing efficient dose to the tumor and avoiding renal and hepatic clearance.

Adhesive hydrogels as drug depots for local and sustained delivery of chemotherapeutic agents

Hydrogels are three-dimensional, hydrophilic, polymeric networks that can store large amounts of water or biological fluids, a property that makes them highly biocompatible (4-6). These materials resemble natural tissues due to the large amounts of structural water and their soft consistency (5, 6). They have the ability to swell (absorb and retain water in their structure). The swelling ratio is determined by their initial degree of crosslinking, controlled by material formulation, and can be modified on demand as a response to certain stimuli, such as temperature (7, 8), pH (9-13), light (14, 15), magnetic field (16, 17), electric current (18, 19) or antigens (14, 20). Control over crosslinking density defines the mesh size, and hence the rate of passive diffusion, which are key parameters in developing a controlled drug delivery system (21). In situ polymerization enables hydrogels to be injectable, an advantage in medical applications (22-32), allowing for the use of techniques already available in a hospital setting, such as ultrasound-guided injection, avoiding open surgery and its associated complications.

A large number of hydrogels conjugated to cell adhesive molecules have been developed in the field of tissue engineering over the last decade (33-37). Their purpose was mainly to serve as biomimetic materials for three-dimensional cell growth. However, the use of hydrogels as tissue adhesives, rather than cell adhesives, is not as widely reported, but rapidly emerging. Mehdizadeh and Yang defined tissue adhesives and sealants as a "group of liquid or semi-liquid compounds that can be applied to a tissue incision with the purpose of closing wounds, adhering to soft tissues, and for hemostasis"(38). They also outlined the ideal properties that a tissue adhesive should have, including the following:

- Low toxicity, ease of preparation and sterilizability
- Low viscosity prior to application and rapid solidification on the target tissue
- Maintaining tissue adhesion post-application

- Improve hemostasis, healing and regeneration
- Degradability at a rate suitable for the application
- Non-toxic degradation by-products
- Cost-effective

Adhesion to tissues can be imparted through mechanical or chemical means. Mechanical interlocking mechanism of adhesion is based on the infiltration of the adhesive material into the pores and crevices of the adherend surface, such as bone (38). A macroscopic example that illustrates mechanical interlocking and helps visualize the mechanism is Velcro; the hooks latch onto the loops and physically hold the two materials together like an adhesive would. Chemical reactions with tissues usually provide stronger adhesion strength as the materials bind to tissue surfaces. Primary bonds (covalent, ionic or metallic), unlike secondary bonds (hydrogen bonding or Van der Waals), form strong bonds between atoms, making the adhesive less dependent on assisting mechanisms. This strong bond can also potentially damage the tissue, necessitating careful choice of basic material components and reactive groups. Tissue-material interactions must be controlled, as simply providing an excess number of reactive groups to react with tissue functional groups may impart toxicity. Hence, material formulation must be titrated to tissue type and need. It is possible to consume internally excess groups by a second material component, thus increase cohesion while eliminating toxicity (39).

The use of hydrogels as tissue adhesives is a novel and rapidly emerging field (39-44). Control over the physicochemical properties of the macromolecules that form these adhesive hydrogels dictates their adhesion and degradation. Moreover, their ability to polymerize in situ makes them injectable materials, and hence requiring minimally invasive procedures for their implantation, which can be done through a syringe needle or a catheter into a cavity (45). On the contrary, implantable materials that require open surgery, which increases tissue trauma, risk of infection

and overall morbidity (46). As the curing process of injectable materials takes place directly on the surface of the target organ, the liquid components allow for an intimate interface with more interactions, which in turn improves adhesive and mechanical properties. This is critical for uneven or curved surfaces, which are present in most organs and are accentuated in pathological states such as inflammation or neoplasia. However, injectable materials pose certain challenges in their design. First, there's a limited repertoire of chemical reactions that can take place spontaneously and in a reasonable time frame in physiological conditions, and these reactions should not harm or modify the tissue to which they adhere. Another challenge for in situ material polymerization is the toxicity of the monomers as they are in direct contact with the cells and can be uptaken or cause tissue crosslinking similar to the process observed in tissue fixation using formaldehyde or glutaraldehyde. An alternative approach to reducing toxicity is to use macromolecules with distant surface functional groups as reactive units instead of small monomeric units to form the adhesive. These macromolecules are less likely to be uptaken by cells or penetrate as deeply to the tissue due to their size, and the right distribution of chemical groups throughout their chains would prevent tight tissue crosslinking (40).

In Chapter 2, I describe the development of a novel class of highly biocompatible and biodegradable adhesive hydrogels based on dendrimer and dextran.

Leveraging cues of tissue microenvironment to allow for optimal material design

Biomaterials are increasingly used to support or reprogram their complex biological microenvironment by either providing structural stability and mechanical restoration or by serving as scaffolds for local drug release or for embedding of cells. Furthermore, materials have been functionalized with biological sequences of natural components to attract reparative endogenous cells and modulate their phenotypes (47-51). Despite the use of such materials in injured, inflamed, or diseased environments, little has been reported about the impact of disease on the

material itself and whether the material performs its intended action in selected environments. Materials with adequate efficacy in a healthy environment might demonstrate suboptimal performance and altered host-material responses in diseased settings. Although the inflammatory response to material exposure follows an orderly sequence of events, preexisting processes such as inflammation might set this order awry. The sequence of early neutrophil invasion followed by macrophage infiltration and eventually the formation of foreign-body giant cells is modified in a disease state (52). Disease alters the basal immune state, as immune cells are present at the site of injury well before any material is implanted. Such is the case of inflammatory diseases, in which the preexisting tissue reactivity might alter tissue response to a material. We envisioned that rational development of materials with optimal healing capacity can be enabled only in the context of the intended clinical use of the material and with a deep understanding of the local environment. This led to defining two key concepts: 'material dynamics' and 'material kinetics'. These roughly correspond to how the material affects the tissue and how the tissue affects the material. Material dynamics is usually studied in detail, where the therapeutic effect of a material system is evaluated to understand its biocompatibility and efficacy. However, material kinetics— understanding how the tissue microenvironment affects material properties—has long been neglected. Materials pre-programmed behavior may be altered post-implantation, as the immediate tissue milieu interacts with and modifies the material. Dissecting the features of the disease microenvironment and understanding how they vary from the normal state now defines precision medicine, where biomaterials are designed to sense and respond to disease type- and- state while providing the optimal treatment and hence improved clinical outcomes. These concepts will be supported with experimental data in Chapter 3.

For the past two decades, advances in panomics and systems biology allowed clinicians to envision personalizing the practice of medicine in a data-driven manner: drugs could be tailored precisely to the individual's condition based on their genetics and disease state. In a parallel of

drug development, materials must be evaluated based on both 'material dynamics' and 'material kinetics' in vivo and built from versatile building blocks that allow for application-specific optimization. Modular material platforms can thus be readily modified to sense and report on the dynamic local environment that would then trigger the most appropriate therapeutic outcome (Figure 1).

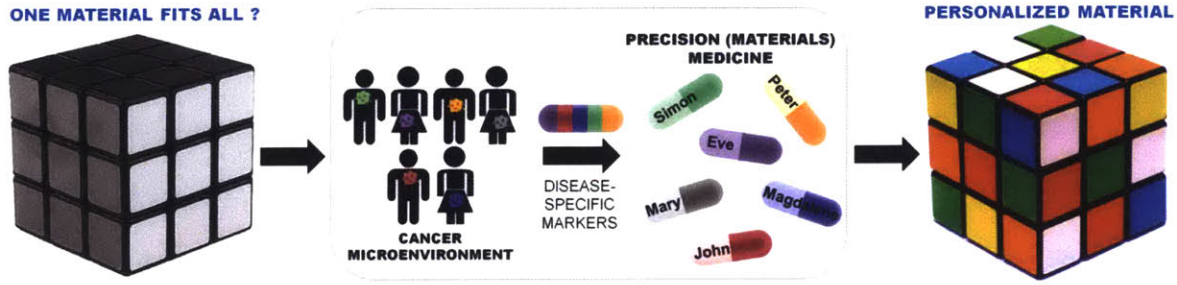

Figure 1. Materials need to be composed of building blocks capable of sensing and reporting on patient-specific disease microenvironment to allow for precision materials for medicine.

A "one material fits all" rule ignores deep variances in target tissues that affect their responses and reactivity. The complex microenvironment in vivo at different tissue sites with diverse cell types and under different pathological conditions may alter material properties and in turn, affect its in vivo performance. Physiological and pathophysiological variations between tissue types and states would affect material performance. Hence, merely characterizing the biomaterial is necessary but insufficient to fully comprehend and predict material in vivo performance. The resultant material designs must be based on flexibly tunable 'platforms' that can be modified to meet even the most-subtle changes in disease type and state (53).

Studying how the tissue microenvironment affects material properties has remained an under-explored area. In vivo microenvironments are far more complex than those utilized in vitro, hence, bench-top findings rarely predict material in vivo behavior. Tzur-Balter et al. showed that porous

silicon particles (PSi), which are increasingly used to deliver chemotherapeutics, undergo enhanced degradation in cancerous environments compared to healthy environments. Up-regulation of reactive oxygen species (ROS) by the tumor cells oxidizes the silicon scaffold (see Glossary) and catalyzes its degradation (54). The authors showed that PSi degradation profiles in vitro and in vivo correlate in the absence of a tumor in a murine model, but only correlate with tumor data when ROS-containing media is used in vitro. This work demonstrates that understanding the governing mechanisms associated with specific tumor milieu and how it might affect material properties, permits predictive in vivo performance.

The degradation kinetics of gelatin scaffolds were shown in another study to be implant site-dependent. Although gelatin scaffolds degrade enzymatically through the action of collagenases, the in vivo degradation data did not correlate with different collagenase concentrations in vitro but with the same concentration in different volumes. In vitro erosion under 25 µl diluent correlated with in vivo erosion in the subcutaneous space, while a linear relationship was obtained for intramuscular and intraperitoneal erosions when a 100 µl diluent volume was used in vitro (Figure 2). The volume of liquid surrounding the gelatin hydrogel affects swelling ratio, which in turn alters the diffusion kinetics of enzymes into the scaffold and hence the degradation kinetics in a tissue-specific manner (55).

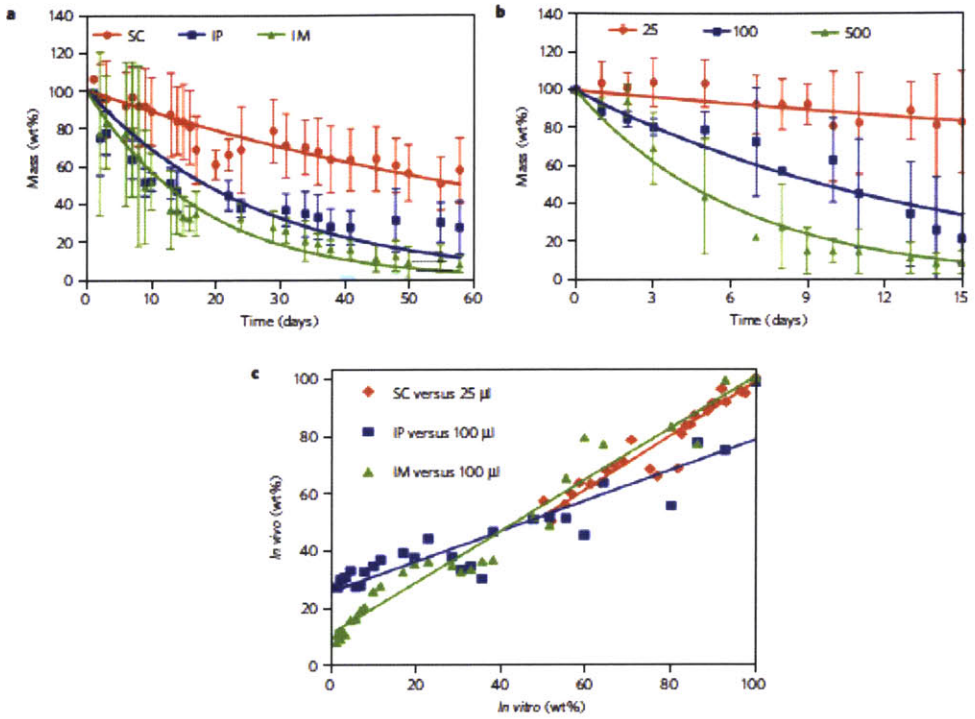

Figure 2. In vivo erosion profile is site-dependent and can be used to infer physiologically relevant in vitro conditions for enzymatic materials. (a) In vivo erosion at target sites that differ in enzyme concentration and fluid volume (Subcutaneous (SC), intraperitoneal (IP) and intramuscular (IM)) is site dependent. The in vivo erosion profiles were used to infer physiologically relevant conditions of diluent volume and enzyme concentration. Although in vitro erosion depends both on enzyme concentration and fluid volume, a specific set of conditions resulted in an in vitro erosion profile (b) that linearly correlates with the in vivo erosion (c). A correlation between the erosion profiles in vitro and in vivo is achieved when SC implantation is plotted versus in vitro erosion of material submerged in 25 ml of PBS solution containing physiological concentration of collagenase, and for IM and IP implantations when compared with in vitro erosion using 100 ml of PBS-containing enzyme solution. The linear correlation between in vitro and in vivo erosion enables screening of materials in vitro with in vivo prediction capacity.

It is clear, then, that the current state of the art, where a defined material formulation is designed and optimized in the laboratory irrespective of the final application, is insufficient. It is crucial to carefully study the characteristics of the tissue microenvironment in the settings of the relevant pathology in which materials will be used, and to optimize them under conditions that simulate the (pre)clinical ones to allow attaining predictive behavior. However, this is not a straightforward task as tissues and cells are transient entities, capable of altering their surroundings by changing protein and enzyme concentrations, pH, redox potential, oxygenation, inflammation and tumor immunity – in response to pathology.

Altered tissue microenvironments are a hallmark of cancer (56) with an immense influence on therapeutic response (57). Pathophysiological variations are profoundly manifest in cancer (Figure 3), where the complex tumor microenvironment imparts multiple cell types, tissue chemistry and morphology, as well as mechanical stresses that are altered by local pathology with respect to normal tissues. These features can serve not only as biomarkers for cancer diagnosis and therapy but can also regulate materials' performance in light of the tumor milieu. Crafting (pre)clinically relevant *in vitro* conditions that would enable forecasting materials behavior *in vivo* is of utmost importance. This approach will help to obtain *in vitro–in vivo* correlations and hence proper material design. To develop an effective correlation, the physicochemical and dynamic properties of the materials as well as the physiological tumor milieu must be taken into consideration, as well as the effects that each of these exert on the other.

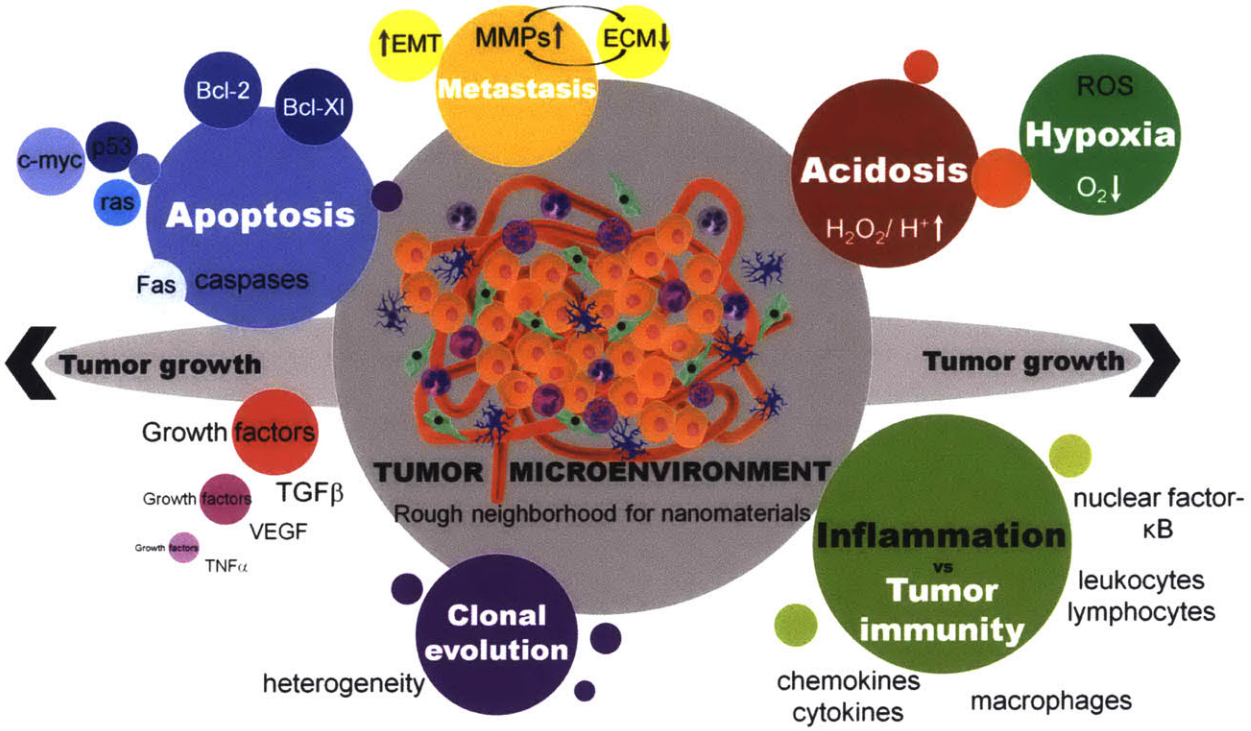

Figure 3. Established cancerous tumors consist of a wide array of cells and factors that contribute to the tumor stroma of a growing malignancy. The tumor niche is a dynamic system in which several factors such as acidosis, hypoxia, access to growth factors, apoptosis mechanisms, inflammation and immune cell interactions can vary drastically and affect both the tumor and its interaction with materials. Legend: Bcl-2 - B-Cell CLL/Lymphoma 2; c-myc - V-Myc Avian Myelocytomatosis Viral Oncogene Homolog; ECM - Extracellular matrix; EMT - Epithelial–mesenchymal transition; Fas - Cell Surface Death Receptor; MMP - Matrix Metalloproteinases; p53 - Tumor suppressor protein; ras - Rat Sarcoma Viral Oncogene Homolog; ROS - Reactive oxygen species; TGFβ - Transforming growth factor beta; TNFα - Tumor necrosis factor alpha; VEGF - Vascular Endothelial Growth Factor.

While crafting the appropriate preclinical conditions is strictly necessary to predict in vivo performance, elucidating a generic protocol for it is a challenging endeavor, as location of implantation and disease type and state will affect materials differently based on their chemical

susceptibility and mode of degradation. Thus, generating a set of rigid steps for determining material performance in the settings of disease may render suboptimal results. Instead, the set of considerations that should be assessed in vitro to identify the most determinant factors that would then mimic the in vivo conditions must be inferred on a case-by-case basis (Figure 4). For instance, the elevated concentration of reactive oxygen species in the tumor microenvironment may be the most important factor determining material degradation kinetics when the material is susceptible to oxidative stress degradation, as in the case of silicon. As silicon is being used increasingly to deliver chemotherapeutic agents (54, 58), cargo release kinetics would deviate from the expected profile if examined in ROS-free media in vitro. The effect of pH may be significant for materials that undergo hydrolytic degradation that may be further catalyzed in acidic environments. Such materials may degrade differentially depending on implantation site as the subcutaneous space contains less water than the intraperitoneal space. Natural materials, like collagen, are expected to degrade differentially in injured or inflamed environments in which MMPs are present and hence their effect should be examined in vitro. Identifying the determinant factors affecting material in vivo performance would enable attaining in vitro-in vivo correlation and will be particular to each material family and tissue/disease microenvironment.

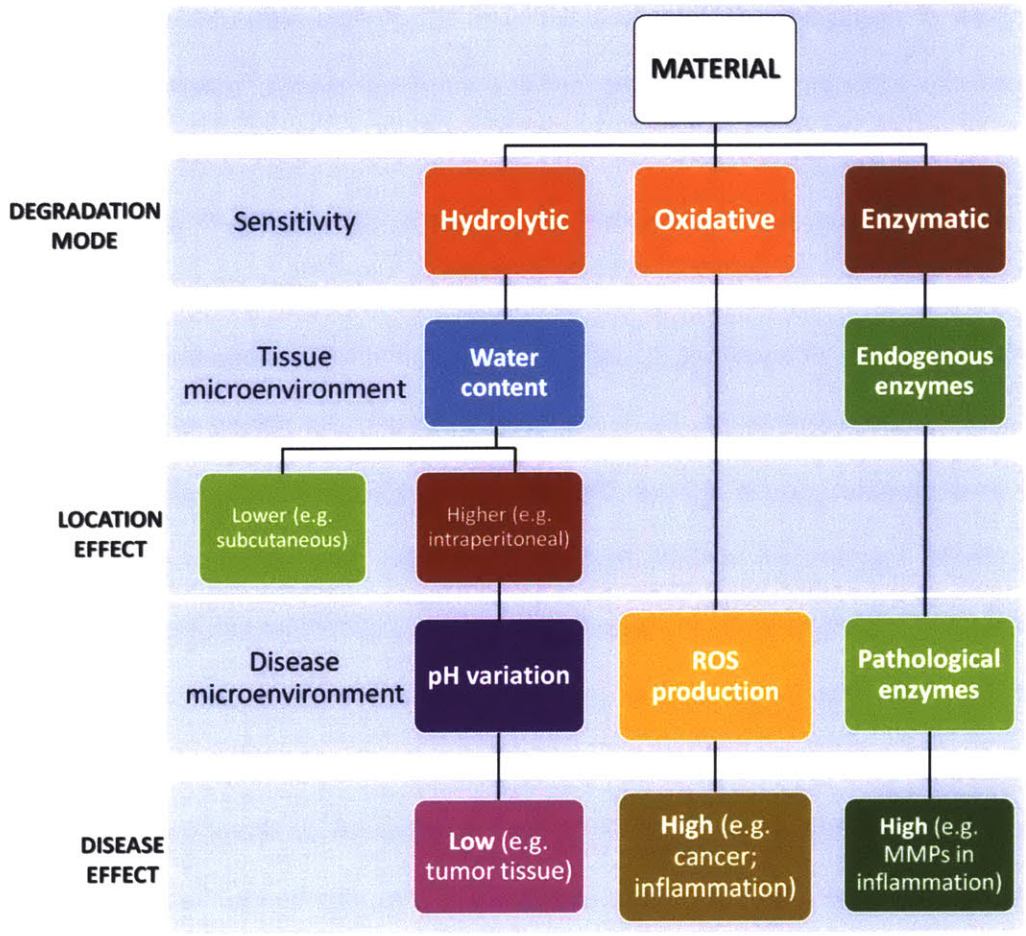

Figure 4. Case-by-case approach for the identification of determinant factors that control material performance in vivo. In vitro-in vivo correlation can be achieved only under (pre)clinically relevant conditions in vitro.

By leveraging disease cues, one can program materials to impart selective treatments while reporting on disease states. We can now exploit the characteristics of the pathological tissue microenvironment to design materials that would sense tissue state and provide selective and disease-specific treatment. The resulting materials must be based on flexible and tunable 'platforms' that can be modified to meet even the most-subtle tissue changes due to disease type and state (53).

Following these principles, we aim to understand both disease microenvironment (TNBC) and material delivery system (dendrimer) to rationally design a dendritic pro-drug to attain cancer selectivity. TNBC, while being negative for hormone receptors, typically overexpresses EGFR (59), while healthy cells surrounding the tumor express basal levels of this receptor. It has been reported that nanoparticle binding to cell membrane receptors and their subsequent internalization through RME depend on nanoparticle size and the number of receptors stimulated on the cell membrane at once (60) (Figure 5). I hypothesize that a given nanoparticle presenting multiple ligands on the surface will stimulate multiple EGF receptors on cancer cells owing to their overexpression (higher chances for ligands to interact with receptors). Basal levels of EGFR on healthy cells will not elicit enough ligand-receptor interactions to trigger RME. We aim to exploit the differential expression of this receptor in the disease microenvironment for rational design of the pro-drug to allow for selective uptake.

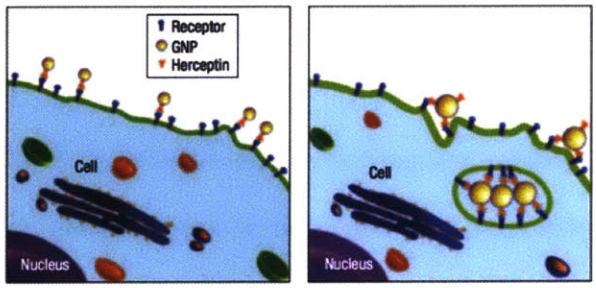

Figure 5. Nanoparticle size and ligand density

On the material side, dendrimers are spheroidal polycations that can be synthesized with a well-defined diameter and precise number of terminal functional groups (61-63). They are synthesized in a stepwise fashion, which leads to products that are monodispersed in size (as opposed to polydispersed classical polymers). Such homogeneity ensures reproducible activity and effects, reducing experimental and therapeutic variability (61, 62). Every repeated branching cycle that emerges during dendrimer synthesis is called a generation. Figure 6 shows the structure of a generation 3 poly(amido amine) (PAMAM) dendrimer. The core is depicted in red and the three consecutive

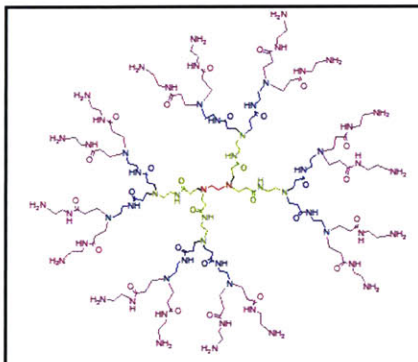
Figure 6. Generation 3 PAMAM

generations in green, blue and pink. As the generations increase linearly, the number of functional groups increases exponentially, allowing for polyvalent conjugation (61, 63-65). Their physicochemical properties resemble those of biomolecules (e.g. proteins) (66). The toxicity of PAMAM dendrimers is time-, concentration- and generation-dependent, and can be reduced by replacing the amines for neutral or anionic groups at the terminal positions(63, 67-69).

The cellular internalization mechanism of PAMAM dendrimers is subject of debate. Multiple theories have been reported, mostly involving cholesterol-, clathrin- and/or claveolae-dependent endocytosis, as well as macropinocytosis, non-specific fluid-phase endocytosis and nanoscale hole formation (70). Internalization mechanism of PAMAM dendrimers has been reported to be altered by surface modification (71). However, in all reported cases, the internalization follows multiple mechanisms at a time with a lack of specificity for the substrate. A few groups reported dendritic uptake by receptor-mediated endocytosis by conjugating ligands such as folic acid (72, 73). However, cancer-specific uptake over healthy cells has not yet been reported. Chapter 4 details the rational design of the dendritic pro-drug to attain specific uptake by cancer cells through RME.

CHAPTER 2: Development and characterization of an injectable adhesive hydrogel platform

Introduction

In this section, I will describe the development of dendrimer:dextran adhesive hydrogel and its ability to differentially react with tissues as a function of type. The dendrimer:dextran family of adhesive hydrogels constitutes a new generation of materials for drug delivery that combines the biocompatibility of hydrogels, in situ polymerization capability for injected and localized delivery, facile control over adhesion and degradation and tissue microenvironment sensitivity. Amines on the dendrimer react with aldehydes on the dextran to form a Schiff base, which is the imine product of the condensation of an amine and an aldehyde, with the release of a molecule of water (Reaction 1). This bond is labile and can be cleaved in aqueous solution by hydrolysis (74).

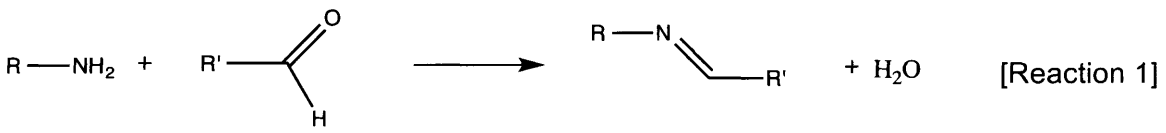

[Reaction 1]

A number of groups have taken advantage of this reaction mechanism to form adhesive hydrogels in which the bulk of the material is formed by a polymeric network with Schiff bases at the crosslinking points (39, 40, 75-80). The adhesion relies on excess aldehydes reacting with amines on the surface of tissues, provided mainly by proteins forming the extracellular matrix around the cells. Figure 7 shows the general mechanism of adhesion-cohesion in this type of materials.

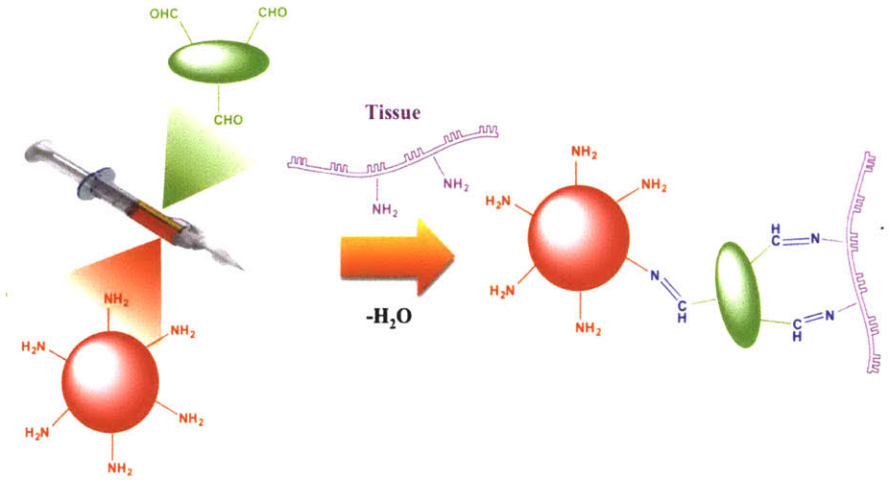

Figure 7. Schematic representation of the adhesion and cohesion mechanisms underlying amine-aldehyde adhesive hydrogels.

Aldehydes provided by the first material component react both with tissue amines to impart adhesion and with amines provided by the second material component to impart cohesion. Hence, mechanical and adhesive properties of the material can be tuned simultaneously by altering aldehyde to amine ratio. This ratio can be modified by either altering the overall solid content of the aldehyde and amine-bearing polymers, or by changing the number of amine groups available in each polymer. This is critical, as it may define not only the mechanical properties of the final adhesive, but also whether or not it will form a hydrogel or a stiff plastic-like polymer. For instance, when PAMAM dendrimer generation 5 (128 amines on the surface) at a solid content of 12.5% (w/v) was mixed with dextran-aldehyde (50% oxidation) at concentrations between 10 and 25% (w/v), the resulting product was a white, plastic-like product. However, if 75% of the amines were caped, leaving the PAMAM dendrimer generation 5 with only 32 amines on the surface, the resulting material was a hydrogel (Figure 8) (39). This proved that the reaction kinetics is critical to achieve a hydrogel structure, therefore the importance of controlling the ratios of the chemical groups.

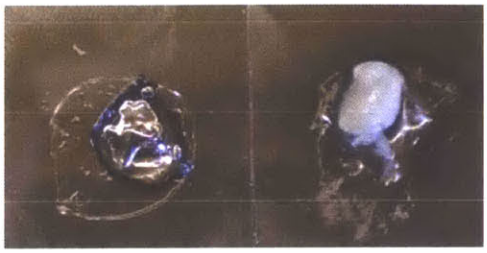

Figure 8. Images of dendrimer-dextran hydrogel (left) and non-hydrogel polymeric plastic (right).

In the development of dendrimer:dextran adhesive hydrogel family, we also examined whether differences in chemical composition between tissues would affect biomaterial function, specifically the adhesion capacity. Soft-tissue adhesive provide an ideal material class for the assessment of tissue−material interactions, which can be rigorously quantified through a series of functional assays that supplement characterizations of tissue reactivity and material fate (55, 78).

Property gradients at interfaces between tissues with different functionalities create more than physical barriers. Subtle chemical gradients enhance differential recognition and functionality even for adjacent tissues and can take on increased importance in the design of materials that interact chemically with tissue surfaces. Whereas materials and devices are designed to modulate specific functions for a given application and tissue bed, the definition of material−tissue interactions has rarely considered differences in target tissue (81). Tissues are composed of the same basic cells and components, yet subtle differences in the relative ratios and configuration of these materials allow for definitive discrimination between like and adjacent tissues. The main question that arises is, what is the role of the in vivo tissue microenvironment in determining material performance? Specifically, it is interesting to examine the effect of tissue type on material interaction. Nature employs gradients in tissue properties to impart a smooth transition between tissue regions and to facilitate differential tissue functions, chiefly by adjusting the composition

and architecture (82, 83). A vast array of techniques in material design have been employed to regulate the adhesive binding potential to tissue surfaces, including material surface patterning (84) and chemical modification (85, 86). The next step in material design would be to consider natural differences that transpire between tissue surfaces, as relevant to a specific medical application, and only then to examine how materials can be further tuned to control its performance, specifically adhesive interactions. We propose that natural variations in tissue surface chemistry affect the tissue–material interaction by way of adhesion and also affect the material properties, including cohesion and therefore the mechanical properties, morphology, and degradation kinetics. To begin to unravel the impact of natural variation between adjacent tissues, we have utilized this new family of adhesive materials based on dendrimer and dextran and have defined their interactions within the continuous regions of the small intestine: the duodenum, jejunum, and ileum. We hypothesized that differences in organ function and structure play a key role in determining the tissue composition and herein the tissue amine content. It has been shown that the serosal duodenum and jejunum contain higher collagen contents whereas the ileum presents a higher elasticity indicative of a higher elastin content. These differences in the composition of the extracellular matrix will dictate the serosal amine density, requiring the development of a specific assay to determine tissue amines (87). Variance in the surface properties of small intestinal subjacent tissues in our model system enables us to study the extent to which natural gradients in tissue properties affect tissue–biomaterial interactions and to examine whether the same material performs distinctly when applied to different tissue surfaces within the same organ.

Results and Discussion

Biocompatibility and in Vivo Pathology.

The dendrimer:dextran family of materials provides a model system for examining chemically directed adhesion. The synergy between dendrimer multifunctionality and size on the nanoscale enables the creation of smart materials with environmentally sensitive modalities (88). These materials support two competitive reactions: an external reaction between tissue amines and dextran aldehyde – promoting material–tissue adhesion – and a second, internal reaction between dendrimer amines and dextran aldehydes that adds to gel cohesion and removes free aldehydes from potential tissue toxicity (Figure 9). Multiarmed dendrimers with multiple amine groups per dendritic molecule should have a high capacity for absorbing these free aldehyde groups. When dendrimer generation and the oxidation level are optimized, the amine density determines if the material will gel, remain a liquid, or polymerize rapidly to form a plastic material. As discussed earlier, whereas generation five dendrimer with 75% oxidation and 32 surface amine groups forms a hydrogel, generation three dendrimer with 32 surface amine molecules does not gel and remains as a liquid, and generation five dendrimer with 128 amine groups polymerizes to form a white plastic that cannot retain water. Hence, we chose to work with generation five dendrimer, which has a higher molecular weight than generation three and hence less steric hindrance to allow interaction with dextran aldehyde, with only 25% of amines on the surface to support hydrogel formation kinetics.

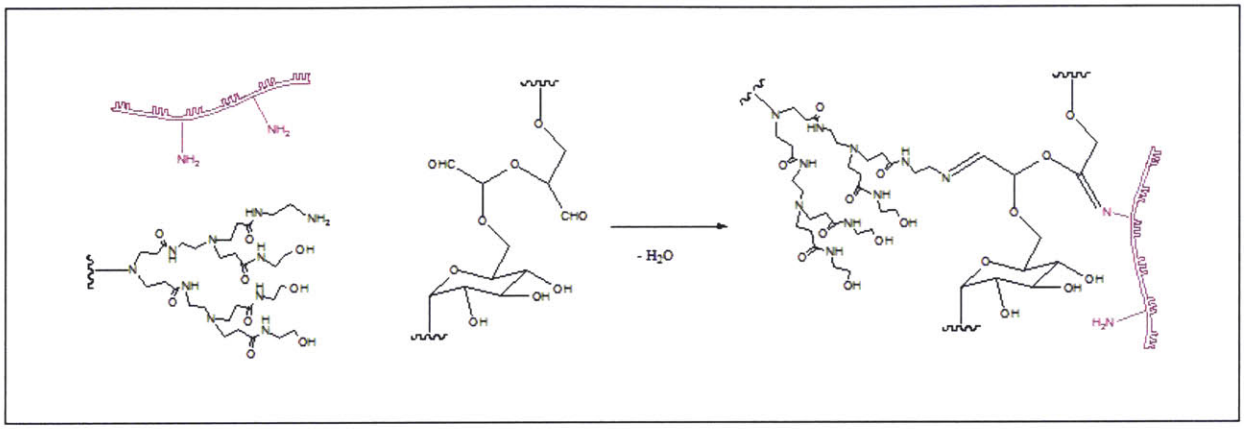

Figure 9. Reaction scheme to form dendrimer:dextran adhesive hydrogel. Dextran aldehyde reacts simultaneously with dendrimer amine generation five presenting 32 amines on the surface to create the bulk of the material (cohesion) and with amines on the surface of tissues to promote adhesion.

A subset of materials that vary in dextran aldehyde solid content was chosen from a larger set of materials to examine the material biocompatibility to assess whether excess aldehydes that remain free give rise to toxic cellular and tissue responses (40). Regardless of the dextran aldehyde solid content, cell survival was higher than 90% and supports the hypothesis that the multiple amine dendritic arms absorb excess aldehydes that might otherwise impart cytotoxicity (Figure 10).

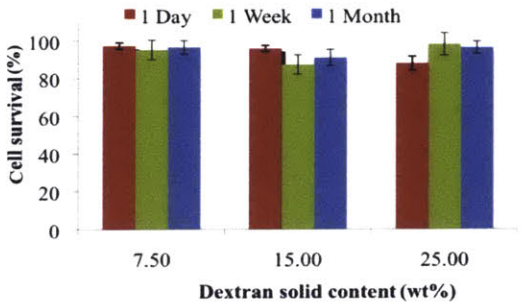

Figure 10. Material cytotoxicity examined in vitro using 3T3 fibroblasts. Cell survival in the presence of adhesive materials with increasing dextran aldehyde solid contents (7.5, 15, and 25 wt %) exceeds 90% regardless of the formulation or time elapsed (1, 7, or 30 days).

Following these experiments, materials were implanted in the dorsal subcutaneous space of a mouse that survived for 7 or 30 days (Figure 11a). Regardless of material formulation, the tissue response at day 7 was generally characterized by abundant dendrimer:dextran adhesive material in the subcutaneous region (hypodermis) surrounded by a mild to moderate zone of inflammation consisting primarily of histiocytic/macrophage infiltrates and interstitial edema with minimal scattered granulocytes (i.e., neutrophils and eosinophils) and early fibroplasia. Abundant dendrimer:dextran adhesive material was still present at day 30 but relative to that at day 7 appeared to be more vacuolated and associated with a relatively quiescent, decreased tissue response characterized by minimal cell infiltrates and the encapsulation by a thin band of fibrous connective tissue. Regardless of the time point or dose, there was no evidence of adverse pathology including hemorrhaging, necrosis, or aberrant neovascularization and no potentially adverse inflammation, supporting the potential use of such materials as adhesive materials. The inflammatory score (Figure 11b) did not exceed 2 (mild to moderate response) for any of the compositions or for the 7 or 30 day time points. Inflammatory cells such as histiocytes and neutrophils were present after 7 days as expected after any surgical manipulation, and their level diminished after 30 days, indicating a healing response.

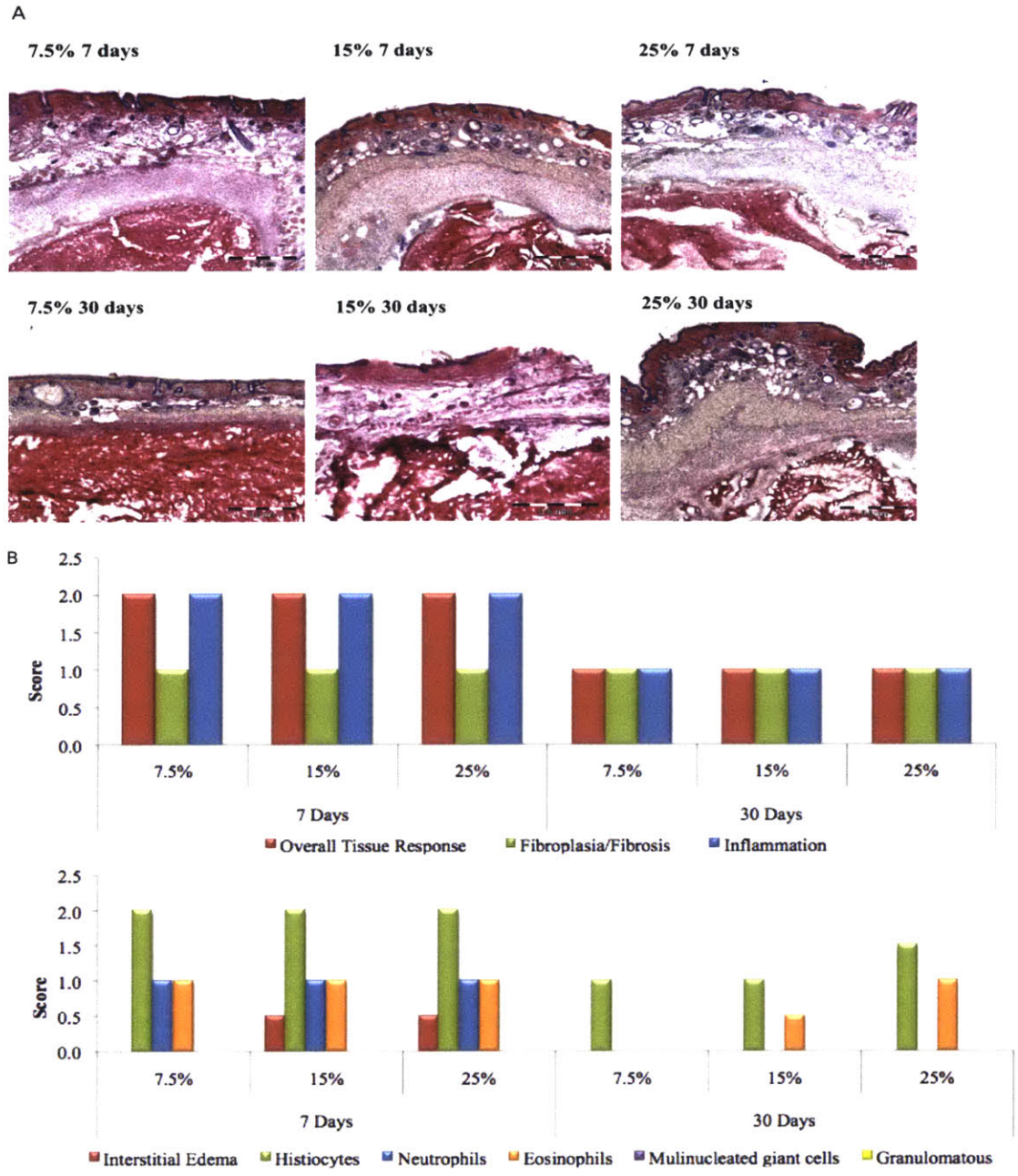

Figure 11. (A) In vivo response to adhesive materials with increasing dextran aldehyde solid contents (7.5, 15, and 25 wt %) showing minimal surrounding histiocytic/macrophage inflammation and minimal fibrous encapsulation, in agreement with the in vitro results. (B) On the basis of our scoring system, a mild response was evident at 7 days as expected after any tissue manipulation and implantation; however, this response became minimal after 30 days, regardless of the material formulation. Bar = 200 nm.

Material Tunability.

We examined the extent to which we can control the material adhesive capacity to serosal rat small intestinal tissues by varying the material formulation. A difference of 17.5 wt% in dextran aldehyde solid content imparts a 115% change in the load required to disrupt the tissue–material bond and lead to failure. As expected, the lower the amount of aldehyde, the weaker the adhesive bond (Figure 12a). Loading failure values for different material compositions were 0.2–0.4 N, which fall between the values reported for commercially available adhesive materials that are considered to be non-adhesive or extremely adherent, with loading failures of 0.15 N for fibrin glue and 0.6 N for cyanoacrylate under the same testing conditions (40). The aldehyde content is a key parameter determining not only the internal interaction with dendrimer amines but also the interaction with tissue amines. The interfacial regions between dendrimer:dextran and the excised rat jejunum were microscopically examined to add physical insight to adhesive interactions. Three distinct domains were evident with material adhesion, including the target tissue (T, red), bulk material (B, green), and an adhesive regime (I) interposed between the two (Figure 12b). The adhesive regime depicts the intermediate material structure resulting from the concurrent dextran aldehyde reactivity with dendrimer and tissue amines. The interfacial morphology of the adhesive regime varied with the material composition and reflected the strength of adhesion (78), appearing porous and discontinuous at low aldehyde content and more continuous at the higher contents. By quantifying the fluorescence intensity at the interface, we can evaluate the adhesive interactions with the tissue (Figure 12c). Indeed, there is a linear correlation ($R = 0.98$, Figure 12d) between the maximum load as measured by the strength of materials in a mechanical tester and the interfacial fluorescence signal, supporting the notion that the interfacial morphology is a good indication of macroscopic failure. Similarly, the bulk of the material is more porous at the low aldehyde solid content (7.5 wt%) and gets denser as the content increases (up to 25 wt%), giving rise to a higher cross-linking density. This is supported by the smaller pore size and faster

gelation as the dextran aldehyde solid content increases (Figures Figure 12e-f).

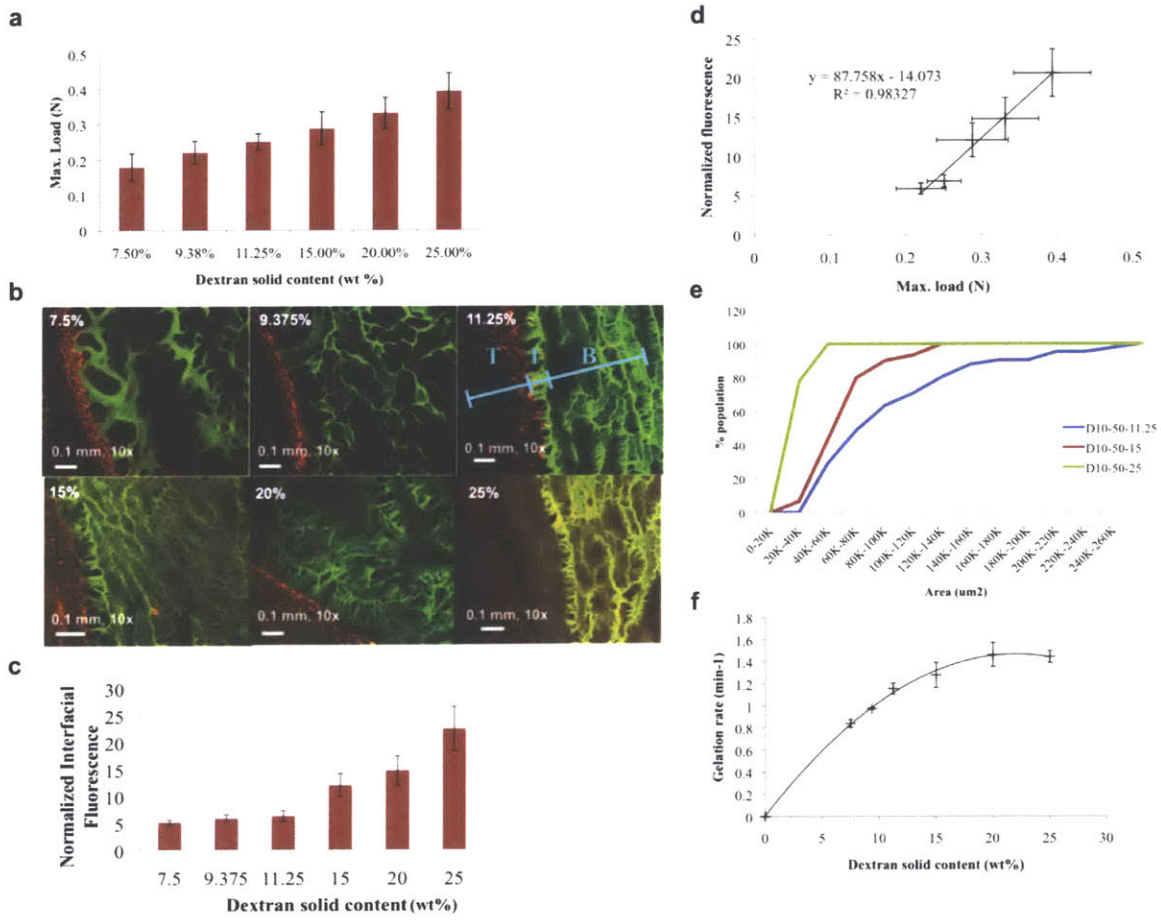

Figure 12. (a) Material adhesion strength with respect to jejunal tissue can be mediated by formulation and increases with dextran aldehyde solid content. An increase of 17.5 wt % dextran aldehyde results in a 115% increase in adhesion strength. 7.5, 11.25 and 25 wt % loads are statistically significantly different, $p < 0.5$. (b) Interaction between the adhesive material and tissue was examined by quantifying the fluorescence intensity at the interface between them (T = tissue, I = interface, and B = bulk material). Tissue was stained with propidium iodide (red) and material conjugated with fluorescein (green). When we increase the dextran aldehyde solid content, the interface becomes continuous and less porous, indicative of improved interaction with the tissues. (c) Interfacial fluorescence intensity increases with aldehyde solid content and (d) has a linear

correlation (R = 0.98) with the maximum load as measured by a mechanical tester. 7.5, 15, and 25 wt % interfacial fluorescence values are statistically significantly different, p < 0.5. Pore size distribution shows a decrease in (e) pore size and (f) gelation time with increasing dextran aldehyde solid content.

Tissue Microenvironment Alters Material Properties.

We defined the interaction of dendrimer:dextran with the three regions of serosal rat small intestine (duodenum, jejunum, and ileum) using specific material formulations of D10-50-11.25 and G5-25-12.5. The nomenclature for this material reflects a composition that contains 10 kDa dextran with 50% oxidation and 11.25 wt % solid content mixed with generation five dendrimer with 75% oxidation (25% amine surface groups) and 12.5 wt % solid content. We hypothesized that a variation in tissue properties along the gastrointestinal tract will support the diverse functionalities of these regions. Specifically, we were interested in examining whether there is a gradient in amine density along the gastrointestinal tract that would affect our material's ability to form an adhesive bond.

The surface amine chemistry of the three tissue types was quantified with fluorescent aldehyde-coated microspheres, providing a means of rapid evaluation of tissue–aldehyde reactivity (Figure 13a) and a mechanistic basis for the demonstrated variability in adhesive mechanics. We show that serosal ileum amines are at a much higher density than those of the duodenum and the jejunum ($P < 0.05$), indicating the adhesion capacity as corroborated by the quantification of interfacial fluorescence (Figure 13b) with a high correlation of $R = 0.99$ and by the tissue–material adhesion strength (Figure 13c) as measured by a mechanical tester ($R = 0.96$). These results demonstrate that the tissue amine density is a critical factor determining the tissue–material interaction and, more broadly, that one needs to consider that organ function and structure define the specific tissue microenvironment in which a material will perform its function.

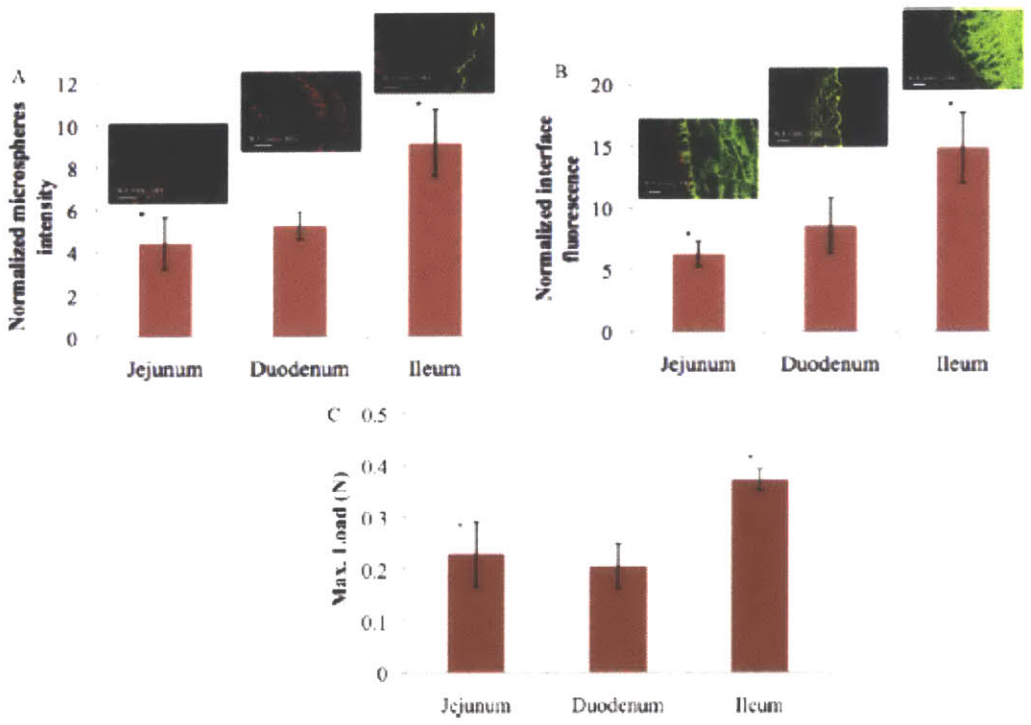

Figure 13. (A) The relative aldehyde reactivity of the jejunum and duodenum is statistically significantly different from that of the ileum, as assessed through the tissue-sample conjugation of fluorescent aldehyde-coated microspheres ($p < 0.05$ compared with the ileum). (B) The interface between dendrimer:dextran formulations (G5-25-12.5% and D10-50-11.25%, green) and the three distinct regions of the small intestine highlighted with propidium iodide (red) varies with the tissue type and is statistically significantly higher in the ileum ($p < 0.05$ compared to that of the jejunum and duodenum). (C) The higher material reactivity with the ileum is further supported by the higher maximal load seen, as measured with a mechanical tester.*

Whereas material formulation controls the adhesion and biocompatibility, it is interesting to study the effect of the tissue microenvironment and specifically the tissue amine density on adhesive material physicochemical properties, including the material morphology and degradation kinetics. The material residence time in vivo is important in determining the material capacity for providing

support as a tissue heals and gains sufficient strength. We have applied a fast degrading formulation of adhesive material to tissue biopsies from the three regions of the small intestine to examine the effect of tissue type on the material degradation kinetics. Although the same material formulation was applied to the serosal side of the three intestinal regions, material degradation was slower when applied to the ileum compared to that on the jejunum and duodenum (Figure 14a). Because the ileum provides more functional amines for the material, creating more points of interaction between them, the material stability is enhanced. Statistically significant differences are seen at early time points (1 and 2 h) whereas at late time points as the material loses much of its integrity the differences are less significant although on average they are still evident. This trend is supported by images of fluorescently labeled material and stained tissues after 0, 1, and 2 h (Figure 14b). With time, less material is evident in the duodenum and jejunum and more material remains attached to the ileum. The dendrimer:dextran tunable family of materials shows great promise as surgical sealants with adequate adhesion, biocompatibility, and graded interaction with different tissues presenting a distinct density of surface chemical groups.

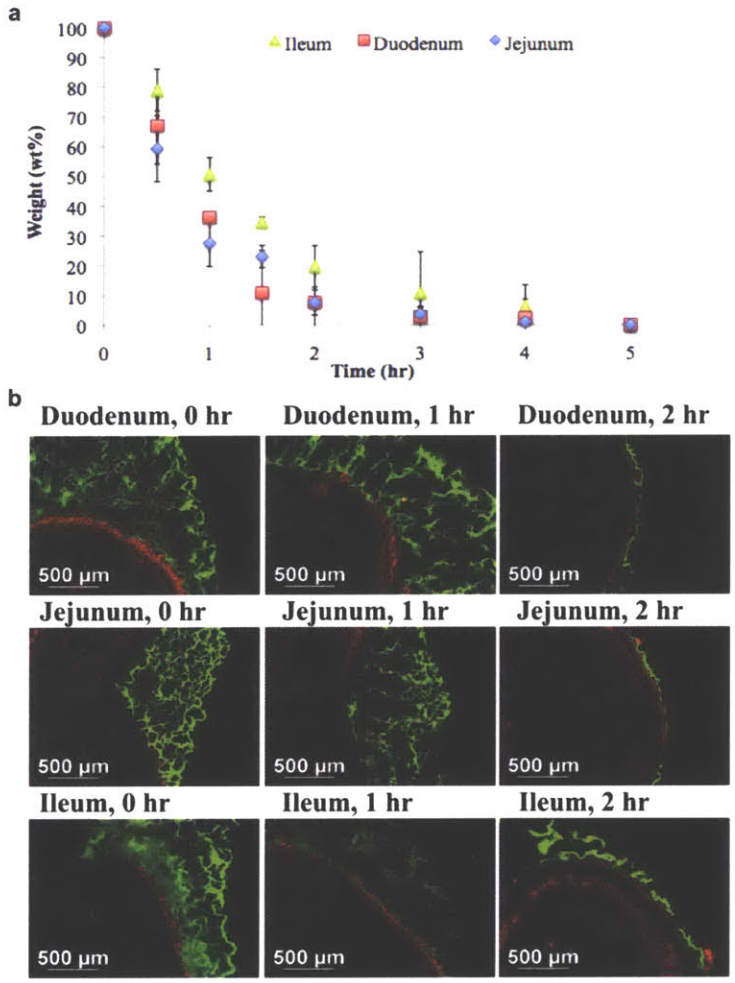

Figure 14. Tissue type affects the material residence time via the variation in the tissue–material interaction, as demonstrated by (a) the weight loss and (b) the correspondent fluorescence microscopy images (tissue – red and material – green) of a quickly degrading material (D40-10-5% + G5-25-20%) when applied to the three regions of the small intestine.

Tissue-Specific Adhesive Formulations.

Though the tissue type imposes constrains on the material, flexibility in material design enables control over material properties by providing a specific material formulation for each tissue. We show that changes in the material formulation can regulate the adhesion strength for each specific region of the rat intestine (Figure 15). By providing aldehydes for specific tissue amines, we

modulated adhesion to an extent that depends on each tissue. Because the ileum has more amines, it is more responsive to changes in material formulation in the form of aldehydes. While increasing dextran aldehyde solid content from 11.25 to 15 wt% increased the maximal load in 15% for the three intestinal parts, further increase in dextran aldehyde to 25 wt% raised the load at failure to 55%. Providing more aldehydes similarly increases the load at failure for the three regions of the intestine. However, the higher number of tissue amines in the ileum absorb more aldehydes thus increasing the absolute value of the load to failure as the dextran-aldehyde content increases.

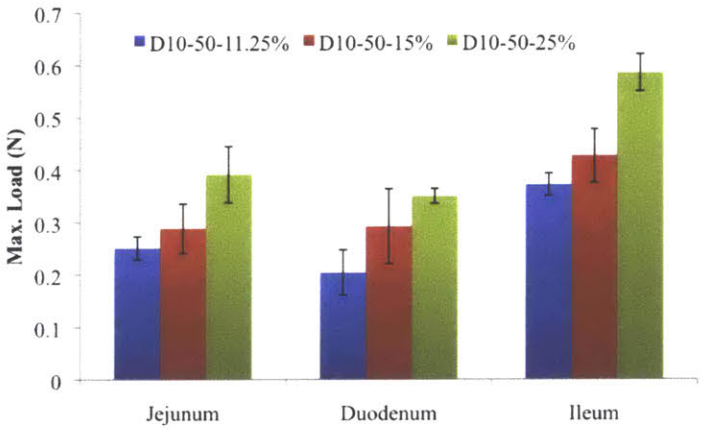

Figure 15. Tissues are responsive to changes in the dextran aldehyde solid content. By changing the material formulation, we can regulate the adhesion strength for each specific region of the intestine. For each composition, ileum load values are statistically significantly higher than those of the jejunum and duodenum, $p < 0.5$.

These results demonstrate that the specific tissue properties of the target organ, particularly its chemistry, must be considered when developing new materials, specifically adhesive materials, to facilitate the optimal tissue response and clinical outcome.

Conclusions

The optimization of tissue adhesive materials can minimize complications associated with internal leakage as seen, for example, in the gut, which is a frequent surgical complication that results in high morbidity and mortality. The variability in tissue structure and chemistry supports the diverse set of functions that tissues provide and should be seen as imparting differing microenvironmental conditions and reactivity to materials. Tissues and materials, specifically biodegradable materials, continuously influence each other. Although materials are subject to rigorous design criteria and thorough characterization, the properties of the target tissue, including tissue chemistry and morphology, must be considered when a material is to be used in a specific application and in a specific site. Herein, we utilized a model organ (the small intestine) and an adhesive hydrogel (dendrimer:dextran) to demonstrate a wider concept: the formulation of biomaterials such as adhesive materials requires an understanding and tailoring based on the specific target tissue properties. The generalized use of an adhesive for a wide range of tissues will result in suboptimal clinical outcomes and in some cases device failure. Because material performance is a contextual state rather than just a constitutive property, it can be determined only within specific environments. Understanding biomaterials and tailoring them to elicit the desired in vivo effects is a crucial step in biomaterials research. A rational process in material design under controlled environments considering target tissue properties will allow the development of tailored biologically relevant materials that are site- and application-specific and therefore clinically superior.

CHAPTER 3: Dendrimer:Dextran Hydrogel's Performance And Biocompatibility Are Contextual

Introduction

A "one material fits all" mindset ignores profound differences in target tissues that affect their responses and reactivity. Yet little attention has been paid to the role of diseased tissue on material performance, biocompatibility, and healing capacity. We assessed material-tissue interactions with our prototypical adhesive material based on dendrimer:dextran and colon as a model tissue platform. Adhesive materials have high sensitivity to changes in their environment and can be exploited to probe and quantify the influence of even subtle modifications in tissue architecture and biology. We studied inflammatory colitis and colon cancer and found not only a difference in adhesion related to surface chemical interactions, but also the existence of a complex interplay that determined the overall dendrimer:dextran biomaterial compatibility. Compatibility was contextual, not simply a constitutive property of the material, and was related to the extent and nature of immune cells in the diseased environment present prior to material implantation. We then showed how to use information about local alterations of the tissue microenvironment to assess disease severity. This in turn guided us to an optimal dendrimer:dextran formulation choice using a predictive model based on clinically relevant conditions.

We used the gastrointestinal tract as a model system to study the impact of disease on the tissue microenvironment and two disease models—inflammation and neoplasia—which we surmised would span a range of cellular responses and a spectrum of reactions to a material. Adhesive materials are ideal candidates with which to study the effects of gut disease on performance given their intimate interaction with tissue in this defined locale and their clinical relevance in mediating

complications associated with leakage after surgical gut repair (89). We recently showed that adhesive dendrimer:dextran-based materials facilitate the probing of local changes in tissue surface chemistry by virtue of their distinct interactions with different target tissues (78, 89). Here, we exploit this feature to examine, in our model systems, the effects of disease-driven alterations in local tissue-state on the tissue microenvironment and the clinical implications of such alterations. We show that neplasia and inflammation of the colon are two distinct processes that present substantially different surfaces—driven by their biochemistry and cell biology—to the external environment. Interaction of the dendrimer:dextran material with tissue surfaces and tissue responses to this adhesive material were altered in a disease type– and pathological state–dependent manner. The interrelationship between material science and tissue biology should be considered as we seek to facilitate predictive and controlled material performance in specific clinical scenarios. Concepts learned from these studies might illuminate general guidelines by which to assess material-tissue interactions and their disease-driven alterations.

Results and Discussion

Characterization of tissue surface chemistry and material performance in colon cancer and colitis.

We used two different animal models for studying the impact of local pathology on dendrimer:dextran performance across species and recapitulated the chemical, structural, and biological cues characteristic of a particular disease in a specific location. We used a commercially available rat orthotopic model for colon cancer and developed a colitis model in rabbits that provided sufficient tissue biopsies to conduct mechanical testing, characterize tissue chemistry, and build a predictive model that informs material choice for each disease severity.

Dextran aldehyde reacts internally with dendrimer amines to form a hydrogel and with tissue amines to provide adhesion. To understand the extent to which tissue surface chemistry was

altered by cancer or colitis in our model systems, we quantified the interaction of aldehyde-coated microspheres with healthy and diseased tissues as a measure of tissue-amine binding sites. We hypothesized that microsphere adhesion in colon cancer would exhibit alterations in concert with changes in tissue surface amine density. Indeed, a significant increase in amine density was detected with fluorescent aldehyde-coated microspheres in cancerous colon tissue (Figure 16A, i-ii), which displayed a greater number of chemical groups that were available for material interaction. A concomitant increase in material adhesion (Figure 16A, iii-iv) was detected by fluorescence intensity at the interfacial region, defined as the area of the biomaterial interacting with the tissue that has a distinct morphology from the rest of the bulk of the material (Figure 17 A-B). Smaller and fewer pores of reduced area (U=interfacial pores area) were present within a narrower interfacial region (W= interfacial width) (W= 104.7 ± 20.8 μm and U = $5.85x10^2$ ± $7.77x10^1$ μm^2 for cancerous rat tissue and W= 130.3 ± 27.9 μm and U = $5.44x10^3$ ± $1.75x10^3$ μm^2 for healthy rat tissue; Figure 17 c-d; $P<0.05$ by two-tailed *t*-test for independent samples), which indicated that interfacial adhesion and integration of the material were enhanced. Macroscopic-force measurement of adhesion failure (as determined with a mechanical tester, see Materials and Methods) rose 43% (from 0.566 ± 0.08 N to 0.808 ± 0.04 N) for colon cancer tissue compared to the healthy colon tissue (Figure 16C, $P<0.05$ by two-tailed *t*-test for independent samples). This increase in the maximum load correlated with observed microscopic changes, as indicated by higher interfacial fluorescence and amine density.

In contrast, amine density was lower in inflammatory colitis compared to the healthy state (Figure 16B, i-ii). Material-tissue adhesion was reduced in colitis tissue (Figure 16B, iii-iv and Figure 17e) as indicated by a wider interfacial region as well as a higher pore area (W=216.3 ± 37.5 μm and U=$1.39x10^4$ ± $2.84x10^3$ μm^2) compared with that of healthy colon tissue (W=108.3 ± 38.6 μm and U=$3.40x10^3$ ± $1.13x10^3$ μm^2; Figure 17f-g; $P<0.05$ by two-tailed *t*-test for independent samples).

The reduction in tissue binding sites indicated by microsphere conjugation translated into inferior material adhesion strength as corroborated by a 58% reduction in the mechanical load required to break the bond between the colitic tissue and our material relative to the healthy state (from 0.812 ± 0.16 N to 0.34 ± 0.13 N, respectively) (Figure 16D, $P<0.05$ by two-tailed *t*-test for independent samples).

We then examined whether dendrimer:dextran formulation protocols can compensate for the reduced availability of tissue binding sites in colitis. Material composition spanned a wide range of adhesion strengths (Figure 16E). As dextran aldehyde solid content was increased from 7.5 to 25 wt%, maximal load at failure increased 235% (from 0.25±0.03 N to 0.83 ±0.22 N, $P<0.05$ by two-tailed *t*-test for independent samples) (40, 89). The excess aldehydes provided by raises in the dextran aldehyde solid content increased the probability for material interaction with tissue amines. Indeed, by increasing dextran aldehyde solid content from 10 wt% in healthy tissue to 25 wt% in the case of colitis, we were able to compensate for the reduction in tissue amine density in the disease state and achieve the same level of adhesion strength as in the healthy state (Figure 16F).

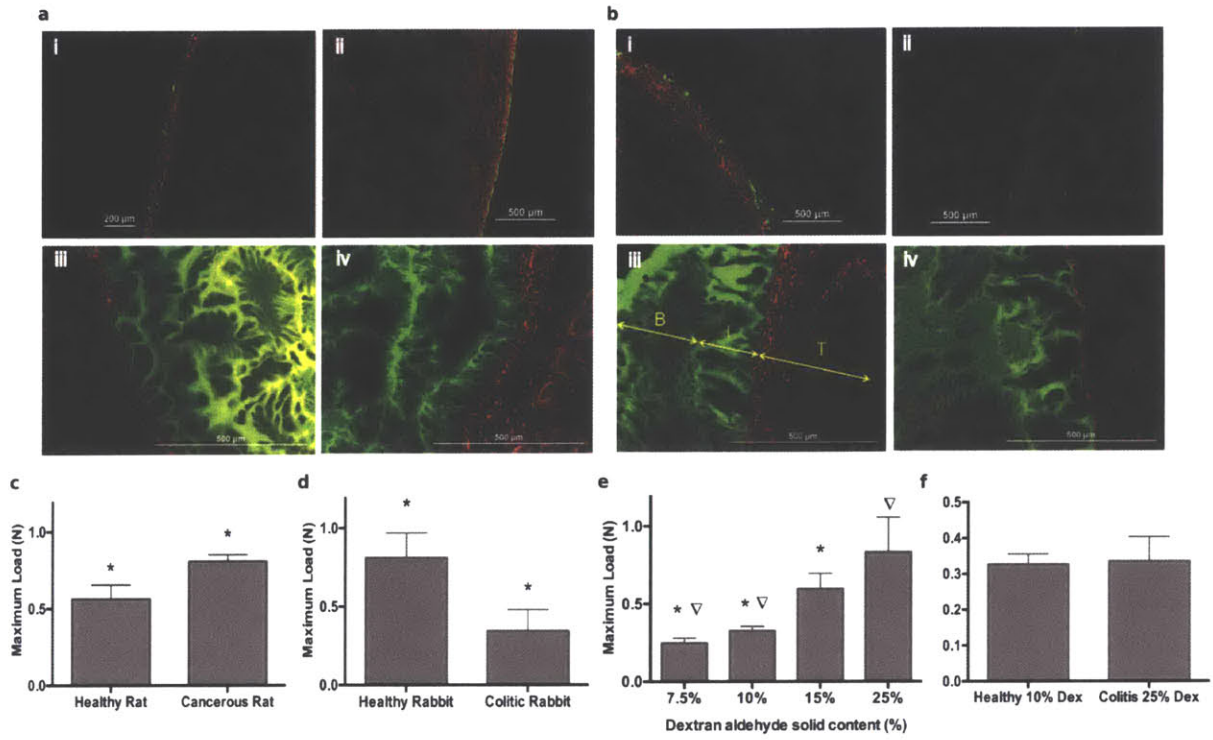

Figure 16. Assessment of tissue:material interactions and mechanical properties as a function of disease type. (a) Amine density on colon serosal layer was assessed by aldehyde-coated fluorescent microspheres (green) in rat healthy (i) and cancerous (ii) tissues (red, stained with propidium iodide); and dendrimer:dextran adhesive (green, tagged with fluorescein) morphology when applied to rat healthy (iii) and neoplastic (iv) tissues (red, stained with propidium iodide). (b) Aldehyde-coated fluorescent microspheres (green) and dendrimer:dextran morphology (green, tagged with fluorescein) applied to rabbit healthy (I and iii) and inflamed (ii and iv) tissues (red, stained with propidium iodide). Maximum load at failure measured for (c) healthy and cancerous tissues and (d) healthy and inflamed tissues. (e) Maximum load at failure measured for different material formulations (dextran aldehyde solid contents from 7.5 to 25% with fixed dendrimer amine solid content of 20%) on healthy rabbit colon ($P < 0.05$). Dextran aldehyde solid content can be tuned to match the surface amine density of the target tissue. (f) By increasing dextran aldehyde solid content from 10% to 25%, statistically equal levels of adhesion can be achieved in healthy and inflamed tissues, respectively. For all mechanical testing data, N=5 for each

experimental group. In each graph, data marked with the same symbol represents statistical significance with P<0.05.

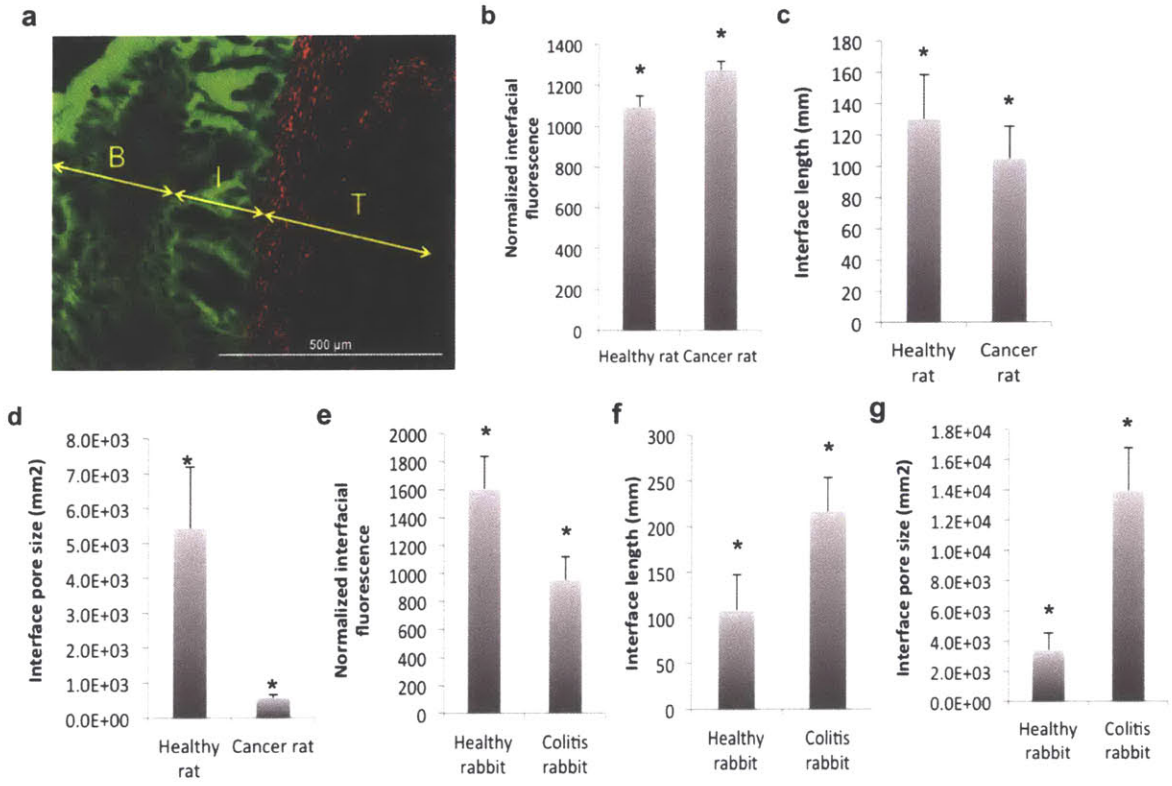

Figure 17. Dendrimer:dextran Interfacial Morphology Characterization in Inflammation and Neoplasia. (a) Morphology of the interfacial region between fluorescein tagged adhesive material (green) (B – bulk, and I – interface) and excised rabbit colon tissue (T), stained with propidium iodide (red). (b) Interfacial fluorescence when material was applied to healthy and cancerous rat colon was quantified as a surrogate for material adhesion/interaction with the tissue. Interfacial (c) length and (d) pore size was measured in healthy and cancerous states in rat colon ($p < 0.05$). Interfacial (e) fluorescence, (f) length and (g) pore size were also measured in healthy and colitic rabbit colon ($p < 0.05$).

We demonstrated in Chapter 2 that variations in tissue surface chemistry between different tissue surfaces dictate their interaction with our adhesive material in healthy states (78, 89). We showed herein that tissue surface chemistry was modified to an even greater extent by local pathology relative to variations from one tissue to another in the healthy state. Pathological states exerted profound effects on tissue:biomaterial interactions and material performance for dendrimer dextran adhesive hydrogel. Tissue surface chemistry (amine content) and the biological microenvironment were significantly altered in the face of inflammation and neoplasia.

Determination of diseased-tissue surface chemistry by collagen quantification.

To understand the underlying mechanism that mediated tissue surface chemistry modifications in the context of cancer and colitis, we characterized the primary tissue proteins in healthy and diseased tissues. Collagen-I accounts for ~70% of the total collagen in gastrointestinal tissues (90). Using cryosectioned tissue, we measured a significant increase in collagen content in vitro in the presence of neoplasia (Figure 18a). The same trend was observed when we quantified collagen and bound microspheres on healthy and cancerous tissue surfaces (*en face*) in the in vivo imaging system. These findings suggest that a higher number of amine groups reside on the surface of cancerous versus healthy colon tissue (Figure 18b). Colorectal cancer is driven by unbridled cell proliferation and an abundant extracellular matrix response with marked elevation in internal collagen levels, which are reflected on the surface and subsequently accompanied by increased amine binding sites. This indeed resulted in a 43% increase in adhesion strength in tumoral compared to healthy tissue.

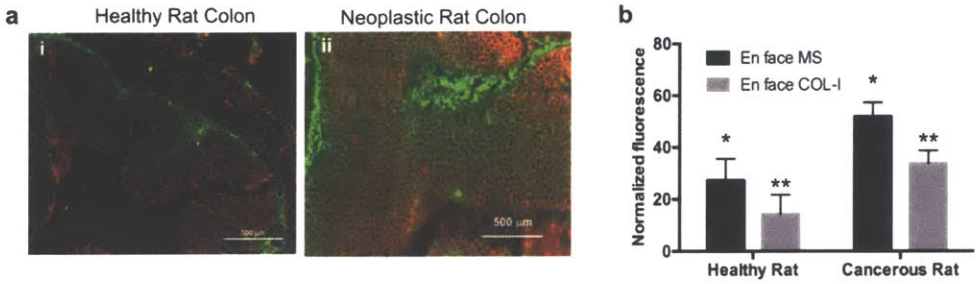

Figure 18. (a) Collagen I Immunostaining in Healthy and Neoplastic Tissues. Basement membrane collagen I (COL-I) immunostaining (green, FITC-conjugated secondary antibody) in healthy and neoplastic rat colon (red, stained with propidium iodide). (b) Amine density and surface collagen content were quantified en face using aldehyde coated fluorescent microspheres and anti-collagen I antibody, respectively, in (a) healthy and cancerous rat tissues (n=3 for each experimental group).

In contrast, inflammation is known to result in collagen degradation and tissue surface remodeling as a consequence of the release, by neutrophils, of factors that activate matrix metalloproteinases such as MMP-8 (also known as collagenase-2 or neutrophil collagenase). The question that arises is whether there would be a similar alteration in tissue surface chemistry in a disease that originates remotely from the tissue surface, as in the case of inflammatory colitis. The inflammatory reaction of colitis is most intense at the luminal side, presenting irregular or obliterated crypts, inflammatory cell infiltrates in the lamina propria, and abscess formation at the bottom of the crypts (91). Serosal surface–interacting materials such as adhesives are thus removed from the major source of tissue alteration, yet we observed deep tissue injury manifested as reduced amine density on the serosa compared to healthy tissue. Inflammation elicits neutrophil recruitment across the colon, starting from the mucosa and covering the serosa. As the infiltrating neutrophils release metalloproteinases, they break down collagen to allow for tissue remodeling and healing. We hypothesized that disease-driven changes in collagen levels on the

surface of the gut lumen, where the disease originates, would disseminate to the external surface of the gut, serosa (peritoneum-facing), where the material is applied. Alteration of tissue serosal surface chemistry would then affect material performance. To examine this hypothesis, we induced colitis in rabbits by instilling 2,4-dinitrobenzenesulfonic acid (DNBS) intra-colonically and tested whether collagen content and hence, amine concentration varied on the serosal side of the gut. We observed a reduction in collagen content throughout the three layers of the intestinal wall of colitic tissue (Figure 19A, i and iii), and this effect disseminated to the serosal layer, as evident by the reduction in *en face* collagen content (Figure 19A, iv-vi) and microsphere conjugation (Figure 19B). There was a strong linear correlation (R^2=0.99, Figure 19C) between serosal *en face* collagen I content and serosal tissue amines (as measured by microspheres conjugation), and this relation was maintained across species (rats and rabbits; Figure 19C). Indeed, adhesion strength in colitic tissue with ~80% less collagen I (Figure 19B) was 58% lower than that achieved for healthy tissue (Figure 16D). The significant alteration of tissue surface chemistry in pathological states reiterates the importance of understanding the disease impact on the tissue microenvironment in the selection of dendrimer:dextran material formulation and also might be helpful in the design of other surface-interacting biomaterials.

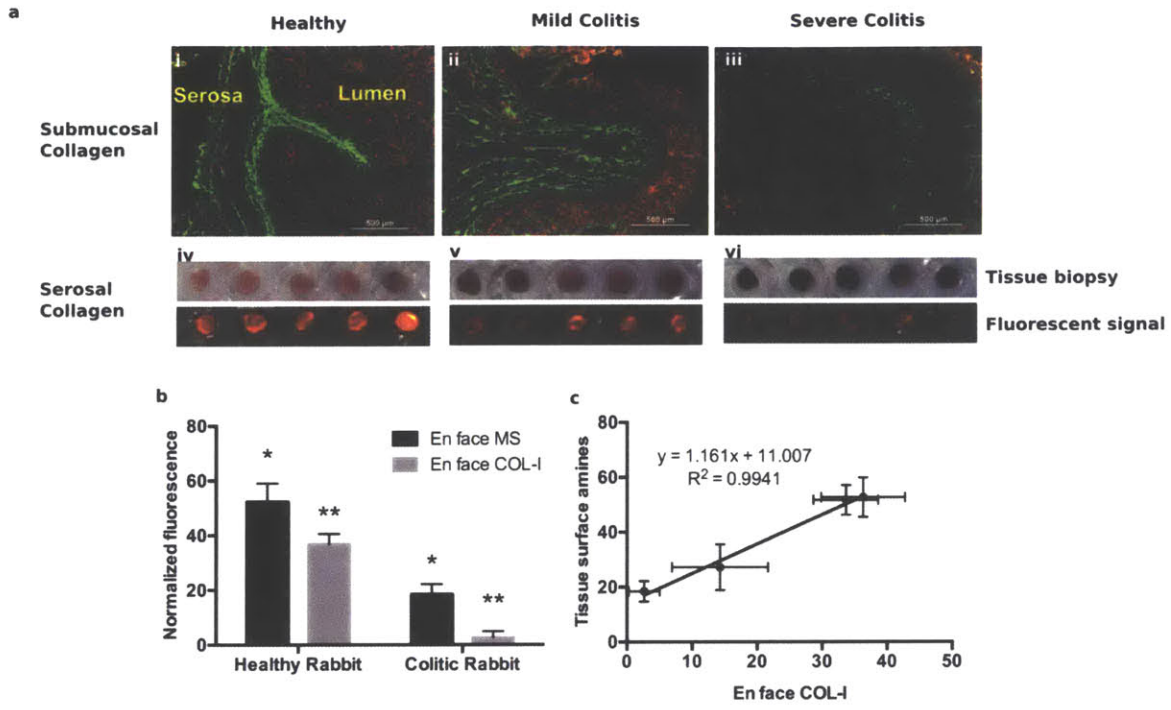

Figure 19. (a) Immunofluorescence staining against collagen, both for basement membrane collagen (cryosection staining, i to iii) and serosal collagen (en face staining, iv-vi), was performed in rabbits using healthy, mild and severe colitic tissues. (b) Amine density and surface collagen content were quantified en face using aldehyde coated fluorescent microspheres and anti-collagen I antibody healthy and colitic rabbit tissues (n=10 for each experimental group). (C) High correlation is achieved between collagen and amine density en face (R2=0.99, P< 0.05). In each graph, data marked with the same symbol represents statistical significance with P<0.05.

Deciphering the impact of disease severity on tissue microenvironment.

Colitis presents clinically as a range of severities. We investigated whether differential luminal degrees of inflammation would disseminate to the serosal side in a disease-severity dependent manner. We instilled various concentrations of DNBS into rabbit colons to achieve a range of disease severities and then validated our model through quantification of tumor necrosis factor alpha (TNF-α) and neutrophil recruitment in the gut (Figure 20a, i-vi). TNF-α is known to be

upregulated in inflammatory bowel disease in humans (92) because it is released in the context of inflammation by immune-surveillance macrophages present in the mucosal layer of the colon (93). TNF-α upregulation then leads to neutrophil recruitment to the gut mucosa, tissue infiltration and subsequent release of MMP-8, which degrades collagen in the basement membrane (94). Indeed, TNF-α release increased over a 7.4-fold range (from 30.9 ± 8.57 to 229.2 ±27.67 in relative fluorescence) with the severity of induced colitis, while neutrophils recruitment was increased in a correlative manner (5.5-fold; from 10.7 ± 13.51 to 60.4 ± 5.93 in relative fluorescence) (Figure 20b). As a result, we observed a correlative 1.7-fold decrease in basement-membrane collagen (from 336.6 ± 8.05 to 218.7 ± 15.65 in relative fluorescence).

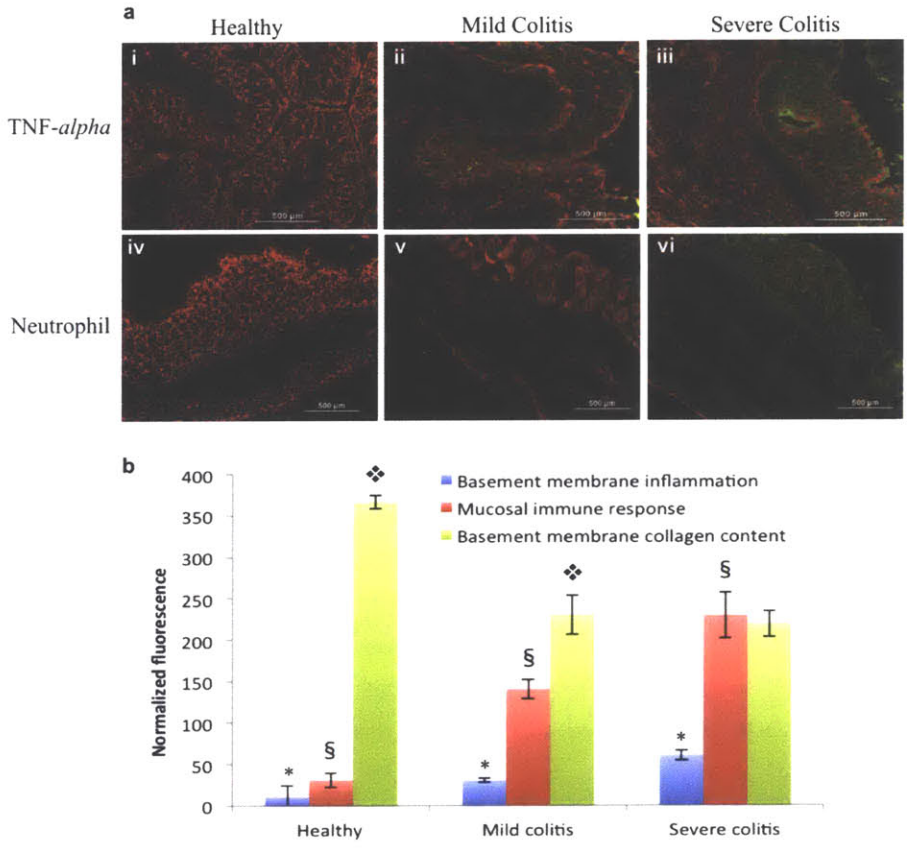

Figure 20. Study of Alterations in Tissue Biological and Chemical Cues as a Function of Disease Severity. (a) Immunofluorescence staining against mucosal TNF-a (i-iii) and basement membrane neutrophils (iv-vi) were performed in rabbit healthy, mild and severe colitis tissues. (b) Normalized

fluorescence from mucosal TNF- a, neutrophils and basement membrane collagen in the tissue sections was quantified ($p < 0.05$).

We also observed a linear correlation between *en face* collagen content in the serosa (Figure 19a, iv-vi) and the extent of inflammation, as measured by the recruitment of neutrophils to the gut, thus corroborating the transmural nature of this disease in our rabbit model (Figure 21a, R^2=0.97). This decrease in serosal collagen level was further supported by a decrease in surface amine density, which correlated linearly with serosal collagen content (Figure 21b, R^2=0.94). These findings suggest that one can use the rapid measure of surface amine density to guide one's choice of adhesive properties in a dendrimer:dextran material in a way that is clinically relevant and yields information on disease severity. Such properties might facilitate a more personalized selection of materials for colitis treatment than is currently possible.

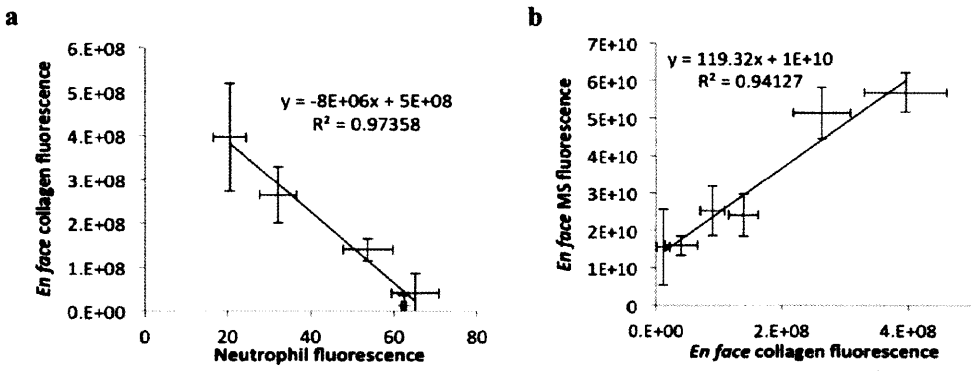

Figure 21.En face Collagen I Correlations with Neutrophil Recruitment and Microspheres Conjugation. En face collagen content (b), measured by immunofluorescence staining, correlates with neutrophil recruitment to the colorectal wall, as measured by fluorescence immunostaining on tissue sections. Collagen content en face (c) also correlates linearly with the serosal amine content, as measured by aldehyde-coated fluorescent microspheres en face.

Building a predictive model to guide material choice.

Dendrimer:dextran performance is not only affected by different pathological processes such as carcinogenesis and inflammation, but it is also altered by different states of a particular disease. Colitic tissues with different degrees of inflammation were tested for amine density and adhesion strength using three different material formulations of varying aldehyde content (10%, 15%, and 20%). The data set described adhesion strengths for three different dendrimer:dextran material formulations as a function of a range of colitis severities as measured by amine density. For a particular formulation, adhesion strength decreases with disease severity in a linear fashion. As we increase dextran aldehyde solid content, the slope of this curve increases, indicating higher adhesion strength (Figure 22a). A linear regression model was fit to each material formulation (Figure 22a) and the slopes of the curves were plotted as a function of aldehyde solid content, yielding a linear relationship (Figure 22b). Interestingly, there is a linear correlation between the slope of these curves and dextran solid content (R^2=0.99, Figure 22b). Hence, we can predict adhesion strength of a new formulation for any disease state using these relationships. The slope of a new material formulation with a defined dextran aldehyde solid content, 25%, was extrapolated from this fit (Figure 22b, red triangle). The model was validated by comparing the measured adhesion strengths using a mechanical tester with the calculated ones following *ex vivo* application of the 25% solid content material formulation to tissues with three different degrees of colitis severities. Indeed, there was an excellent agreement between the calculated and predicted adhesion strengths of 25% dextran aldehyde formulation applied to tissue surfaces that are healthy, or with mild and severe colitis (R^2=0.99, with errors smaller than 6%, Figure 22c). As expected, there was an inverse linear correlation between disease severity and adhesion strength, as a result of amine density loss (Figure 22a). We demonstrated that providing more aldehyde groups to react with tissue with low amine density can compensate for the reduction in adhesion strength resulting from collagen loss. The obtained linear relationships allowed us to construct a mathematical fit for the data, which in turn enabled us to predict the adhesion strength

of a completely new dendrimer:dextran formulation when applied to either healthy, mild, or sever colitic states. If this approach can be implemented in a clinical setting where a patient's colorectal biopsy can be rapidly analyzed for amine density, it would allow the surgeon to choose the optimal adhesive formulation on the basis of an individual patient's needs. This practice would help prevent material failure and improve patient outcome. We envision performing rapid assessment of amine density in the operating room on patients' biopsies to guide surgeons on the optimal material formulation to be used, in a patient-specific manner, such that adequate adhesion will be achieved.

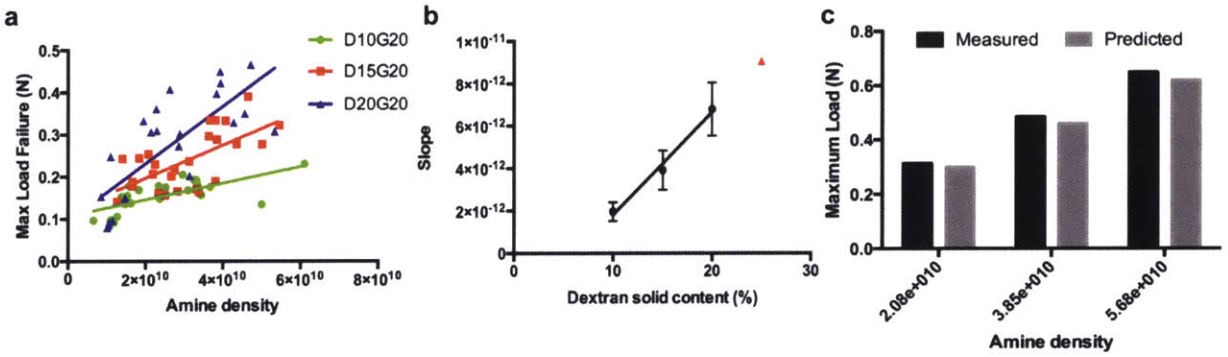

Figure 22. (a) Maximum load at failure as a function of amine density and hence, inflammation severity, for a range of material formulations (D10, 15, 20 represent dextran aldehyde with 10, 15, or 20% solid content, and G20 is PAMAM dendrimer 20% solid content; N=20 of varying degrees of inflammation for each adhesive formulation). (b) The slopes of the curve fits for maximum load at failure as a function of inflammation severity linearly correlate with dextran aldehyde solid content (10, 15, and 20%). This correlation was used to predict the slope for a new dextran solid content of 25% (D25, red triangle in the graph). (c) Experimental (measured) and predicted (calculated using model) adhesion strengths of a new formulation (D25 and G20) applied to three tissue samples spanning a range of inflammatory severities (N=1 for each inflammation severity).

Evaluation of material biocompatibility and healing capacity in vivo.

We examined inflammation in the implant area as well as biological response to a dendrimer:dextran material (serosal heterophils) and healing capacity (serosal fibrosis) compared to use of sutures in vivo for healthy compared to colitic or cancerous tissues. Healthy rat colonic tissue appeared normal in structure (Figure 23a, i-iii), and the colorectal cancer rat model verified the existence of a mass of abnormal tissue with differentiated cells forming the tumor (Figure 23a, iv-vi). Similarly, healthy rabbit colonic tissue appeared normal with intact mucosal and serosal layers (Figure 23b, i-iii), while colitic tissue presented as diffusely necrotic mucosa with an intense heterophilic inflammatory response (Figure 23b, iv-vi).

The levels of inflammation were not statistically distinguishable when dendrimer:dextran material was applied to the serosal layer of lacerated healthy or cancerous tissue in the presence or absence of the adhesive (Figure 23c-d). The difference in heterophil (defined as granular leukocytes) recruitment to the serosal layer was not statistically significant when sutures alone were used compared to sutures plus adhesive, both in healthy and cancerous states (Figure 23c-d). Serosal fibrosis was similar with and without adhesive application in healthy tissue (Figure 23c). When sutures alone were applied, tissue fibrosis was reduced in the cancerous state compared to the healthy state. Application of adhesive material to cancerous tissue improved healing to levels comparable to those of healthy tissue, as measured by serosal fibrosis (Figure 23d). Colitic tissue presents with higher total inflammation whether sutures alone or sutures plus material were applied, owing to the nature of the disease (Figure 23f). The immune response to dendrimer:dextran was contextual; the number of serosal heterophils in lacerated healthy tissue was not altered upon material application to the serosal layer; in contrast, the difference in serosal heterophil numbers upon material application was statistically significant in the colitic state compared to sutures alone (Figure 23e-f). Similar to what was observed in the cancerous model, healing capacity (as measured by serosal fibrosis) after material application to the serosal layer

in colitic tissue was improved compared to that of suture application alone, while healthy tissue presented good repair capacity irrespective of whether the adhesive material was used or not (Figure 23e-f). Dendrimer:dextran biocompatibility was also disease-dependent as measured by the recruitment of serosal heterophils to the interface with the adhesive material (Figure 23c-f). Differences in disease-specific basal immunity—as evident from total inflammatory scores at tissue sites prior to injury and treatment—may explain these variable responses. Although basal immunity varies dramatically in colitic versus healthy tissue, the basal inflammatory score in the cancerous state was similar to that of a healthy state (Figure 23c-d). These trends correlated with the levels of heterophils recruitment upon dendrimer:dextran application compared to suture application alone (Figure 23d and f), being higher in colitic versus cancerous tissue. Assessing both the basal immune state as well as disease-specific immune responses was crucial to deciphering material compatibility. Healing capacity followed the same trend in both models—although our material did not affect healing in healthy tissues, application to diseased tissues improved healing capacity. This may result in part from improved mechanical stability and alleviation of local stresses imparted by the sutures when our material was applied. For both diseases, total inflammation was identical whether dendrimer:dextran was applied or not, further supporting the role of mechanical stability in the differential healing responses.

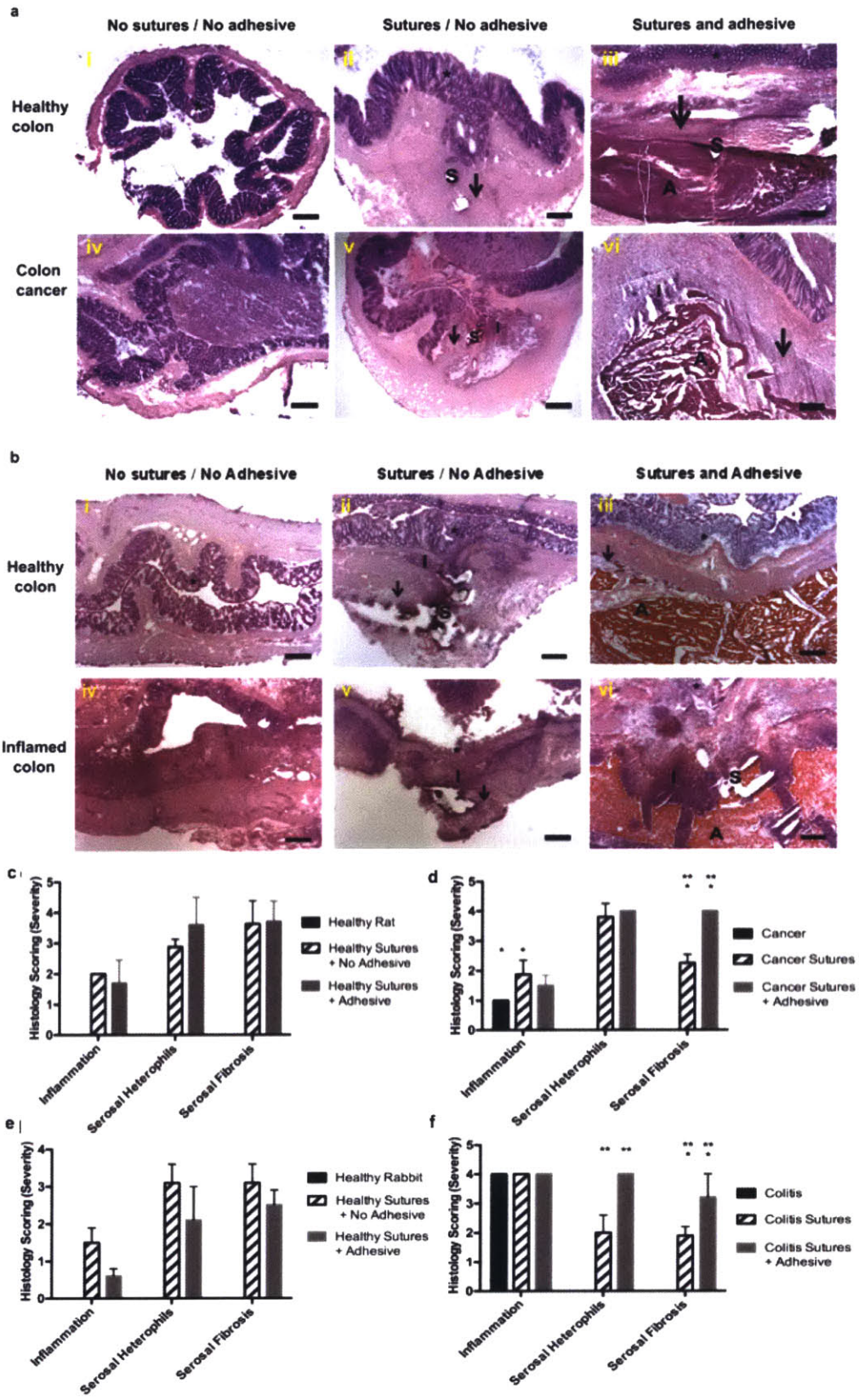
a
No sutures / No adhesive
Sutures / No adhesive
Sutures and adhesive
Healthy colon
Colon cancer
i
ii
iii
iv
v
vi
S
A
b
No sutures / No Adhesive
Sutures / No Adhesive
Sutures and Adhesive
Healthy colon
Inflamed colon
c
Histology Scoring (Severity)
Healthy Rat
Healthy Sutures + No Adhesive
Healthy Sutures + Adhesive
Inflammation
Serosal Heterophils
Serosal Fibrosis
d
Cancer
Cancer Sutures
Cancer Sutures + Adhesive
e
Healthy Rabbit
Healthy Sutures + No Adhesive
Healthy Sutures + Adhesive
f
Colitis
Colitis Sutures
Colitis Sutures + Adhesive

Figure 23. (a) Hematoxylin and eosin (H&E) staining of rat healthy and cancerous tissues without treatment (i and iv), sutural closing of anastomoses site (ii and v) and combination of sutures and adhesive (iii and vi). (b) Hematoxylin and eosin (H&E) staining of rabbit healthy and colitic tissues without treatment (i and iv), sutural closing of anastomoses site (ii and v) and combination of sutures and adhesive (iii and vi). Histological scoring of inflammation, serosal heterophils, and serosal fibrosis in the case of (c) healthy and (d) cancerous rat tissues and (e) healthy and (f) colitic rabbit tissues (N=5 for each experimental group). In each graph, data marked with the same symbol represents statistical significance, with $P<0.05$.

Conclusions

Our data revealed the profound effect of pathological states on tissue:biomaterial interactions and material performance and increased our understanding of how biological forces manifested by disease type and severity affect dendrimer:dextran adhesive performance. With a predictive model to account for those changes, we could rationally tune our material's adhesive strengths to be comparable to those of healthy tissue. Furthermore, changes in the tissue microenvironments altered dendrimer:dextran performance in our colon cancer and colitis models relative to healthy tissues, suggesting that an understanding of the diseased tissue microenvironment is key for successful translation.

An understanding of tissue:material interactions provides new vistas for materials research and characterization of therapeutic potential. Other materials and pathologies might display determinant factors that differ from those of our model adhesive hydrogel. For instance, materials that undergo oxidative degradation will degrade faster in the tumor environment as a result of an elevation in the concentration of reactive oxygen species. Similarly, natural materials that undergo

enzymatic degradation will degrade differentially depending on the enzyme concentrations in an inflammatory environment relative to the basal healthy state.

Leveraging disease cues, one can program materials to impart selective treatments while reporting on disease states. The next chapter focuses on exploiting the pathological cues of TNBC to design a pro-drug capable of sensing the microenvironment and provide selective treatment to cancer cells.

CHAPTER 4: Synthesis and mechanistic insights of a disease-specific dendritic pro-drug

Introduction

Tissues and cells are transient entities, capable of altering their surroundings – protein and enzyme concentrations, pH, redox potential, oxygenation, inflammation and tumor immunity – in response to pathology (see Figure 3). These pathophysiological variations are profoundly manifest in cancer, where the complex tumor microenvironment exhibits several cell types, tissue chemistry and morphology, as well as mechanical stresses that are altered by local pathology with respect to normal tissues (95). Disease-specific stimuli, such as pH (96), proteases (MMPs) (97), phospholipases ($sPLA_2$) (98, 99) or nucleic acids (100), amongst others, have indeed been exploited to allow triggered and targeted drug release.

This concept is the stepping-stone for the development of smart material platforms that can sense the tumor environment, enhance tissue repair and report on tumor state. By understanding tissue microenvironment and its interactions with materials, we can now exploit material design to sense tissue state, interact in a diferential manner and provide a disease specific treatment. The resulting materials must be based on flexibly tunable 'platforms' that can be modified to meet even the most-subtle tissue changes due to disease type and state, as showed in Chapter 2 and Chapter 3. The ultimate goal is to create systems capable of potentiating the development of individualized therapy based on the patient's biological information within the biomolecular cancer profiling.

Biomaterials have been increasingly used as vehicles for intravenous delivery of chemotherapeutic agents to improve cargo protection, avoid rapid clearance and increase

circulation time. Although systemic targeting enables tumor accumulation due to the enhanced permeability and retention (EPR) effect (101), recent efforts have been focused on enhancing vehicle accumulation at the tumor site by adding moieties to actively target tumor cells (102-104). However, these targeting moieties are not necessarily selective to cancer cells only, and may affect healthy cells in surrounding tissues, eliciting undesired toxicity. All of these efforts only marginally improve cargo bioavailability. Hence, the goal of this work is to design and characterize an injectable and degradable hydrogel that would release drug selectively and locally to cancer cells in a sustained manner.

Dendrimers have been used as effective vehicles for delivery of drugs and genetic material owing to their ability to enter cells and escape the endosome (105-107). However, dendrimers are associated with high levels of toxicity and inability to discern healthy and tumor cells (67). In order to overcome some of these potential drawbacks, dendrimers can be derivatized with molecules that provide specific cancer cell targeting, such as folic acid (108) or epidermal growth factor (EGF) (109) to deliver a range of chemotherapeutic drugs (110-112). However, none of these pro-drugs have been shown to be selectively uptaken by cancer cells. We focused on deciphering the underlying mechanism behind the uptake of these dendritic vehicles and elucidating proper material design to provide controlled and selective internalization of the dendritic pro-drug.

EGFR expression is upregulated in multiple cancer types, such as breast, head and neck, cervical, ovarian, bladder, esophageal, endometrial, lung or colorectal, which in most cases is correlated with increased recurrence-rate and reduced overall survival (113). We explored the effects of the ligand's type (i.e. full growth factor, EGF, versus EGFR-binding synthetic peptide) on cellular uptake via receptor-mediated endocytosis (RME). PAMAM dendrimer generation 5 was conjugated with either EGF – one of the natural ligands of EGFR – or a small synthetic peptide that binds to the EGF receptor (EGF mimicking peptide – EGFmp) (114) to achieve RME

(Figure 24a). It has been reported that nanoparticles capable of simultaneous stimulation of multiple receptors on the surface of cells can elicit RME (60). We hypothesized that similarly to nanoparticles, dendrimers conjugated with multiple copies of a ligand for EGFR would enhance RME in cancer cells, where the high density of receptors on the surface would prompt numerous stimulation points. On the contrary, these conjugates would not elicit RME in healthy cells owing to their basal levels of EGFR (Figure 24b).

TNBC is routinely treated with anthracycline/taxane chemotherapy-based regimens as neoadjuvant therapies (115). We have used an anthracycline drug, doxorubicin, as a model for the dendritic pro-drug. Doxorubicin has been conjugated to various biomaterials, such as AffiGel 701 (116), polyvinyl alcohol (117), micelles (118) and dendrimers (119) through an aconityl linker and has been reported to possess acid-sensitive release in the lysosomal compartment.

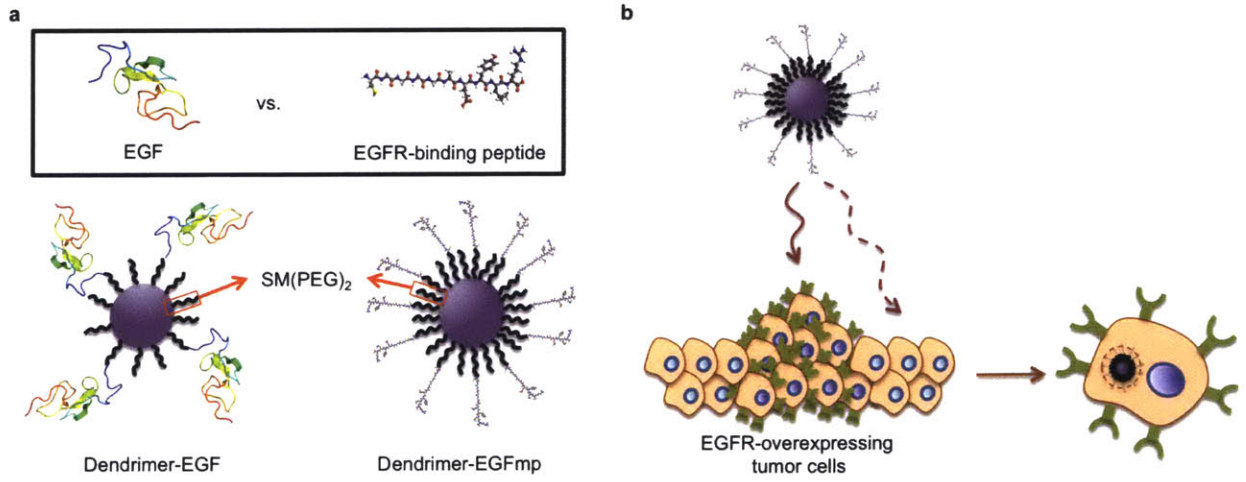

Figure 24. (a) PAMAM dendrimer generation 5 was conjugated to either human EGF or EGFR-binding peptide (EGFpep). (b) These conjugates can elicit selective receptor mediated endocytosis in EGFR-overexpressing breast cancer cells while avoiding uptake by healthy cells around them.

In this chapter, we develop a dendritic pro-drug that can selectively enter cancer cells and escape the endosome. We studied the uptake mechanisms and showed that while naked dendrimer follows multiple uptake mechanisms and exhibits high toxicity both in cancer and healthy cells, the dendrimer-EGFmp was highly biocompatible and exclusively internalized by EGFR overexpressing cancer cells, leaving healthy cells intact. In contrast, dendrimer-EGF utilizes multiple internalization mechanisms and hence it is not selective to EGFR overexpressing cells. We also showed that the dendritic pro-drug has cancer-specific cytocidal effect, while the same concentration of free doxorubicin elicited indiscriminate toxicity in healthy and cancer cells. Based on the findings reported here, dendritic pro-drugs can be leveraged to impart selective delivery of high chemotherapeutic drug dose to cancer cells, avoiding healthy tissue damage – a hallmark of systemic chemotherapy. The approach described in this work and the concepts learned from these experiments can be generalized to design an array of dendritic pro-drug vehicles capable of harnessing other commonly over-expressed receptors in cancer, such as VEGFR or FGFR-2.

Results and Discussion

Cell line characterization

To validate the selectivity of our conjugates towards EGFR overexpressing cancer cells we studied the conjugates uptake and therapeutic effect in a breast cancer cell line overexpressing the EGF receptor (MDA-MB-468) and in a healthy mammary epithelial cell line (HMEpC). We corroborated the differential receptor expression between these two cell lines by immunostaining and Western Blot against EGFR (Figure 25a-c). We quantified EGFR expression by reverse transcription polymerase chain reaction (RT-PCR) and found that MDA-MB-468 cells express more EGFR (2-fold) than HMEpC (Figure 25d).

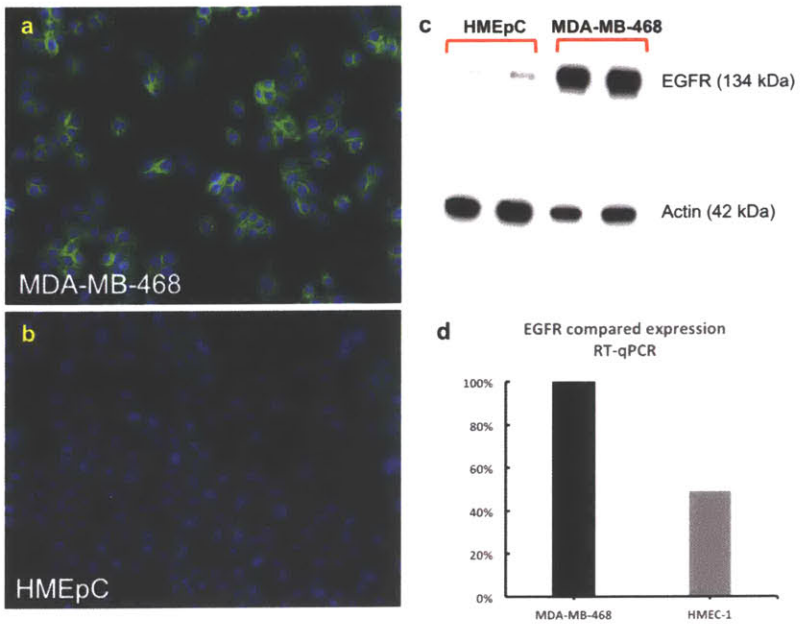

Figure 25. Immunostaining against EGFR of (a) EGFR-overexpressing breast cancer cells (MDA-MB-468) and (b) healthy cells (HMEpC) with basal levels of EGFR. Differential expression was corroborated and quantified by (c) Western Blot and (d) RT-PCR.

Dendrimer-peptide conjugates are stable and enable higher peptide density on their surface

Fluorescently labeled PAMAM dendrimer generation 5 was conjugated to either EGF or EGFmp through a PEGylated amine-to-sulfhydryl crosslinker ($SM(PEG)_2$) (Figure 26a). The PEGylated crosslinker density on the surface of the dendrimer was determined by Ellman's assay by reacting an excess cysteine to the terminal maleimide groups and measuring the unreacted excess cysteine. Successful peptide and EGF conjugation was corroborated by UV-VIS spectroscopy, which showed an increase in absorbance at 280 nm, originating from the aromatic amino acids present both in the peptide and EGF (Figure 26b-c). We calculated the ligand to dendrimer ratios as the quotient EGF or peptide concentrations (measured from their absorbance contributions at 280 nm) and dendrimer concentration (determined from the absorbance of the fluorescent tag at 594 nm, See Materials and Method section for detailed calculations), as well as by Ellman's assay

of the unreacted EGF or peptide. The substantially lower molecular weight and volume of EGF mimicking peptide (1.1 kDa, linear sequence) with respect to EGF (6.2 kDa, tertiary bulky structure), allowed for a higher peptide conjugation efficiency per dendrimer (~40 peptides) compared to that of EGF (~5 proteins).

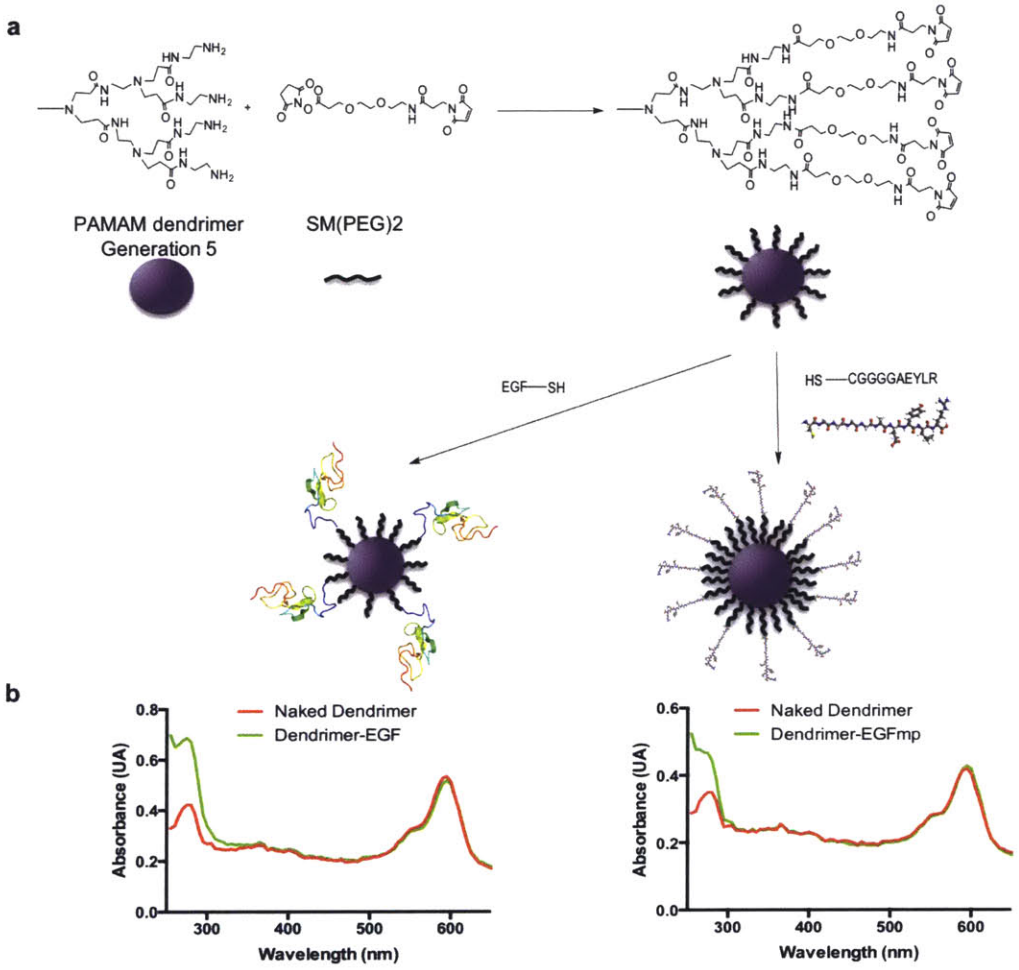

Figure 26. (a) PAMAM dendrimer generation 5 was conjugated to either EGF or EGFR-binding peptide through a PEGylated linker ($SM(PEG)_2$). UV-VIS spectra of naked dendrimer and conjugates showed an increase in absorbance at 280 nm correspondent to the aromatic amino acids present in (b) EGF and (c) peptide.

Dynamic Light Scattering (DLS) was employed to report on conjugates size. Both dendrimer-EGF and dendrimer-EGFmp showed an increase in hydrodynamic diameter with respect to the naked dendrimer (mean diameters of 6.18 ± 1.33, 9.46 ± 0.98 and 7.31 ± 1.16 nm for naked dendrimer, dendrimer-EGF and dendrimer-EGFmp, respectively; Figure 27a). Even though both conjugates have roughly the same size, dendrimer-EGF conjugates form aggregates of 9.86 ± 1.69 μm in diameter (arrows in Figure 27a). Moreover, DLS studies of dendrimer-EGF conjugates a week post-reaction showed an increase in size distribution of the main peak at 9.46 nm, as corroborated by the increase in standard deviation, as well as the appearance of other peaks of varying sizes – 63.16 ± 13.17 nm, 612.33 ± 94.44 nm and 4.59 ± 0.64 μm – indicating conjugate degradation (Figure 27b). After one week, naked dendrimers also form aggregates that could be dissolved by sonication, and hence are most likely formed by electrostatic interactions (Figure 27c). High-resolution cryo-TEM showed discrete naked dendrimer and dendrimer-EGFmp particles of 4.2 nm and 5.6 nm in diameter, respectively (solid arrows, Figure 27d-e). Images of dendrimer-EGF conjugates show two distinct populations; aggregates (area delineated with a dashed line in Figure 27f) and discrete particles of 8.7 nm in diameter (solid arrows in Figure 27f). This correlates with the observations gathered from DLS experiments regarding aggregates formation and corroborates the lower stability in solution of dendrimer-EGF conjugates.

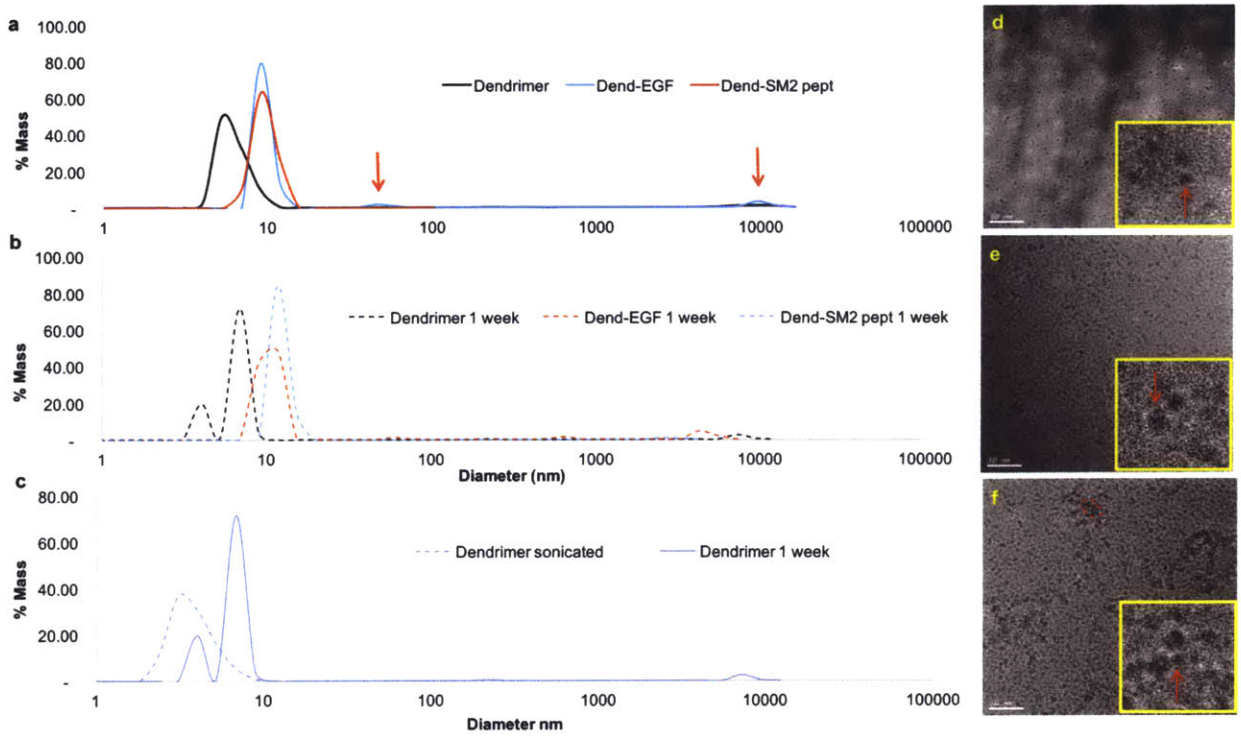

Figure 27. (a) Dendritic conjugates showed an increase in diameter with respect to the naked dendrimer. Dendrimer-EGF also exhibited peaks at higher diameters, indicating the formation of aggregates (red arrows) (b) Dendrimer-peptide was demonstrated to be more stable in solution after a week than dendrimer-EGF, which showed an increase in size distribution. (c) Naked dendrimer also forms aggregates after a week in solution that are disrupted by sonication. The size and structure of (d) naked dendrimer, (e) dendrimer-EGFmp and (f) dendrimer-EGF was corroborated by high-resolution cryo-TEM (red arrows indicate discrete particles; area encircled by a dashed line shows dendrimer-EGF aggregates).

Synthetic peptides allow for EGFR interaction without pathway activation

Next, we studied whether the dendritic pro-drug was capable of triggering the EGFR signaling pathway through its interaction with the EGF receptor. EGFR signaling pathway induces growth, differentiation, migration, adhesion and cell survival through various interacting signaling pathways. It is critical for the design of chemotherapeutic pro-drugs utilizing this receptor to

ensure this pathway is not triggered, leading to further cancer cell proliferation and survival, which could counteract the effects of the chemotherapeutic drug. Western Blot studies showed that full EGF, both on its own and conjugated to the dendrimer, triggered EGFR pathway, as shown by the presence of a band corresponding to the phosphorylated form or EGFR (Figure 28a,c). On the contrary, the synthetic peptide did not elicit EGFR phosphorylation when cells were dosed with the free peptide or the dendritic conjugate (Figure 28b,c). Moreover, the number of peptide copies (20 or 60 copies) conjugated to the dendrimer did not affect EGFR phosphorylation (Figure 28). These results corroborate one of the advantages hypothesized about the use of synthetic peptides over full proteins – the ability to be synthesized to interact avidly with receptors without eliciting the response of the actual biological ligand.

We also explored the relative affinity of EGF and EGF mimicking peptide for the receptor, and investigated whether the peptide was an antagonist that could potentially block the receptor from EGF-mediated activation. EGFR-overexpressing cancer cells were incubated with a mix of EGF and peptide and EGFR activation was also assessed by Western Blot, as described above. The results showed that the EGF mimicking peptide does not behave as an EGF antagonist, as evident by the phosphorylated EGFR bands observed, regardless of the relative concentrations of growth factor and peptide (Figure 28d).

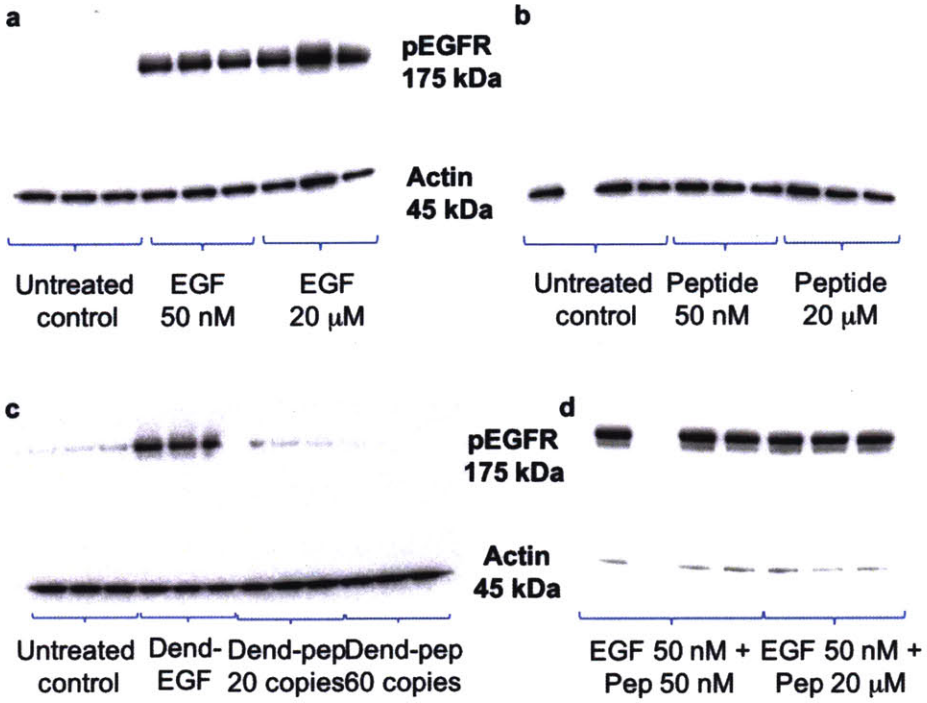

Figure 28.Images of Western Blot gels showed bands corresponding to phosphorylated EGFR when cells were incubated with (a) free EGF, but none were observed with (b) free peptide. (c) The corresponding conjugates followed same trend same trend, with dendrimer-EGF but not dendrimer EGF-mp activating the pathway. (d) The EGF mimicking peptide did not block EGF-mediated EGFR pathway activation. Actin was used as an internal control in all gels (band at 45 kDa).

Deciphering the uptake mechanism and potential selectivity of dendrimer conjugates

Next, we studied the cellular uptake mechanism of the dendritic pro-drug and investigated the selectivity of these conjugates towards EGFR-overexpressing breast cancer cells compared to mammary epithelial cells as a model for healthy cells surrounding the tumor. EGFR-overexpressing MDA-MB-468 cells were incubated with fluorescently labeled naked dendrimer, dendrimer-EGF or dendrimer-EGFmp at 37°C or 4°C for 5 hours to assess intracellular uptake. Uptake at 4°C was conducted to examine whether uptake occurs via energy-independent

processes, as energy-dependent processes such as RME are inactive at 4ºC. Conjugates' uptake was differentially reduced as a function of treatment (Figure 29a-h). Despite shutting down energy-dependent uptake mechanisms, naked dendrimers' internalization at 4ºC was still evident, pointing towards both energy-dependent and independent internalization mechanisms, as previously described (120). Nanoscale hole formation is thought to take place through interactions between the positive charges on the surface on the dendrimer and the cell membrane. Indeed, high uptake of naked dendrimer is observed in HMEpC (Figure 29j), owing to nanoscale hole formation, which is minimized in the case of the modified dendrimer conjugates (Figure 29k-l). Taken together, these data suggest that both dendrimer-EGF and dendrimer-EGFmp are being uptaken into cells through energy-dependent mechanisms selective to the cancer cells of study.

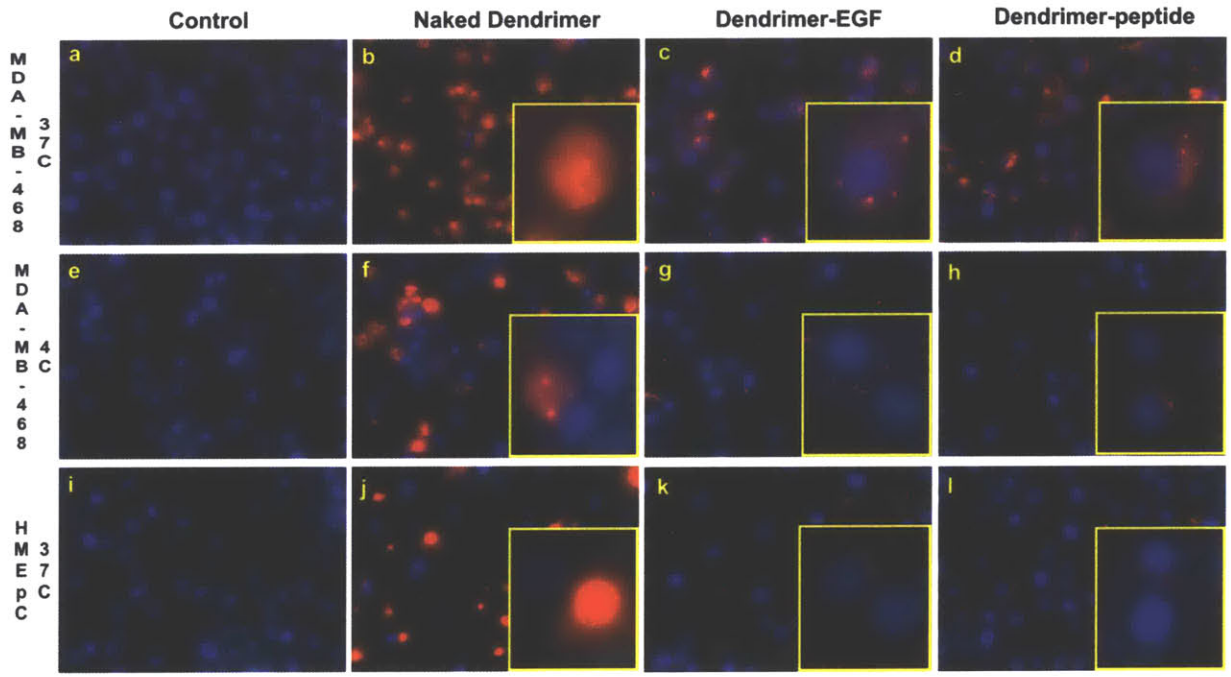

Figure 29. Fluorescence microscopy images of untreated controls, naked dendrimer and dendritic conjugates in MDA-MB-468 breast cancer cells at 37°C (a-d) and 4°C (e-h), and healthy HMEpC (i-l). Dendrimers were tagged with AlexaFluor-594 and nuclei stained with DAPI. Images were taken at 10X magnification.

Flow cytometry data corroborated the energy-independent mechanism of dendrimer conjugates (Figure 30). While naked dendrimer uptake is extensive in EGFR overexpressing cells at 37°C (mean fluorescence/cell $1.12x10^5 \pm 9.1x10^4$), dendrimer conjugates showed a more moderate uptake (mean fluorescence/cell dendrimer-EGFmp $5.1x10^3 \pm 5.4x10^3$ and dendrimer-EGF $2x10^3 \pm 2.9x10^3$, Figure 30a and d). Uptake at 4°C was reduced in all cases, however the decrease was more significant in the case the dendritic conjugates, with levels of uptake comparable to those of the untreated controls (mean fluorescence/cell dendrimer-EGFmp 40 ± 40; dendrimer-EGF $1.4x10^2 \pm 4.5x10^2$ and untreated control 43 ± 43; Figure 30b and d). Naked dendrimer uptake was significantly reduced at 4°C compared to that of 37°C, but still maintained high levels compared to its conjugated counterparts ($1.7x10^4 \pm 1.8x10^4$ at 4°C compared to $1.1x10^5 \pm 9.1x10^4$ at 37°C), corroborating that dendrimers are internalized via a combination of mechanisms, both energy-dependent and independent, as previously reported (120). Dendrimer conjugates showed a decrease in uptake in HMEpC, with more pronounced reduction in the case of dendrimer-EGFmp (dendrimer-EGFmp $5.1x10^2 \pm 4.9x10^2$ and dendrimer-EGF $9.4x10^2 \pm 8.2x10^2$; Figure 30c and d). This suggests that dendrimer-EGFmp is being internalized solely through energy-dependent mechanisms more specific to MDA-MB-468 breast cancer cells than healthy HMEpC.

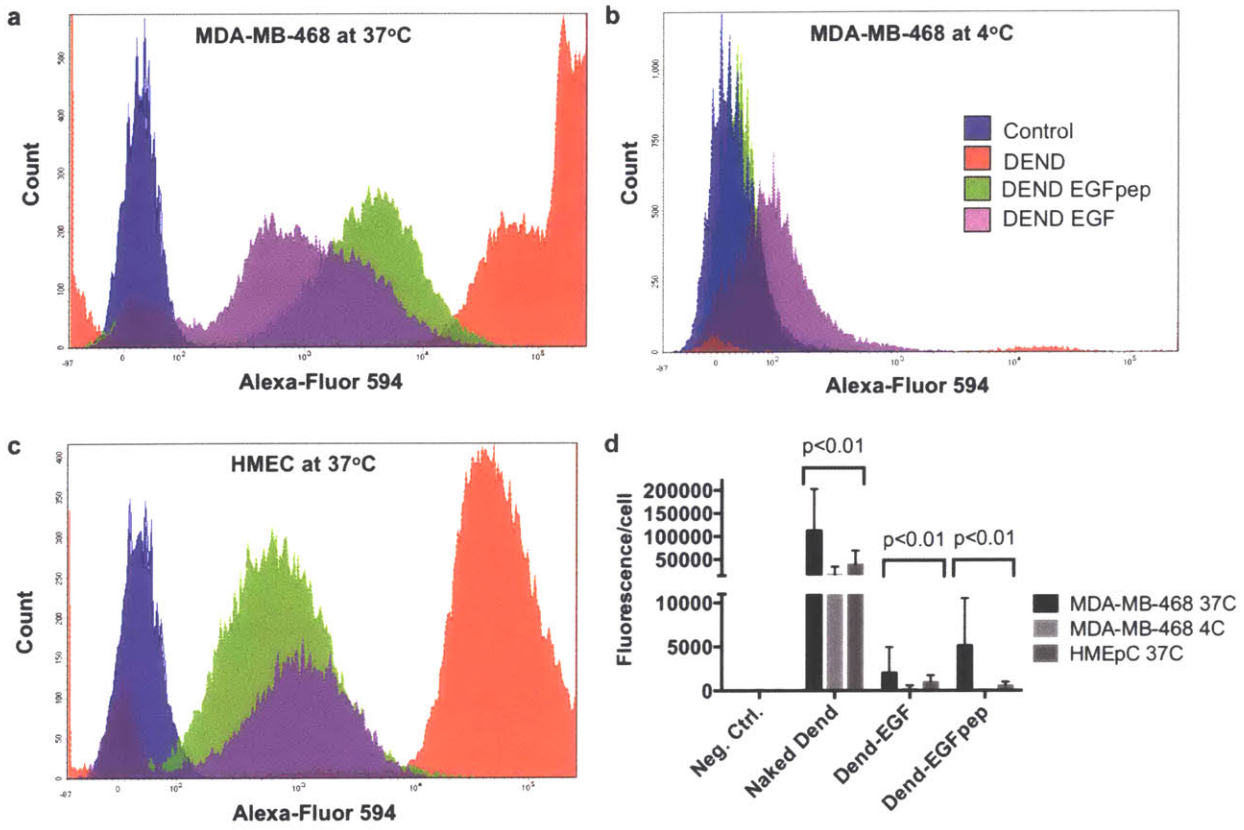

Figure 30. FACS analysis of naked dendrimer and dendritic conjugates uptake in MDA-MB-468 cells at (a) 37°C and (b) 4°C and in HMEpC (c). (d) Mean fluorescence per cell and standard deviations for each treatment and cell line.

Next, we corroborated that the observed energy-dependent uptake by the dendritic conjugates was indeed EGFR-mediated. For this purpose, EGFR was blocked with a neutralizing antibody prior to MDA-MB-468 incubation with the different dendrimers (Figure 31a-c). Naked dendrimer and dendrimer-EGF uptake were not altered by receptor neutralization (Figure 31a-b), while dendrimer-EGFmp internalization was completely abrogated (Figure 31c), hence indicating exclusive EGFR-mediated uptake. Indiscriminate uptake of naked dendrimer is independent of cell type and treatment. Data observed by epi-fluorescence microscopy correlated with flow cytometry results (Figure 31d-e).

We then investigated whether the dendrimer-EGF non-specific uptake following EGFR neutralization was due to alternative EGF uptake mechanisms or a result of the chemical modification during the conjugation process. To examine the specificity of EGF uptake through EGFR, MDA-MB-468 cells were incubated with free, labeled EGF. These cells internalized EGF in the absence of neutralizing antibody (Figure 31f). However, we observed a total abrogation of EGF uptake when the receptor was inactivated (Figure 31g), pointing at its specificity for the EGF receptor. We hypothesized that EGF modifications during the conjugation reaction could alter EGF tertiary structure, potentially activating other internalization mechanisms. TCEP-treated EGF was indeed internalized after blocking EGFR (Figure 31i), but to a lesser extent than without receptor neutralization (Figure 31h). We also studied whether incomplete EGF coverage of the PEGylated dendrimer may lead to non-specific uptake through other internalization mechanisms. Indeed, the intermediate PEGylated dendrimer and the dendrimer-EGF have comparable levels of cellular internalization, as determined by flow cytometry (Figure 31j).

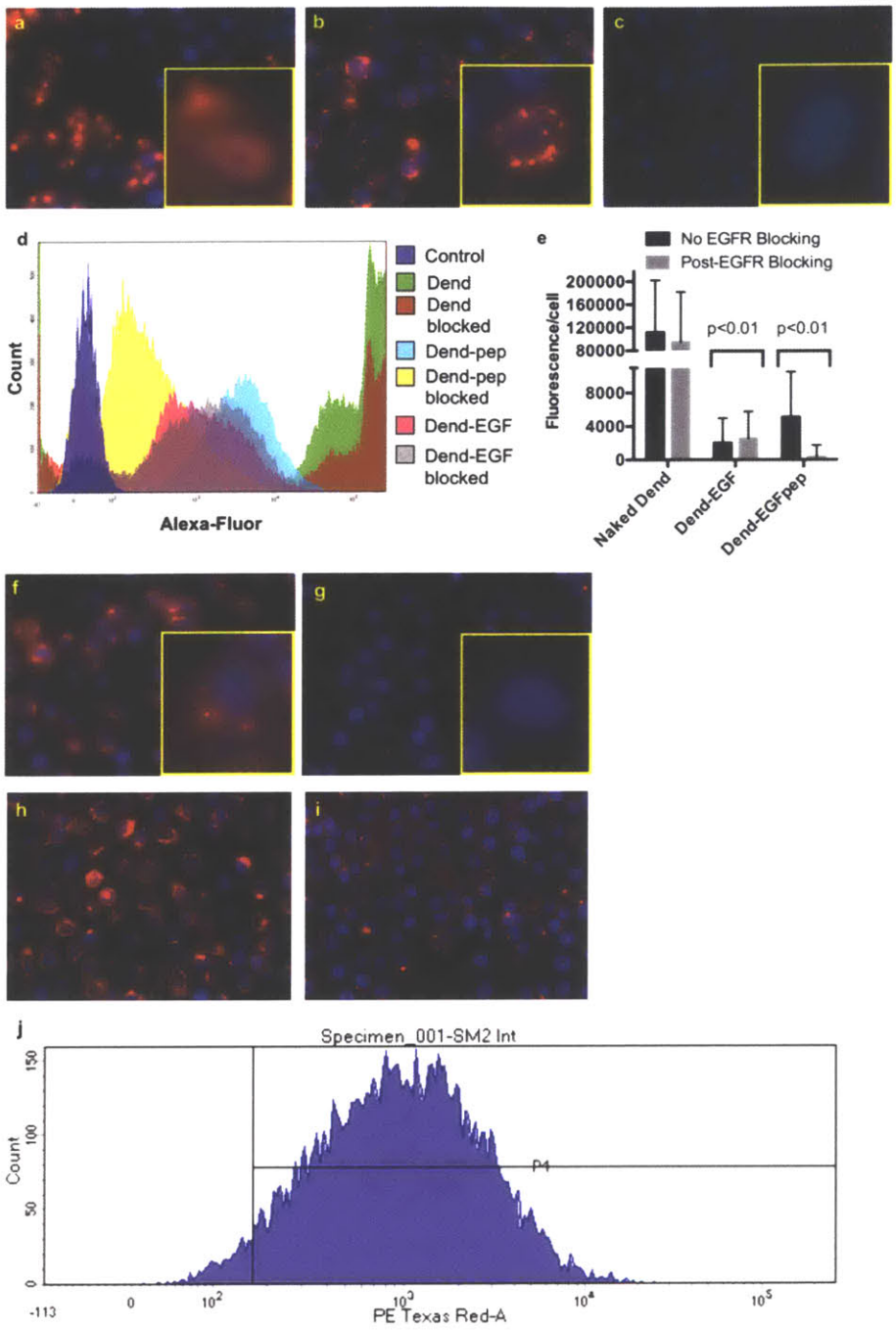

Figure 31. Fluorescence microscopy images of MDA-MB-468 treated with either (a) naked dendrimer, (b) dendrimer EGF or (c) dendrimer peptide after blocking EGFR with a neutralizing antibody. (d) FACS analysis of naked dendrimer and dendritic conjugates uptake in MDA-MB-468 with and without receptor blocking. (e) Mean fluorescence per cell and standard deviations for each treatment and cell line. (f) Free EGF was uptaken by MDA-MB-468 cells, (g) but uptake was

abrogated when the receptor was blocked. (h) TCEP-treated free EGF was uptaken by MDA-MB-468. (i) Cellular internalization of TCEP-treated free EGF was reduced but not abrogated when EGFR was blocked, corroborating alternative uptake mechanisms. (j) PEGylated intermediate also exhibited uptake levels similar to those of the dendrimer-EGF, as evident by similar fluorescent distribution by FACS. Dendrimers were tagged with AlexaFluor-594 and nuclei stained with DAPI. Images were taken at 10X magnification.

Dendritic pro-drug cancer-specific cytocidal effect and intracellular fate

We investigated the cancer-specific cytocidal effect associated with the dendritic pro-drug both in healthy and cancer cells. Doxorubicin was conjugated to the dendrimer-peptide through an aconityl linker (Figure 32a), reported to be pH sensitive, to form the dendritic pro-drug. UV-VIS studies of the conjugates showed successful conjugation of an average of 8 doxorubicin molecules per dendrimer (Figure 32b). More interestingly, at equal concentrations of doxorubicin measured by UV-VIS, fluorescence of the drug conjugated to the dendrimer decreased 9-fold compared to that of the free drug (Figure 32c). The observed fluorescence quenching is most likely caused by the local basic pH imparted by the dendrimer, as doxorubicin fluorescence has a strong dependence with pH. Karukstis et al. (121) reported a 12-fold decrease in doxorubicin's fluorescence between pH 5.52 and 10.40, further corroborating the observed findings in the dendritic pro-drug. We employed dendrimer-conjugated doxorubicin's fluorescence quenching to study pH-triggered release. In vitro release data at pH 7.4 and 5.5 did not show any changes in fluorescence intensity over the course of 48 hours compared to free doxorubicin-aconityl (Figure 32d), suggesting that the pH-sensitive aconityl linker does not get cleaved at acidic pH, as previously reported. We then investigated whether doxorubicin could be released in a cellular environment, where there are more elements at play rather than just pH (e.g. proteases). We incubated MDA-MB-468 with dendritic pro-drug and followed fluorescence intensity over time.

Fluorescence microscopy images showed a buildup of dendritic pro-drug on the surface of cells after 2-hour incubation, and accumulation in the nucleus at 6 and 24 hours incubation, with no concomitant increase in fluorescence (Figure 32e-h). These results suggest that doxorubicin does not get cleaved in the intracellular environment, and that the intact dendritic pro-drug is capable of penetrating the nuclear membrane and accumulate in the nucleus.

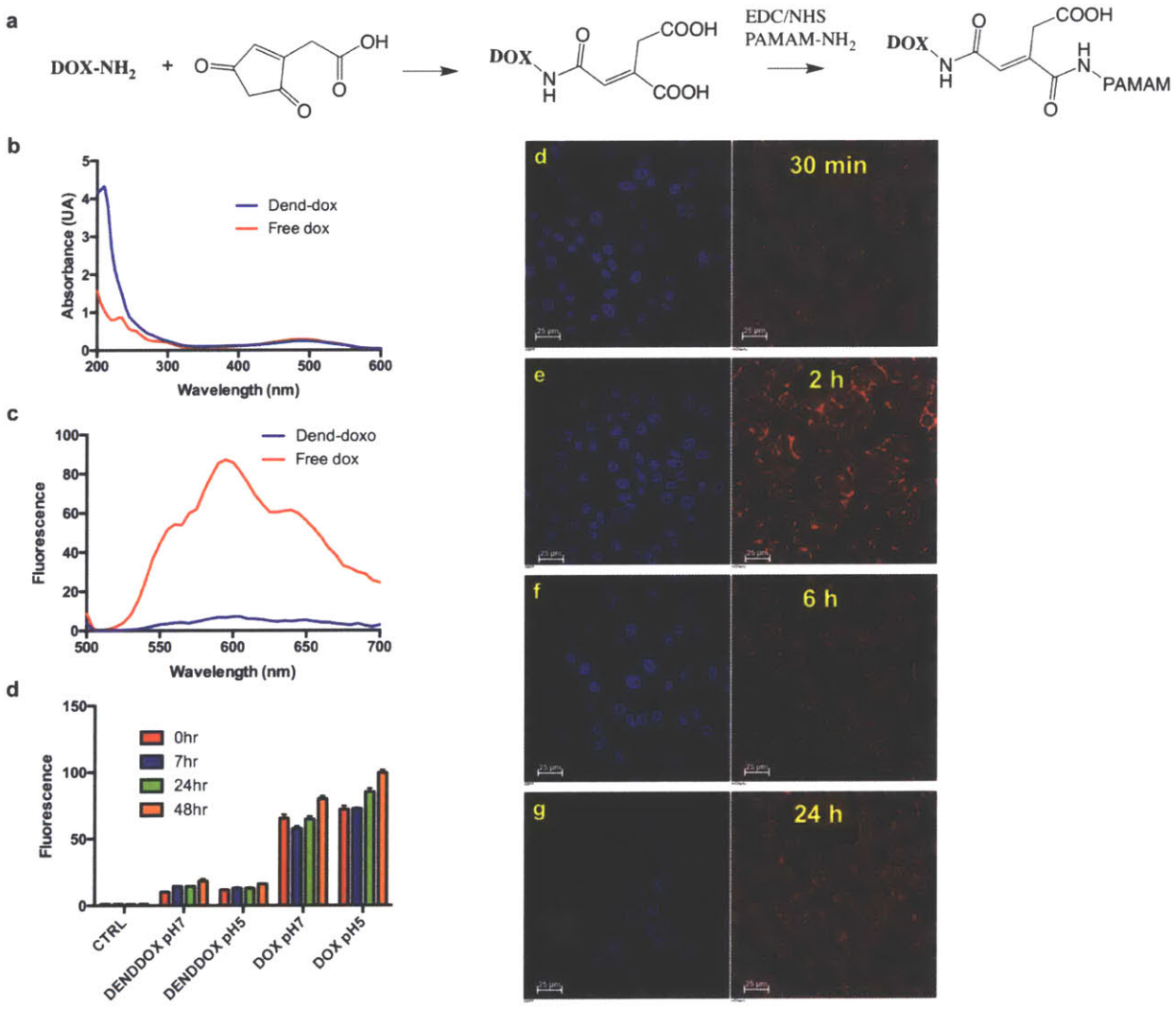

Figure 32. (a) Doxorubicin was conjugated to the dendrimer through an acontityl linker. Doxorubicin's fluorescence quenching was observed when equal concentrations of free and conjugated doxorubicin, as measured by (b) UV-VIS spectroscopy were analyzed by (c)

fluorescence spectroscopy. Conjugated doxorubicin's fluorescence quenching was employed to assess (d) pH sensitivity in vitro using free doxorubicin under the same pH conditions as controls and (e) intracellular fate in EGFR-overexpressing cells over time.

We also investigated the endosomal escape mechanism of the dendritic pro-drug by tracking early and late endosomes and lysosomes over time. Dendritic pro-drug was also tracked owing to its inherent autofluorescence. At early time points (4 and 8 hours), the presence of early endosomes is evident by the green fluorescence observed (Figure 33, top row). At 8-hours incubation, the fluorescence intensity corresponding to late endosomes increases mildly with respect to that of 4 hours, indicating that some of the dendritic pro-drug indeed reaches the late endosome, and most likely escapes it, hence the lower intensity with respect to the early endosome signal (Figure 33, middle row). No substantial evidence of early nor late endosomes are observed at 24 hours, most likely due to receptor internalization and degradation, together with the fact that the internalized dendritic pro-drug escaped the late endosome, as discussed above. No evidence of lysosomes is observed at early time points, consistent with the data obtained suggesting late endosomal escape. However, high lysosomal fluorescence signal was recorded at 24 hours (Figure 33, bottom row). This phenomenon is most likely due to lysosome-dependent apoptosis (122), as doxorubicin is known to induce the lysosomal pathway of apoptosis in cancer cells (123).

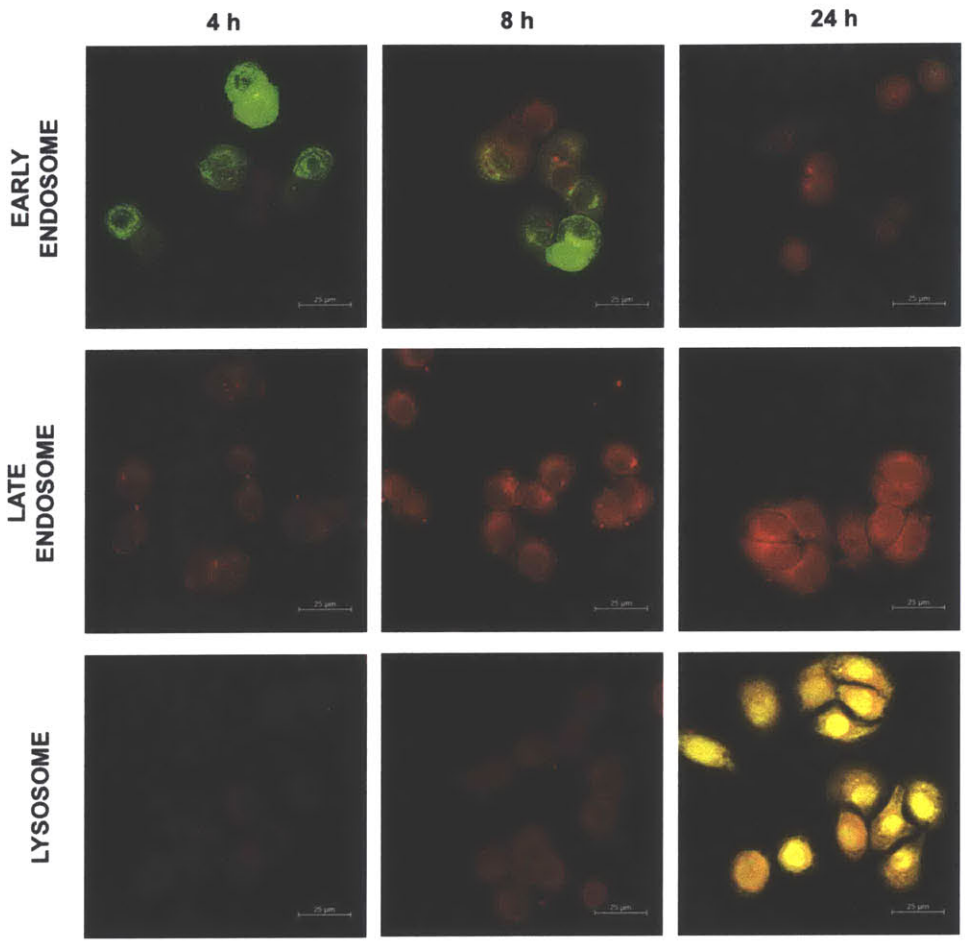

Figure 33. Early and late endosome and lysosome tracking of dendritic pro-drug in MDA-MB-468 cells over time. Endosomes were labeled prior to pro-drug incubation with CellLight Early or Late Endosomes-GFP, BacMam 2.0 (top two rows) and lysosomes were stained with LysoTracker Green DND-26 after cells fixation (bottom row). Dendritic pro-drug was tracked owing to its autofluorescence. At 4-hours incubation, there is evidence of early endosomes (green, top row), but not of late endosomes nor lysosomes. At 8-hours incubation, the late endosome fluorescence increased with respect to 4 hours, but to a lower extent to that observed for early endosomes, suggesting that the dendritic pro-drug escaped the endosome. Lysosome tracker exhibited high fluorescence at 24 hours, probably due to doxorubicin-induced activation of lysosomal pathway of apoptosis.

The next question is, then, whether conjugated doxorubicin still maintains its cytotoxic effect. Dose-dependent studies showed a cancer-specific cytocidal effect in EGFR-overexpressing cancer cells after 48 hours (cell death between 45% and 96%, Figure 34a), while healthy cells exhibited toxicity levels comparable to those of the dendrimer-peptide without the drug (Figure 34b). At a concentration of 10 μM, the dendritic pro-drug had a cytocidal effect of over 90% in cancer cells while not affecting healthy cells, as evident by 100% cell survival (Figure 34c-d). The equivalent free doxorubicin concentration caused over 90% cell death in healthy mammary epithelial cells. Zhu *et al.* reported a decrease in toxicity when dendrimers were PEGylated, owing to lower cellular uptake. However, cytotoxic potency of those conjugates was also dramatically reduced with respect to that of free doxorubicin, with IC50 between 27.83 μM and 138.59 μM (119). By adding the EGF mimicking peptides, our dendritic pro-drug has an IC50 lower than 0.5 μM.

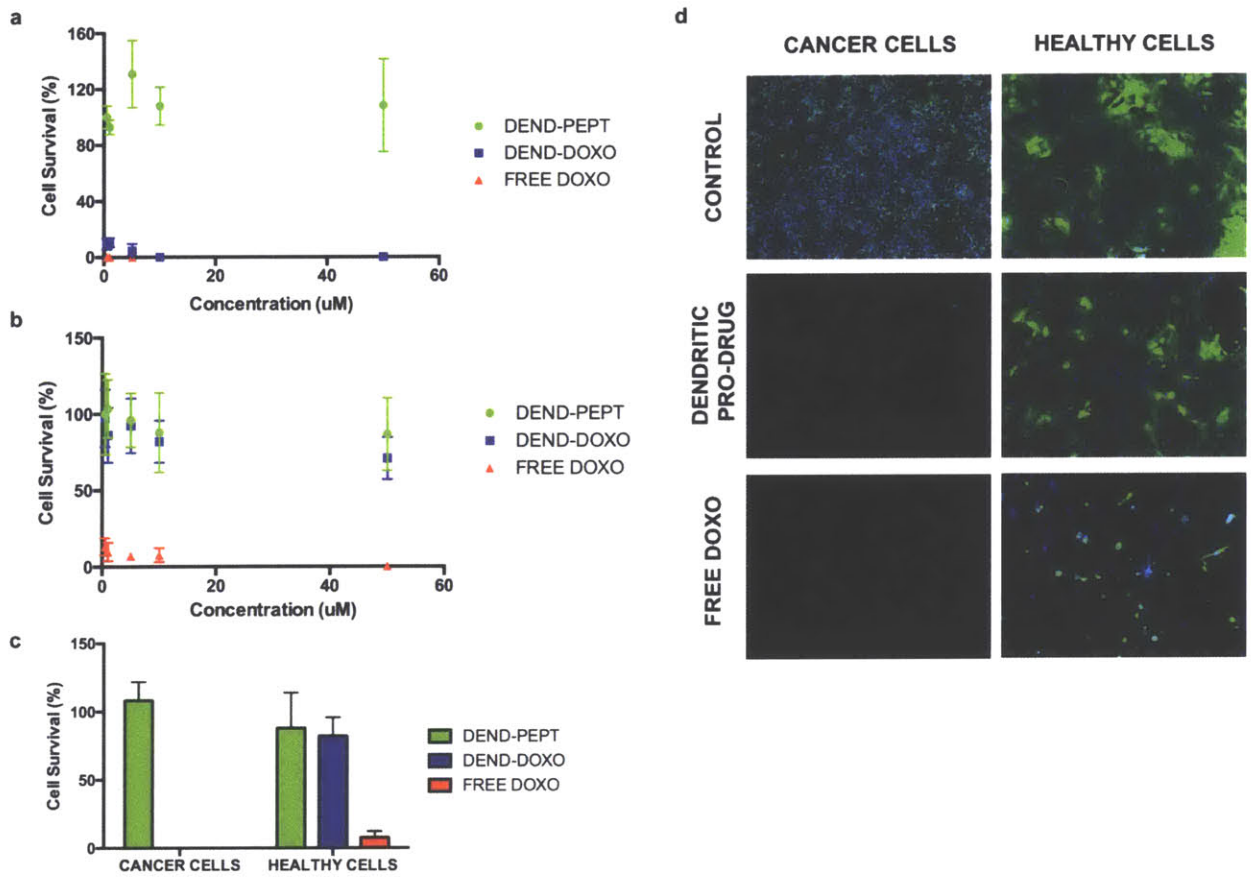

Figure 34. Dose response of (a) EGFR-overexpressing cells and (b) healthy mammary epithelial cells to the dendritic pro-drug. Dendrimer-peptide without drug (vehicle) and free doxorubicin were used as controls. Cytotoxicity was measured as % cell survival with respect to an untreated control. (c) Dendritic pro-drug cancer-specific cytocidal effect at a concentration of 10 μM, compared to equivalent concentrations of dendrimer-peptide without conjugated drug and free doxorubicin. (d) Fluorescence microscopy pictures of EGFR-overexpressing cancer cells and healthy mammary epithelial cells treated with dendritic pro-drug, dendrimer-peptide or free drug at 10 mM concentration. Nuclei were stained with DAPI (blue) and live cells with CellTracker (green).

Dendritic pro-drug-doped hydrogel allows for sustained release and selective uptake in vivo

Fluorescein-tagged dendritic pro-drug was mixed with dendrimer solution 10% solid content and then allowed to cure with fluorescently labeled dextran aldehyde 10% solid content. Pre-cured 6-mm disks of the doped hydrogel were snap-frozen, cryosectioned and analyzed by confocal fluorescence microscopy. Dendritic pro-drug was homogeneously distributed in the hydrogel structure (Figure 35a), as evident by the presence of green fluorescence dye throughout the scaffold in blue. Three-dimensional rendering of the hydrogel scaffold revealed tortuous and irregular pores of over 100 μM in diameter (Figure 35b). Release experiments showed dual kinetics – first a burst release of approximately 50% of the total dendritic pro-drug load, followed by a sustained release over three weeks (Figure 35c). This data suggests that the unbound complexes diffuse out of the hydrogel scaffold through the big pores, while complexes cross-linked to the scaffold are released as the material degrades over time, as evident by the non-linear correlation between the dendritic pro-drug release and the square root of time (insert in Figure 35c). Interestingly, the final concentration of dendritic pro-drug in the scaffold (25 or 50 μM) did not affect the release profile in terms of percent complex released over time, nor the degradation rate of the scaffold.

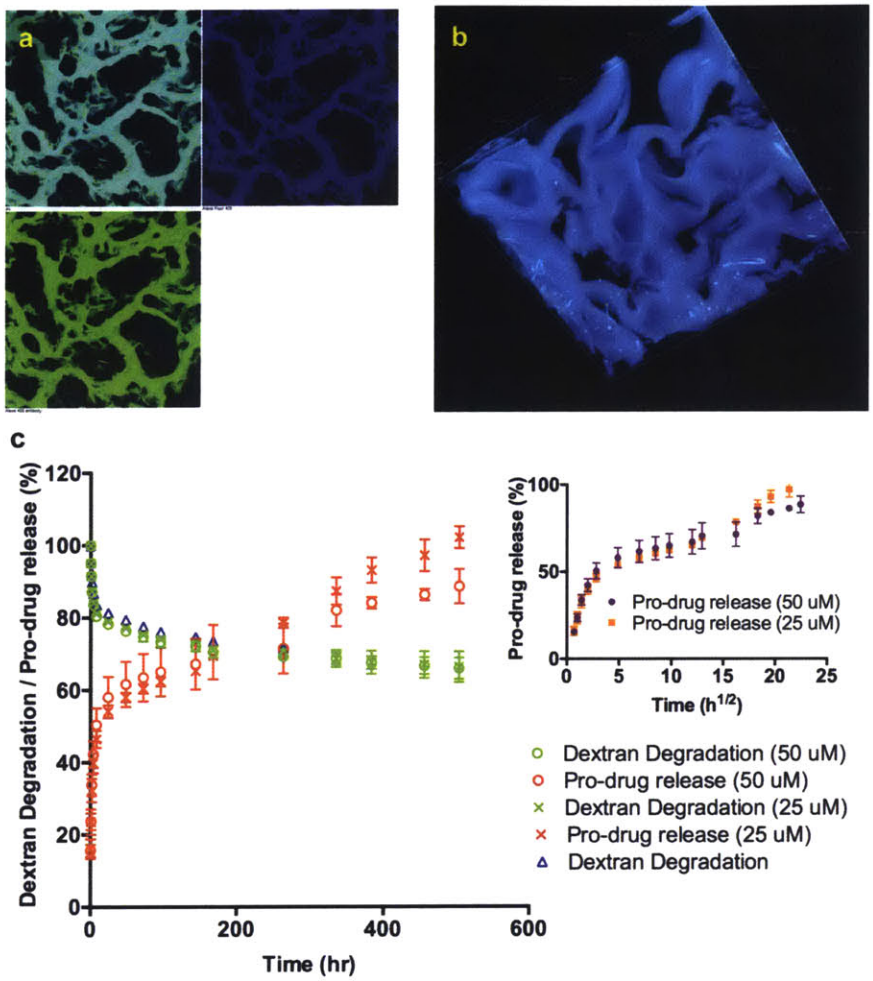

Figure 35. (a) Confocal microscopy image and (b) 3D rendering of the adhesive hydrogel doped (tagged with AlexaFluor 405, blue) with dendritic pro-drug (tagged with fluorescein, green) showing the microscopic structure of the hydrogel and the homogeneously distributed pro-drug in the scaffold. (c) Hydrogel scaffold degradation, measured as dextran release, and pro-drug release at initial concentrations of 25 and 50 μM. The insert graph shows pro-drug release as a function of $t^{1/2}$, proving that the release if not purely diffusion-driven.

Finally, we tested whether the selective uptake observed in vitro was maintained in the in vivo setting. Mice were injected with 100 μl of dendrimer:dextran doped with 50 μM labeled dendritic pro-drug intratumorally and the uptake was assessed after 72 hours. Cryosections of the tumor

and healthy tissue (T) in intimate contact with the material (M) were analyzed by confocal fluorescence microscopy and co-localization studies were performed. Immunostaining against EGFR was performed on the sections to detect tumor cells (green), and dendritic pro-drug was fluorescently labeled (red). EGFR-overexpressing tumor cells showed dendritic pro-drug uptake (Figure 36a; Pearson's R value 0.73 tM=0.888, Costes P-Value 1.00), while healthy tissues with basal levels of EGFR, as evident by the lower fluorescent intensity in the green channel, did not uptake the pro-drug (Figure 36b; Pearson's R value -0.49, tM=0.003, Costes P-Value 1.00). This data corroborates that the selective uptake observed in vitro is maintained in vivo in a murine model of breast cancer.

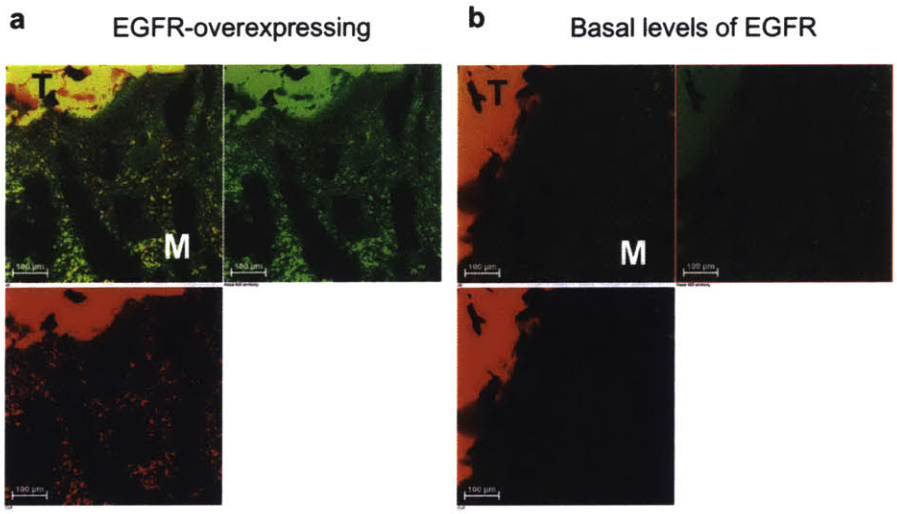

Figure 36. Confocal microscopy images of tumor and healthy surrounding tissues (T) adjacent to the material (M). (a) EGFR-overexpressing tumor cells (green, AlexaFluor 488 secondary antibody) co-localized with dendritic pro-drug (red, Cy5), while (b) healthy cells with basal levels of EGFR did not uptake the pro-drug.

Conclusions

Chemotherapy is an effective cancer treatment modality. However, side effects are extremely devastating for patients owing to non-cancerous cells toxicity. The development of a pro-drug that

can direct these small molecules towards cancer cells, while evading healthy cells in surrounding tissues is of vital importance to achieve powerful and selective treatment. Here, we have developed a pro-drug molecule based on PAMAM-dendrimer generation 5 core decorated with synthetic EGFR-binding peptides that can elicit RME selectively in EGFR over-expressing cancer cells, while maintaining healthy cells with basal levels of EGFR intact. We have proved that the use of synthetic peptides is associated with higher pro-drug stability in solution and higher and more selective uptake through EGFR. Moreover, synthetic peptides can interact with growth factor receptors and elicit RME without activating the downstream signaling pathway. We have showed that this novel dendritic pro-drug can maintain the cytotoxic effect in cancer cells, while sparing healthy cells around them both in vitro and in vivo. Moreover, by embedding this pro-drug in our adhesive hydrogel (Chapter 2), we can attain local and sustained delivery, affording longer therapeutic times with higher tumor effective doses.

This platform also presents the advantage of being generalizable to other types of cancer cells by conjugation of other growth factor mimicking peptides to target other commonly overexpressed receptors in cancer cells, such as FGF2R, VEGFR or PDGFR, and conjugation of other drugs that may be more effective to specific cancer cells. With this approach, we aim to develop a universal platform that can be personalized on a patient-by-patient basis.

CHAPTER 5. Implications and Future Directions

This thesis dissertation describes the development of a novel approach to locally advanced triple negative breast cancer treatment by exploiting the powerful efficacy of currently used chemotherapeutic agents without the harmful and deleterious side effects. The means to doing so rely on two aspects. First, the chemotherapeutic agent is converted into a pro-drug type molecule, only effective under cancer-specific cues, and second, the pro-drug is released in a local manner with the aid of an adhesive hydrogel, avoiding side effects and accumulation in other organs. Beyond minimizing or even eliminating side effects, the advantages of this approach are numerous and very impactful for the field. In situ gelation of the developed adhesive hydrogel makes it injectable, hence patients would not need to undergo further surgical procedures for pro-drug depot implantation. Also, the hydrogel scaffold is biodegradable and the pro-drug is cross-linked into its structure, affording sustained release of therapeutic agent over time – patients would only need one dose in the form of an intratumoral injection every few weeks or months, based on the hydrogel formulation.

The dendritic pro-drug approach itself also presents important implications for the field of personalized cancer treatment. By using small peptides to trigger selective uptake in cancer cells, we open the possibilities for a repertoire of dendrimers conjugated to different peptides for typically overexpressed receptors, such as FGF2R, VEGFR or PDGFR. We envision a patient-by-patient point of care, where biopsies of the tumors can be analyzed for receptor expression with currently available techniques and pre-synthesized dendritic pro-drugs could be used based on the results. The same generalizable model applies to the chemotherapy agent of use, allowing to expand this approach to other types of solid tumors, such as colon, lung, cervical or ovarian cancer, amongst others. Neoadjuvant therapy is only one potential application of the approach

described here. Other uses would include preventive localized treatment after tumor surgical resection to avoid recurrence; and as palliative care for tumor size reduction in cases of mass effect (i.e. masses blocking main airways or arteries in patients with metastasized cancer). Not only is this approach generalizable in many different ways and allows for personalized medicine, but it is also translational. The dendritic pro-drug is highly stable in solution for months, which would allow hospitals to keep stocks of different dendritic pro-drugs, and be readily mixed with dextran aldehyde to form the adhesive hydrogel within seconds.

At the intersection of biomaterials science, cancer cell biology and pharmacokinetics, this dissertation sheds light on promising data in the field of cancer treatment. The immediate and most translational next steps entail pre-clinical studies to assess therapeutic effect, drug biodistribution and safety at short, medium and long term. At a more academic level, this technology could be combined with other therapeutic modalities, such as gene therapy, for dual and potentially synergistic effects over tumors. Also, biodistribution of the dendritic pro-drug alone (without the adhesive hydrogel) after systemic administration, would be of vital interest for the development of a potential selective treatment of metastatic cancer. The possibilities are endless and each and every single effort is necessary in the fight against cancer, a ruthless disease that does not differentiate age, gender or social status and that has become in the past few decades one of the worst epidemics worldwide, with over 14 million new cases per year and an estimate of almost 17,000 deaths every day. And the statistics are not optimistic – according to the WHO, the number of new cases is expected to rise about 70% over the next two decades. This thesis dissertation is my small contribution to the fight against this devastating disease, but it is just the beginning.

ANNEX I. Experimental details

Chapter 2. Development and characterization of an injectable adhesive hydrogel platform

Synthesis and Formation of Dendrimer:dextran Hydrogels

Dendrimer:dextran networks were fabricated by dissolving generation five polyamidoamine (PAMAM) dendrimers with 25% amine surface groups in water (Dendritech Inc.) and mixing with a solution of oxidized dextran. Linear dextran (18.9 g, 10 kDa) is oxidized in water with sodium periodate (17.6 g) for 5 h to create dextran aldehyde (50% oxidation of glucose rings, 2 aldehyde groups per oxidized glucose ring). The reaction mixture is dialyzed (MEMBRA-CEL Dialysis Tubing, molecular weight cutoff of 3500 Da, Viskase Companies, Inc.). The two homogeneous polymer solutions were loaded into a dual-chamber syringe equipped with a 12-step mixing tip. Dendrimer:dextran network formation occurred within seconds to minutes, following the controlled mixing of dendrimer amine and dextran aldehyde via a Schiff base reaction between the constituent reactive groups (aldehydes and amines). The time required for gelation was recorded for each formulation.

Fluorescent Dendrimer Amine

To characterize the dendrimer/ dextran morphology at the tissue–material interface as well as track gradual material release from the tissue surface, constituent dendrimer amine was labeled with fluorescein. Dendrimer amine (1 g) was dissolved in 50 mL of 0.2 M sodium carbonate buffer, followed by the addition of 0.020 g of 6-(fluorescein-5-carboxyamido) hexanoic acid (Invitrogen). The mixture was stirred at room temperature for 2 h, diluted in 100 mL of doubly distilled water, dialyzed, and lyophilized. Dendrimer amine solutions of 12.5 wt % solid content, 2% of which were fluorescently labeled, were then prepared and cross-linked with dextran aldehyde solutions in the established manner to yield fluorescent materials.

Adhesive Interface Morphology

To investigate the morphology of the interface between the adhesives and tissue surfaces, biopsied rat tissues were covered with 100 µL of fluorescently labeled dendrimer/ dextran (fluorescein-conjugated dendrimer:dextran) that was allowed to cure for 4 min. Tissue samples were then snap frozen overnight, cryosectioned (16 µm sections), and stained with propidium iodide. The morphology of the tissue–material interface was quantified as the fluorescence intensity of fluorescein at the interface using image analysis (MetaMorph, Leica Microsystems). The pore size of the bulk adhesive material was also measured using MetaMorph.

Aldehyde Affinity of Soft-Tissue Surfaces

To determine the aldehyde affinity of various soft tissues, the conjugation of aldehyde-coated fluorescent microspheres (FluoSpheres aldehyde-sulfate micro-spheres, 0.02 µm, yellow-green fluorescence (505/515), 2% solids, aldehyde-coated f-MS (Molecular Probes)) to soft-tissue surfaces was quantified. Biopsies of rat duodenum, jejunum, and ileum were prepared with equal surface area (75 mm^2) and submerged in 1 mL of 0.5% f-MS solutions for 20 min on a rocker at 37 °C. Tissue samples were thoroughly rinsed with 10 mL of PBS three times. Tissue specimens were then processed and analyzed to quantify the percent surface coverage by f-MS (Leica Microsystems, MetaMorph).

Adhesion Mechanics

The adhesion mechanics following dendrimer:dextran application to soft tissues was measured using an Instron mechanical tester. Adhesive test elements were created from a 100 µL application of dendrimer:dextran evenly distributed between two uniformly sized tissue biopsies (disks of 6 mm diameter, total test element thickness of 1 mm) of rat duodenum, jejunum, or ileum. Tissue surfaces were dry blotted with Kimwipes prior to material application. After applying

dendrimer:dextran between tissue surfaces and allowing 5 min for material polymerization, adhesive test elements were displaced at a constant rate (0.05 mm s^{-1}) and the load response was continuously recorded (200 measurements s^{-1}). Recorded loads were normalized by the test element cross-sectional area and reported as an interfacial stress response to a change in thickness.

Material Retention

To track material loss following dendrimer/ dextran adhesion to various soft tissues, 6-(fluorescein-5-carboxyami-do) hexanoic acid fluorescently labeled materials were applied to small intestinal biopsies (75 mm^2 sections). Identical volumes (50 µL) of dendrimer:dextran (G5-25-20% and D40-10-5 composition) were applied to tissue surfaces and allowed to polymerize for 5 min. Samples were then submerged in PBS at 37 °C, 50 µL aliquots were taken at 0, 0.5, 1, 1.5, 2, 3, and 4 h and diluted with 50 µL of PBS, and the material percentage weight loss was measured by fluorescence signal at 475/540 nm. In parallel, triplicates from each region of the small intestine were dry blotted at times of 0, 1, 2, 3, and 4 h, snap frozen in liquid nitrogen, and stored overnight at −80 °C. Then, tissue samples were cryosectioned (16 µm sections) and stained with propidium iodide. Tissue specimens were then processed and analyzed.

In Vitro Cytotoxicity

The in vitro cellular response to dendrimer/ dextran materials was quantified via fluorometric colorimetric assays (Cytotox-ONE homogeneous membrane integrity assay, Promega). Cultures of rat 3T3 fibroblast cells were prepared in 24-well plates using standard techniques. At 70% culture confluence, adhesive degradation byproducts predegraded for 1, 7, or 30 days (dextran solid contents of 7.5, 15 and 25% with dendrimer 12.5%) of treatment were applied directly to the cell culture plate, allowing cell exposure to adhesive byproducts. Following material application,

cultures were incubated for 24 h under standard conditions, followed by immediate analyses of the cellular response.

Subcutaneous Mouse Model

A subcutaneous implantation model of tissue response was used to evaluate the in vivo compatibility. A subcutaneous pocket was created in anesthetized SKH1 hairless mice, and a 100 μL preformed disk of dendrimer:dextran (G5-25-12.5 and D10-50-X, with X being 7.5, 15, and 25% solid contents) was introduced into the pocket. After 7 and 30 days, the mice were sacrificed and the skin and subcutaneous tissues were harvested. The samples were snap frozen in liquid nitrogen and stored at −80° until histological analysis. All experimental protocols were approved by the MIT Animal Care and Use Committee and were in compliance with NIH guidelines for animal use. Harvested tissue was cryosectioned to create 16-μm-thick sections. Hematoxylin and eosin staining was performed using standard methods. The fibrotic response was based on the morphology and was measured at multiple random locations in five images from tissue samples from each mouse. Histological slides were evaluated for their extent of inflammation using the following scores: 0, no observable change compared to the control; 1, a nearly imperceptible feature (minimal); 2, an easily identifiable or notable (mild/moderate) feature; 3, a prominent to overwhelming (marked/ severe) feature.

Statistical Analyses

Data are presented as means ± standard deviations. To take multiple comparisons into account, all statistical comparisons were performed using one way ANOVA followed by the Turkey−Kramer test using InStat software (GraphPad, San Diego, CA, USA). A p value of <0.05 was considered to denote statistical significance.

Colitis model in rabbits

Disease model of colitis was developed in rabbits (2.5 to 3 kg, male New Zealand White Rabbits, Charles River) by rectal instillation of 2,4-dinitrobenzenesulfonic acid (DNBS, Sigma-Aldrich). Colitis induction protocol was reviewed and approved by the Committee in Animal Care at MIT. DNBS in 25% ethanol (1 ml) was instilled through a urethral catheter introduced 15 cm into the rectum. Concentrations of DNBS were 150 and 75 mg/ml for severe and mild colitis induction, respectively. Animals were sacrificed 24 hours post-instillation and colon tissues excised.

Colon cancer model in rats

Male PIRC rats (350-400 g, retired breeder F344/NTac-Apcam1137, Taconic) were used as colorectal cancer model and male Sprague-Dawley rats (250 to 300 g, Charles River Laboratories) as control.

Tissue surface amine density

To determine the aldehyde affinity of colorectal healthy and diseased tissues, the conjugation of aldehyde-coated fluorescent microspheres (f-MS) (Molecular Probes) to tissue surfaces was quantified as previously described (89). For fluorescent microscopy purposes, tissue specimens were snap frozen overnight, cryosectioned (16-μm sections), and stained with propidium iodide (Vector Laboratories). For en face amine density quantification, sections were imaged in the Xenogen IVIS device with the appropriate filter sets (N=10 for colitis studies and N=3 for cancer studies). The fluorescence intensity was determined by calculating the efficiency overlying each construct, where the fluorescence intensity was corrected to eliminate tissue autofluorescence.

Adhesive interface morphology

To investigate the morphology of the interface between the adhesive and tissue surfaces, biopsied tissues were covered with 100 µL of fluorescently labeled dendrimer:dextran (dendrimer solution containing 0.5% tagged dendrimer) that was allowed to cure for 4 min. Tissue samples were snap frozen overnight, cryosectioned (12-µm sections), and stained with propidium iodide (Vector Laboratories). The morphology of the tissue–material interface was quantified as the fluorescence intensity of fluorescein at the interface using image analysis (NIS-Elements, Nikon). The interfacial pore size and length were also measured using NIS-Elements (N=5 for each tissue type and formulation).

Adhesion mechanics

The adhesion mechanics following dendrimer:dextran application to soft tissues was measured using an Instron mechanical tester, as previously described (89). Briefly, dendrimer:dextran was applied between two uniformly sized rat colonic tissue biopsies (6 ± m diameter) and allowed to polymerize for 5 min. Then, uniaxial tensile testing (Instron ElectroPuls E3000) was employed at a constant rate (0.05 mm/s) and the load response was continuously recorded to the point of macroscopic failure (N=5 for each tissue type and formulation).

Collagen-I immunofluorescence staining

Primary anti-collagen I antibody (Abcam) and Alexa Fluor 488 goat anti-mouse secondary antibody (Life Technologies) were used. For fluorescent microscopy purposes, tissue specimens were snap frozen overnight and cryosectioned (12-µm sections). Immunofluorescence staining against collagen I was performed using standard methods and tissues were stained with propidium iodide (Vector Laboratories). Collagen contents in the submucosa and basement membrane of the colon were quantified using image analysis (N=5 for each tissue type; NIS-

Elements, Nikon). For en face collagen, tissues were processed and quantified as described for en face amine density (N=10 for colitis studies and N=3 for cancer studies).

TNF-α immunofluorescence staining

Primary anti-TNF-α antibody (Santa Cruz Biotechnology) and goat anti-rabbit IgG fluorescein conjugate secondary antibody (EMD Millipore) were used. Tissue specimens processed as described for collagen immunofluorescence staining. TNF-α content in the colonic mucosa was quantified using image analysis (*N*=5 for each tissue type; NIS-Elements, Nikon).

Neutrophil immunofluorescence staining

Primary anti-MAC-387 (FITC) antibody (Abcam) was used, which recognizes the Calprotectin molecule, an intra-cytoplasmic antigen expressed by granulocytes, monocytes and tissue macrophages. Tissue specimens were processed as described for collagen immunofluorescence staining. Neutrophil recruitment to the submucosa and basement membrane of the colon was quantified using image analysis (*N*=5 for each tissue type; NIS-Elements, Nikon).

Enterotomy procedure

All animals (rats and rabbits) were randomly assigned to control and experimental groups, with the exception of experiments in which different strains were used as control and experimental groups [Sprague-Dawley rats as control compared to Pirc rats as experimental model of human familial colon cancer]. Sample size was determined by power analysis to achieve a minimum effect size of 0.5 with a *P* value of less than 0.05. Sample sizes vary between experiments and are specified in each figure caption as well as the corresponding Materials and Methods section. Enterotomy procedures were performed in both models of colitis and colon cancer, as well as in healthy controls, by creating an incision in the colon and applying sutures to the anastomoses

site with or without the application of dendrimer:dextran adhesive material. Enterotomy studies were reviewed and approved by the Committee in Animal Care at MIT. Harvested tissue was excised a week post-surgery and cryosectioned to create 10-μm-thick sections. Hematoxylin and eosin staining was performed using standard methods. Histological slides were evaluated for their extent of inflammation, serosal heterophils and serosal fibrosis using the following scores: 0, no observable change compared to the control; 1, a nearly imperceptible feature (minimal); 2, an easily identifiable or notable (mild/moderate) feature; 3, a prominent to overwhelming (marked/severe) feature (N=5 for each experimental group).

Statistical analyses

Data are presented as mean ± standard deviation. Graphs were created using GraphPad Prism software. All statistical comparisons were performed with a two-tailed t-test for independent samples using VassarStats software (Vassar College, Poughkeepsie, NY, USA). A P value of <0.05 was considered to denote statistical significance. Data marked with the same symbol (for example, single asterisk or double asterisk) represent values with statistical significance between them.

Chapter 4. Synthesis and mechanistic insights of a disease-specific dendritic pro-drug

Cell culture

MDA-MB-468 (ATCC) human breast cancer cells were cultured and maintained in L15 medium supplemented with 10% FBS and 1% penicillin/streptomycin in an environment at 37°C with 0.8% CO2.

HMEpC (Lonza) cells were cultured and maintained in MEGM medium supplemented with 100ng/ml Cholera Toxin in an environment at 37°C with 5% CO2.

Dendrimer tagging

PAMAM dendrimer (Dendritech) was fluorescently tagged with AlexaFluor-594 carboxylic acid, succinimidyl ester (Life Technologies) in carbonate buffer 50 mM. Fluorescent dendrimers were dialyzed overnight against water in a 10 kDa MWCO dialysis cassettes (Thermo Scientific) and lyophilized. Tagged dendrimers were dissolved in milli-Q water to a final concentration of 500 μM and characterized by fluorescence spectroscopy.

Dendrimer-EGF conjugation

1 mg of human recombinant EGF (Peprotech) was dissolved in 0.1M phosphate buffer with 0.15M NaCl at a concentration of 5 mg/ml and 22.2 μl of TCEP 20mM were added to reduce the disulfide bonds. The reaction crude was stirred for two hours at room temperature. Then, the reaction was dialyzed twice in a 3000 Da MWCO centrifugal filter (Centricon, Millipore) at 4000 RCFs for 15 minutes at room temperature.

In parallel, 1 mg of 500 μM fluorescently tagged PAMAM dendrimer was dissolved in 100 μl of 0.1M phosphate buffer and 831 μl of a 20 mM $SM(PEG)_2$ solution was added drop-wise. The mixture was allowed to react for 1 hour and dialyzed three times in a 10 kDa centrifugal filter (Centricon, Millipore) at 4000 RCFs for 15 minutes at room temperature.

Next, the reduced EGF solution was mixed with the dendrimer conjugated with the linker and stirred at room temperature for 4 hours. The reaction product was dialyzed overnight against PBS. The purified dendrimer-EGF conjugate's concentration was determined by fluorescence spectroscopy and the structure determined by UV-VIS spectroscopy.

Dendrimer-mimicking peptide conjugation

1 mg of 500 µM fluorescently tagged PAMAM dendrimer was dissolved in 100 µl of 0.1M phosphate buffer and 831 µl of a 20 mM $SM(PEG)_2$ solution was added drop-wise. The mixture was allowed to react for 1 hour and dialyzed twice in a 10 kDa centrifugal filter (Centricon, Millipore) at 4000 RCFs for 15 minutes at room temperature.

Next, 610 µl of peptide solution (4 mg/ml in 0.1M phosphate buffer) were added drop-wise to the dendrimer conjugated with the linker and stirred at room temperature for 4 hours. The reaction product was dialyzed overnight against PBS. The purified dendrimer-pep conjugate's concentration was determined by fluorescence spectroscopy and the structure determined by UV-VIS spectroscopy.

UV-VIS spectroscopy

Varioskan Flash Multimode Reader (Thermo Scientific, Tewksbury, MA) was used to characterize the dendrimer conjugates. Absorbance at 280 nm was used to determine the ratio of EGF or peptide to dendrimer. Because the fluorescent dendrimer also absorbs at 280 nm owing to aromatic structure of the fluorescent tag, the equation below was used to deconvolute the signals from each component (dendrimer and EGF or peptide) and obtain the EGF/peptide to dendrimer ratio (Equation 1). The individual absorption coefficients were calculated from the respective UV-VIS standard curves.

$$A_{dend-AF594-EGF,270} = A_{EGF,270} + A_{dend-AF594,270}$$

$$\varepsilon_{dend-AF594-EGF,270} \cdot C_{dend-AF594-EGF} = \varepsilon_{EGF,270} \cdot C_{EGF} + \varepsilon_{dend-AF594,270} \cdot C_{dend-AF594}$$

$$\because C_{dend-AF594-EGF} = C_{dend-AF594} = C_{dend}$$

$$\frac{C_{EGF}}{C_{dend}} = \frac{\varepsilon_{dend-AF594-EGF,270} - \varepsilon_{dend-AF594,270}}{\varepsilon_{EGF,270}}$$

DLS measurements

Samples were diluted to a concentration of 10 μM in PBS and dendrimer complexes' sizes were determined by laser dynamic light scattering (DLS) using a DynaPro Plate Reader instrument (Wyatt Technology Corp., USA).

CryoTEM

Dendrimer conjugates' solutions were purified and dissolved in milli-Q water. Samples were prepared following standard methods and analyzed using a JEOL 2100F Transmission Electron Microscope.

RT-qPCR

Cells were seeded at a density of $25 \cdot 10^4$ cells/well in a 24 well-plate and incubated at 37°C with 0.8% CO_2 for 72h. RNA was isolated using RNeasy Mini kit (QIAGEN). RNA concentration was determined by spectrophotometry using Varioskan Flash Multimode Reader (Thermo Scientific, Tewksbury, MA). For each sample, 1 μg of total RNA was used for cDNA synthesis, and the reverse transcription reaction was performed with a High Capacity cDNA Reverse Transcription kit (Applied Biosystems) according to the manufacturer's instructions. Real-time polymerase chain reaction (qPCR) was performed using TaqMan Universal Master Mix II (Applied Biosystems) and TaqMan probes (EGFR assay ID: Hs01076078_m1, GAPDH assay ID: Hs02758991_g1) in a LightCycler® 480 Real-Time PCR System (Roche).

The relative expression mRNA level of EGFR was computed and housekeeping gene glyceraldehyde 3-phosphate dehydrogenase (GAPDH) was used as the endogenous control to normalize for variations in the quality of RNA and the amount of input cDNA.

qPCR steps consisted of a pre-incubation step for 5 min at 95 °C, followed by 40 cycles of three steps: 10 s at 95 °C, 20 s at 60 °C, and 30 s at 72 °C. The threshold cycle (Ct) values were generated automatically by the LightCycler 480 software, version 1.5, and the Ct comparative method for mRNA level quantification was calculated according to the following formula:

$$mRNA_{fold} = 2^{\left[\left(Ct_{gene}^{sample} - Ct_{GAPDH}^{sample}\right) - \left(Ct_{gene}^{CTRL} - Ct_{GAPDH}^{CTRL}\right)\right]}$$

Immunostaining

MDA-MB-468 and HMEpC cells were seeded at a density of $30 \cdot 10^3$ cells/well in a 96 well-plate and incubated 24h at 37°C and 0.8% CO_2. Immunostaining against EGFR of both cell lines was performed following standard protocols. EGF receptor (D38B1) XP(R) Rabbit mAb (Cell Signaling) was used as primary antibody and Goat Anti-Rabbit IgG conjugated to Alexa Fluor 488 was used as secondary antibody. Cell nuclei were stained with DAPI. Images were acquired by fluorescence microscopy (Zeiss Axiovert 200M) and processed using ImageJ software.

Western Blot

EGFR was detected in lysates of MDA-MB-468 and HMEpC by Western Blot following standard protocols. EGF receptor (D38B1) XP(R) Rabbit mAb and Anti-rabbit IgG, HRP-linked Antibody (Cell Signaling) were used as primary and secondary antibodies, respectively. β-actin was used as control protein (Cell Signaling). Luminata Forte Western HRP Substrate (Millipore) was used as detection reagent. Protein signals were detected using ChemiDoc XRS+ Imaging System.

pEGFR was detected in lysates of MDA-MB-468 by Western Blot after 5-minutes incubation with either EGF, peptide or dendritic conjugates. Cells were lysed following standard protocols with protein and phosphatase inhibitors. pEGFR receptor (Tyr1068) antibody and Anti-rabbit IgG, HRP-linked Antibody (Cell Signaling) were used as primary and secondary antibodies,

respectively. β-actin was used as control protein (Cell Signaling). Luminata Forte Western HRP Substrate (Millipore) was used as detection reagent. Protein signals were detected using ChemiDoc XRS+ Imaging System.

Uptake experiments

a. Energy-dependent uptake mechanisms (37°C)

MDA-MB-468 and HMEpC cells were seeded in their respective growth media at a density of $30 \cdot 10^3$ cells/well in a 96 well plate and incubated 24h at 37°C. Incubation medium was removed and replaced by complete L15 medium containing either naked dendrimer or dendrimer complexes at a concentration of 10 µM. Complete L15 medium was used as a negative control. After 5-hour incubation with the dendrimer complexes, cells were washed with PBS, fixed with PFA 4% and nuclei were stained with DAPI. Images were acquired by fluorescence microscopy (Zeiss Axiovert 200M) and images were processed using ImageJ software.

b. Energy-independent uptake mechanisms (4°C)

Cells were cultured and treated as described above after 1 hour pre-incubation at 4°C. All dendrimer solutions were also cooled down to 4°C prior to incubation.

c. EGFR-mediated uptake specificity (neutralizing antibody)

MDA-MB-468 were seeded at a density of $30 \cdot 10^3$ cells/well in a 96 well plate and incubated 24h at 37°C and 0.8% CO_2. Incubation medium was removed and replaced by complete L15 culture medium containing anti-EGFR neutralizing antibody clone LA1 (Millipore) at a concentration of 30 µg/ml. Cells were incubated at 37°C for 1 hour, after which either naked dendrimer or dendrimer complexes were added to a final concentration of 10 µM. After 5h of incubation with the dendrimer complexes, cells were washed with PBS and fixed with PFA 4%. Nuclei were stained with DAPI

after fixation with 4% PFA. Images were acquired by fluorescence microscopy (Zeiss Axiovert 200M) and processed using ImageJ software.

FACS

Cells were seeded in 24 well plates at a density of $25 \cdot 10^4$ cells/well and incubated for 24h at 37°C, 0.8% CO_2. Incubation with naked dendrimer or dendrimer complexes was performed as previously described above for uptake assays maintaining the ratio of dendrimer concentration to cell density.

After 5-hour incubation, cells were washed with PBS and trypsinized. Pellets were washed with PBS-BSA 1% solution and resuspended in 500 µL of PBS-BSA 1%. Flow cytometry data was acquired in on FACS LSR-II HTS-1 (BD Biosciences) flow cytometer.

Doxorubicin aconityl synthesis

Doxorubicin-aconityl was synthesized as previously described (116). Briefly, 30 mg of doxorubicin (Cayman Chemicals) were dissolved in 3 ml of water, the pH was adjusted to 8-9 with 0.25M sodium hydroxide and the solution cooled down in a ice-water bath. Then, 40 mg of aconitic anhydride (Sigma-Aldrich) were dissolved in dioxane (Sigma-Aldrich) and added to the doxorubicin solution drop wise, while simultanerously adjusting the pH to 8-9. The mix was allowed to react for 10 minutes in the ice-water bath and then 10 more minutes at room temperature. Then, the reaction was cooled down again in an ice-water bath and the reaction product was precipitated with cold 1M hydrochloric acid for 30 minutes. The product was centrifuged for 5 minutes at 2500 RPMs and 4°C, redissolved in basic water and re-precipitated twice with cold 1M hydrochloric acid. The final product was then dissolved in DMF:DMSO (3:1 ratio) and store at -20°C for further use.

Dendritic pro-drug synthesis

Unreacted PEG-maleimide groups on the surface of the dendrimer-peptide were utilized for doxorubicin-aconityl conjugation. 0.347 µmol of dendrimer-peptide were dissolved in 1 ml of phosphate buffer 50 mM and 61 µl of 10 mg/ml cysteine (Sigma-Aldrich) were added and allowed to react for 1 hour. In parallel, 4 µmol of doxorubicin aconityl in 250 µl of DMF:DMSO (3:1 ratio) were mixed with 1 ml of 10 mg/ml EDC (Thermo Fisher) and 1 ml of 10mg/ml NHS (Thermo Fisher) for 30 minutes. Then, the activated doxorubicin-aconityl was added to the dendrimer-peptide-cysteine solution drop wise and the reaction was carried out for 1 hour. The reaction crude was purified in a PD-10 desalting column (GE Healthcare) and concentrated in a centrifugal filter (Amicon Ultra-15, EMD Millipore).

Dendritic pro-drug pH sensitivity

Dendritic pro-drug or doxorubicin-aconityl were diluted to 10 µM in OptiMEM media and the pH was adjusted to 5.5 with 1M hydrochloric acid for acidic samples. Media at pH 7.4 or 5.5 were used as controls to assess background autofluorescence. Fluorescence spectra of either the drug alone or the dendritic complex were recorded at 480 nm excitation wavelength (Varioskan) at different time-points and the intensity at the maxima (590 nm) were plotted as a bar diagram.

Dendritic pro-drug intracellular fate

MDA-MB-468 cells were seeded in 35-mm glass bottom dishes (MatTek) at a density of 500k cells per dish in their recommended media. After 24 hours, the media was switched to OptiMEM for another 24 hours. Then, cells were incubated with 10 µM dendritic pro-drug in OptiMEM media for 30 minutes and 2, 6 and 24 hours, fixed with PFA 4% and nuclei stained with DAPI. Samples were preserved with mounting media (ProLong Diamond Antifade Mountant, Thermo Fisher).

Confocal microscopy (Nikon AR1 Ultra-Fast Spectral Scanning Confocal Microscope) was employed to image the cells.

Endocytosis experiments

MDA-MB-468 cells were seeded in 35-mm glass bottom dishes (MatTek) at a density of 500k cells per dish in their recommended media. After 24 hours, the media was switched to OptiMEM for lysosome tracking samples or to OptiMEM with either early or late endosome-GFP trackers for 17 hours (Cell Light Early/Late Endosomes-GFP, BAcMam 2.0, Thermo Fisher). Then, cells were incubated with 10 μM dendritic pro-drug in OptiMEM media for 4, 8 or 24 hours and fixed with PFA 4%. Lysosome tracking samples were then incubated with lysosome tracker (LysoTracker Green DND-26) for 1 hour and washed with PBS 3 times. Samples were preserved with mounting media (ProLong Diamond Antifade Mountant, Thermo Fisher) and imaged by confocal microscopy (Nikon AR1 Ultra-Fast Spectral Scanning Confocal Microscope).

Dendritic pro-drug cancer-specific cytocidal effect

MDA-MB-468 and HMEpC were seeded in 96-well plates at a density of 20k cells per dish in their recommended media. After 24 hours, the media was switched to OptiMEM for another 24 hours. Then, cells were incubated with 10 μM dendritic pro-drug, dendrimer-peptide (without the drug) or free doxorubicin in OptiMEM media for 48 hours. Then, cells were incubated with fresh media containing a live cell tracker (CellTracker Green CMFDA Dye) for 30 minutes and then fixed with PFA 4% and nuclei stained with DAPI. Images were acquired by fluorescence microscopy (Zeiss Axiovert 200M) and live cell analysis performed with CellProfiler software.

Dextran and Dendritic pro-drug tagging

Dendritic pro-drug was labeled with either cyanine5 NHS ester (Lumiprobe) or fluorescein NHS ester (Thermo Fisher) using standard bioconjugate techniques. Dextran aldehyde was also fluorescently labeled with AlexaFluor 405 Cadaverine (Thermo Fisher). Briefly, 15 mg of dextran aldehyde were dissolved in 1.5 ml of 50mM carbonate buffer (pH 8.5) and 3 mg of tag dissolved in 300 µl of carbonate buffer were added drop wise and allowed to react for 1 hour. Then the reaction mix was cooled down in an ice-water bath and 1.5 ml of 30 mM sodium cyanoborohydrate solution were added and allowed to react for 3 hours. Then, the reaction was dialyzed through a 3000 Da MWCO centrifugal filter (Amicon Ultra-15, EMD Millipore). For all experiments described below, 5% of the dextran was fluorescently labeled.

Adhesive morphology

Fluorescently labeled dendritic pro-drug was added to a 10% (w/v) PAMAM dendrimer solution (generation 5, 25:75% amine:alcohol on the surface) to a final concentration of 100 µM. Then, the dendrimer:dendritic pro-drug solution was mixed with 10% (w/v) fluorescently labeled dextran aldehyde (10 kDa, 50% oxidation to aldehydes) to form 6-mm adhesive hydrogel pre-cured disks. Hydrogels were snap-frozen in liquid nitrogen and cryosectioned in 12 or 60 µm thickness for 2D or 3D images, respectively. Adhesive two- and three-dimensional morphology was imaged using confocal microscopy (Nikon AR1 Ultra-Fast Spectral Scanning Confocal Microscope).

Dendritic pro-drug release from the adhesive

6-mm pre-cured adhesive hydrogel disks doped with either 25 or 50 µM dendritic pro-drug were prepared as described above. Then, disks were incubated in PBS at 37C and samples were taken at different time points. Material percentage weight loss was measured by dextran aldehyde fluorescence signal at 390/425 nm and dendritic pro-drug release was also assessed

by fluorescence signal at 640/680 nm. Fluorescence signals were transformed to mass and plotted as % degradation (dextran aldehyde) or % release (dendritic pro-drug) over time.

In vivo dendritic pro-drug uptake

To create the TNBC murine model, 5-million cells in HBSS buffer were injected in the mammary fat pad of SCID mice and tumors were allowed to grow for 4-6 weeks. When tumors reached a volume of 0.1 cm^3, mice were randomly sorted into control and experimental groups. 100 µl of adhesive hydrogel doped with fluorescently labeled dendritic pro-drug was injected adjacent to the tumor and allowed to release pro-drug for 72 hours. Then, mice were euthanized and tumors excised and snap-frozen in liquid nitrogen. Tumors were cryosectioned (12 µm sections) and immunostained against EGFR to detect cancer cells. Confocal microscopy imgaes (Nikon AR1 Ultra-Fast Spectral Scanning Confocal Microscope) were analyzed for dye co-localization using ImageJ software.

REFERENCES

1. Suresh P, Batra U, Doval DC. Epidemiological and clinical profile of triple negative breast cancer at a cancer hospital in North India. Indian J Med Paediatr Oncol. 2013;34(2):89-95.
2. Boyle P. Triple-negative breast cancer: epidemiological considerations and recommendations. Ann Oncol. 2012;23 Suppl 6:vi7-12.
3. Thompson AM, Moulder-Thompson SL. Neoadjuvant treatment of breast cancer. Ann Oncol. 2012;23 Suppl 10:x231-6.
4. Langer R, Peppas NA. Advances in biomaterials, drug delivery, and bionanotechnology. AIChE Journal. 2003;49(12):2990-3006.
5. Peppas NA, Bures P, Leobandung W, Ichikawa H. Hydrogels in pharmaceutical formulations. European journal of pharmaceutics and biopharmaceutics : official journal of Arbeitsgemeinschaft fur Pharmazeutische Verfahrenstechnik eV. 2000;50(1):27-46.
6. Peppas NA, Huang Y, Torres-Lugo M, Ward JH, Zhang J. Physicochemical foundations and structural design of hydrogels in medicine and biology. Annual review of biomedical engineering. 2000;2:9-29.
7. Jeong B, Bae YH, Lee DS, Kim SW. Biodegradable block copolymers as injectable drug-delivery systems. Nature. 1997;388(6645):860-2.
8. Park TG. Temperature modulated protein release from pH/temperature-sensitive hydrogels. Biomaterials. 1999;20(6):517-21.
9. Siegel RA, Falamarzian M, Firestone BA, Moxley BC. pH-Controlled release from hydrophobic/polyelectrolyte copolymer hydrogels. Journal of Controlled Release. 1988;8(2):179-82.
10. Brannon-Peppas L, Peppas NA. Dynamic and equilibrium swelling behaviour of pH-sensitive hydrogels containing 2-hydroxyethyl methacrylate. Biomaterials. 1990;11(9):635-44.
11. Peppas NA, Keys KB, Torres-Lugo M, Lowman AM. Poly(ethylene glycol)-containing hydrogels in drug delivery. Journal of controlled release : official journal of the Controlled Release Society. 1999;62(1-2):81-7.
12. Risbud MV, Hardikar AA, Bhat SV, Bhonde RR. pH-sensitive freeze-dried chitosan-polyvinyl pyrrolidone hydrogels as controlled release system for antibiotic delivery. Journal of controlled release : official journal of the Controlled Release Society. 2000;68(1):23-30.
13. Chen SC, Wu YC, Mi FL, Lin YH, Yu LC, Sung HW. A novel pH-sensitive hydrogel composed of N,O-carboxymethyl chitosan and alginate cross-linked by genipin for protein drug delivery. Journal of controlled release : official journal of the Controlled Release Society. 2004;96(2):285-300.
14. Al-Aribe K, Knopf GK, editors. Photoresponsive hydrogel microvalve activated by bacteriorhodopsin proton pumps2010.
15. Charati MB, Lee I, Hribar KC, Burdick JA. Light-sensitive polypeptide hydrogel and nanorod composites. Small. 2010;6(15):1608-11.
16. Szabo D, Czako-Nagy II, Zrinyi M, Vertes A. Magnetic and Mossbauer Studies of Magnetite-Loaded Polyvinyl Alcohol Hydrogels. Journal of colloid and interface science. 2000;221(2):166-72.
17. Liu TY, Hu SH, Liu TY, Liu DM, Chen SY. Magnetic-sensitive behavior of intelligent ferrogels for controlled release of drug. Langmuir : the ACS journal of surfaces and colloids. 2006;22(14):5974-8.
18. Liu GZ, X; Tang T. Stimuli-Responsive of Gelatin Hydrogel Under Direct Current Electric Field. Acta Polymerica Sinica. 2003;1(3):5.
19. Hou C, Zhang Q, Li Y, Wang H. Graphene–polymer hydrogels with stimulus-sensitive volume changes. Carbon. 2012;50(5):1959-65.

20. Miyata T, Asami N, Uragami T. A reversibly antigen-responsive hydrogel. Nature. 1999;399(6738):766-9.
21. Hamidi M, Azadi A, Rafiei P. Hydrogel nanoparticles in drug delivery. Advanced drug delivery reviews. 2008;60(15):1638-49.
22. Jeong B, Bae YH, Lee DS, Kim SW. Biodegradable block copolymers as injectable drug-delivery systems. Nature. 1997;388(6645):860-2.
23. Jeong B, Bae YH, Kim SW. Drug release from biodegradable injectable thermosensitive hydrogel of PEG-PLGA-PEG triblock copolymers. Journal of controlled release : official journal of the Controlled Release Society. 2000;63(1-2):155-63.
24. Jeong B, Choi YK, Bae YH, Zentner G, Kim SW. New biodegradable polymers for injectable drug delivery systems. Journal of controlled release : official journal of the Controlled Release Society. 1999;62(1-2):109-14.
25. Bhattarai N, Gunn J, Zhang M. Chitosan-based hydrogels for controlled, localized drug delivery. Advanced drug delivery reviews. 2010;62(1):83-99.
26. Ruel-Gariepy E, Shive M, Bichara A, Berrada M, Le Garrec D, Chenite A, et al. A thermosensitive chitosan-based hydrogel for the local delivery of paclitaxel. European journal of pharmaceutics and biopharmaceutics : official journal of Arbeitsgemeinschaft fur Pharmazeutische Verfahrenstechnik eV. 2004;57(1):53-63.
27. Bhattarai N, Ramay HR, Gunn J, Matsen FA, Zhang M. PEG-grafted chitosan as an injectable thermosensitive hydrogel for sustained protein release. Journal of controlled release : official journal of the Controlled Release Society. 2005;103(3):609-24.
28. Di Silvio L, Bonfield W. Biodegradable drug delivery system for the treatment of bone infection and repair. Journal of materials science Materials in medicine. 1999;10(10/11):653-8.
29. Yaffe A, Herman A, Bahar H, Binderman I. Combined local application of tetracycline and bisphosphonate reduces alveolar bone resorption in rats. Journal of periodontology. 2003;74(7):1038-42.
30. Cascone MG, Lazzeri L, Carmignani C, Zhu Z. Gelatin nanoparticles produced by a simple W/O emulsion as delivery system for methotrexate. Journal of materials science Materials in medicine. 2002;13(5):523-6.
31. Muvaffak A, Gurhan I, Hasirci N. Prolonged cytotoxic effect of colchicine released from biodegradable microspheres. Journal of biomedical materials research Part B, Applied biomaterials. 2004;71(2):295-304.
32. Cai S, Liu Y, Zheng Shu X, Prestwich GD. Injectable glycosaminoglycan hydrogels for controlled release of human basic fibroblast growth factor. Biomaterials. 2005;26(30):6054-67.
33. Mann BK, Gobin AS, Tsai AT, Schmedlen RH, West JL. Smooth muscle cell growth in photopolymerized hydrogels with cell adhesive and proteolytically degradable domains: synthetic ECM analogs for tissue engineering. Biomaterials. 2001;22(22):3045-51.
34. Mann BK, West JL. Cell adhesion peptides alter smooth muscle cell adhesion, proliferation, migration, and matrix protein synthesis on modified surfaces and in polymer scaffolds. Journal of biomedical materials research. 2002;60(1):86-93.
35. Luo Y, Shoichet MS. A photolabile hydrogel for guided three-dimensional cell growth and migration. Nature materials. 2004;3(4):249-53.
36. Lutolf MP, Raeber GP, Zisch AH, Tirelli N, Hubbell JA. Cell-Responsive Synthetic Hydrogels. Advanced Materials. 2003;15(11):888-92.
37. Schukur L, Zorlutuna P, Cha JM, Bae H, Khademhosseini A. Directed differentiation of size-controlled embryoid bodies towards endothelial and cardiac lineages in RGD-modified poly(ethylene glycol) hydrogels. Advanced healthcare materials. 2013;2(1):195-205.
38. Mehdizadeh M, Yang J. Design strategies and applications of tissue bioadhesives. Macromolecular bioscience. 2013;13(3):271-88.

39. Oliva N, Shitreet S, Abraham E, Stanley B, Edelman ER, Artzi N. Natural tissue microenvironmental conditions modulate adhesive material performance. Langmuir : the ACS journal of surfaces and colloids. 2012;28(43):15402-9.
40. Artzi N, Shazly T, Crespo C, Ramos AB, Chenault HK, Edelman ER. Characterization of star adhesive sealants based on PEG/dextran hydrogels. Macromol Biosci. 2009;9(8):754-65.
41. Wang T, Nie J, Yang D. Dextran and gelatin based photocrosslinkable tissue adhesive. Carbohydrate polymers. 2012;90(4):1428-36.
42. Wang T, Mu X, Li H, Wu W, Nie J, Yang D. The photocrosslinkable tissue adhesive based on copolymeric dextran/HEMA. Carbohydrate polymers. 2013;92(2):1423-31.
43. Mehdizadeh M, Weng H, Gyawali D, Tang L, Yang J. Injectable citrate-based mussel-inspired tissue bioadhesives with high wet strength for sutureless wound closure. Biomaterials. 2012;33(32):7972-83.
44. Xu J, Soliman GM, Barralet J, Cerruti M. Mollusk glue inspired mucoadhesives for biomedical applications. Langmuir : the ACS journal of surfaces and colloids. 2012;28(39):14010-7.
45. Shoichet MS, Zahir T, Ballios B, Van DKD, Cooke M. Injectable polymer composition for use as a cell delivery vehicle. Google Patents; 2012.
46. Unterman SA, Marcus NA, Elisseeff JH. Injectable Polymers. Biodegradable Polymers in Clinical Use and Clinical Development: John Wiley & Sons, Inc.; 2011. p. 631-64.
47. Cam C, Segura T. Matrix-based gene delivery for tissue repair. Current opinion in biotechnology. 2013;24(5):855-63.
48. Orive G, Santos E, Pedraz JL, Hernandez RM. Application of cell encapsulation for controlled delivery of biological therapeutics. Advanced drug delivery reviews. 2013.
49. Armentano I, Fortunati E, Mattioli S, Rescignano N, Kenny JM. Biodegradable composite scaffolds: a strategy to modulate stem cell behaviour. Recent patents on drug delivery & formulation. 2013;7(1):9-17.
50. Saiz E, Zimmermann EA, Lee JS, Wegst UG, Tomsia AP. Perspectives on the role of nanotechnology in bone tissue engineering. Dental materials : official publication of the Academy of Dental Materials. 2013;29(1):103-15.
51. Orlando G, Bendala JD, Shupe T, Bergman C, Bitar KN, Booth C, et al. Cell and organ bioengineering technology as applied to gastrointestinal diseases. Gut. 2013;62(5):774-86.
52. Brown BN, Badylak SF. Expanded applications, shifting paradigms and an improved understanding of host-biomaterial interactions. Acta biomaterialia. 2013;9(2):4948-55.
53. Oliva N, Carcole M, Beckerman M, Seliktar S, Hayward A, Stanley J, et al. Regulation of dendrimer/dextran material performance by altered tissue microenvironment in inflammation and neoplasia. Sci Transl Med. 2015;7(272):272ra11.
54. Tzur-Balter A, Shatsberg Z, Beckerman M, Segal E, Artzi N. Mechanism of erosion of nanostructured porous silicon drug carriers in neoplastic tissues. Nat Commun. 2015;6:6208.
55. Artzi N, Oliva N, Puron C, Shitreet S, Artzi S, bon Ramos A, et al. In vivo and in vitro tracking of erosion in biodegradable materials using non-invasive fluorescence imaging. Nat Mater. 2011;10(9):704-9.
56. Hanahan D, Weinberg RA. The hallmarks of cancer. Cell. 2000;100(1):57-70.
57. Junttila MR, de Sauvage FJ. Influence of tumour micro-environment heterogeneity on therapeutic response. Nature. 2013;501(7467):346-54.
58. Mi Y, Mu C, Wolfram J, Deng Z, Hu TY, Liu X, et al. A Micro/Nano Composite for Combination Treatment of Melanoma Lung Metastasis. Adv Healthc Mater. 2016;5(8):936-46.
59. Burga LN, Hu H, Juvekar A, Tung NM, Troyan SL, Hofstatter EW, et al. Loss of BRCA1 leads to an increase in epidermal growth factor receptor expression in mammary epithelial cells, and epidermal growth factor receptor inhibition prevents estrogen receptor-negative cancers in BRCA1-mutant mice. Breast Cancer Res. 2011;13(2):R30.

60. Jiang W, Kim BY, Rutka JT, Chan WC. Nanoparticle-mediated cellular response is size-dependent. Nature nanotechnology. 2008;3(3):145-50.
61. Tomalia DA, Naylor AM, Goddard WA. Starburst Dendrimers: Molecular-Level Control of Size, Shape, Surface Chemistry, Topology, and Flexibility from Atoms to Macroscopic Matter. Angewandte Chemie International Edition in English. 1990;29(2):138-75.
62. Haensler J, Szoka FC, Jr. Polyamidoamine cascade polymers mediate efficient transfection of cells in culture. Bioconjugate chemistry. 1993;4(5):372-9.
63. Lee CC, MacKay JA, Frechet JM, Szoka FC. Designing dendrimers for biological applications. Nature biotechnology. 2005;23(12):1517-26.
64. Tomalia DA, Reyna LA, Svenson S. Dendrimers as multi-purpose nanodevices for oncology drug delivery and diagnostic imaging. Biochemical Society transactions. 2007;35(Pt 1):61-7.
65. Nanjwade BK, Bechra HM, Derkar GK, Manvi FV, Nanjwade VK. Dendrimers: emerging polymers for drug-delivery systems. European journal of pharmaceutical sciences : official journal of the European Federation for Pharmaceutical Sciences. 2009;38(3):185-96.
66. Boas U, Heegaard PM. Dendrimers in drug research. Chemical Society reviews. 2004;33(1):43-63.
67. Fischer D, Li Y, Ahlemeyer B, Krieglstein J, Kissel T. In vitro cytotoxicity testing of polycations: influence of polymer structure on cell viability and hemolysis. Biomaterials. 2003;24(7):1121-31.
68. Jevprasesphant R, Penny J, Jalal R, Attwood D, McKeown NB, D'Emanuele A. The influence of surface modification on the cytotoxicity of PAMAM dendrimers. International journal of pharmaceutics. 2003;252(1-2):263-6.
69. Duncan R, Izzo L. Dendrimer biocompatibility and toxicity. Advanced drug delivery reviews. 2005;57(15):2215-37.
70. Pearson RMBJWHS. Multifuncional Dendritic Nanocarriers: The Architecture and Applications in Targeted Drug Delivery. In: Yeo Y, editor. Nanoparticle Drug Delivery Systems: Wiley; 2013. p. 324.
71. Saovapakhiran A, D'Emanuele A, Attwood D, Penny J. Surface modification of PAMAM dendrimers modulates the mechanism of cellular internalization. Bioconjug Chem. 2009;20(4):693-701.
72. Taratula O, Garbuzenko OB, Kirkpatrick P, Pandya I, Savla R, Pozharov VP, et al. Surface-engineered targeted PPI dendrimer for efficient intracellular and intratumoral siRNA delivery. Journal of controlled release : official journal of the Controlled Release Society. 2009;140(3):284-93.
73. Patil ML, Zhang M, Taratula O, Garbuzenko OB, He H, Minko T. Internally cationic polyamidoamine PAMAM-OH dendrimers for siRNA delivery: effect of the degree of quaternization and cancer targeting. Biomacromolecules. 2009;10(2):258-66.
74. Hermanson GT. Bioconjugate techniques. San Diego: Academic Press; 1996. xxv, 785 p. p.
75. Togo Y, Takahashi K, Saito K, Kiso H, Huang B, Tsukamoto H, et al. Aldehyded Dextran and ε-Poly(L-lysine) Hydrogel as Nonviral Gene Carrier. Stem Cells International. 2013;2013:5.
76. Kazusa H, Nakasa T, Shibuya H, Ohkawa S, Kamei G, Adachi N, et al. Strong adhesiveness of a new biodegradable hydrogel glue, LYDEX, for use on articular cartilage. Journal of applied biomaterials & functional materials. 2013;11(3):e180-6.
77. Chang CY, Chan AT, Armstrong PA, Luo HC, Higuchi T, Strehin IA, et al. Hyaluronic acid-human blood hydrogels for stem cell transplantation. Biomaterials. 2012;33(32):8026-33.
78. Artzi N, Shazly T, Baker AB, Bon A, Edelman ER. Aldehyde-amine chemistry enables modulated biosealants with tissue-specific adhesion. Adv Mater. 2009;21(32-33):3399-403.

79. Artzi N, Zeiger A, Boehning F, bon Ramos A, Van Vliet K, Edelman ER. Tuning adhesion failure strength for tissue-specific applications. Acta biomaterialia. 2011;7(1):67-74.
80. Shazly TM, Artzi N, Boehning F, Edelman ER. Viscoelastic adhesive mechanics of aldehyde-mediated soft tissue sealants. Biomaterials. 2008;29(35):4584-91.
81. Laschke MW, Vollmar B, Menger MD. The dorsal skinfold chamber: window into the dynamic interaction of biomaterials with their surrounding host tissue. Eur Cell Mater. 2011;22:147-64; discussion 64-7.
82. Sun C, Waite JH. Mapping chemical gradients within and along a fibrous structural tissue, mussel byssal threads. J Biol Chem. 2005;280(47):39332-6.
83. Messersmith PB. Materials science. Multitasking in tissues and materials. Science. 2008;319(5871):1767-8.
84. Mahdavi A, Ferreira L, Sundback C, Nichol JW, Chan EP, Carter DJ, et al. A biodegradable and biocompatible gecko-inspired tissue adhesive. Proc Natl Acad Sci U S A. 2008;105(7):2307-12.
85. Stewart RJ, Ransom TC, Hlady V. Natural Underwater Adhesives. J Polym Sci B Polym Phys. 2011;49(11):757-71.
86. Lee BP, Messersmith PB, Israelachvili JN, Waite JH. Mussel-Inspired Adhesives and Coatings. Annu Rev Mater Res. 2011;41:99-132.
87. Storkholm JH, Villadsen GE, Jensen SL, Gregersen H. Mechanical properties and collagen content differ between isolated guinea pig duodenum, jejunum, and distal ileum. Dig Dis Sci. 1998;43(9):2034-41.
88. Khandare J, Calderon M, Dagia NM, Haag R. Multifunctional dendritic polymers in nanomedicine: opportunities and challenges. Chem Soc Rev. 2012;41(7):2824-48.
89. Oliva N, Shitreet S, Abraham E, Stanley B, Edelman ER, Artzi N. Natural tissue microenvironmental conditions modulate adhesive material performance. Langmuir. 2012;28(43):15402-9.
90. Graham MF, Diegelmann RF, Elson CO, Lindblad WJ, Gotschalk N, Gay S, et al. Collagen content and types in the intestinal strictures of Crohn's disease. Gastroenterology. 1988;94(2):257-65.
91. Morimoto Y, Tanaka K, Toiyama Y, Inoue Y, Araki T, Uchida K, et al. Intravital three-dimensional dynamic pathology of experimental colitis in living mice using two-photon laser scanning microscopy. Journal of gastrointestinal surgery : official journal of the Society for Surgery of the Alimentary Tract. 2011;15(10):1842-50.
92. Cury DB, Mizsputen SJ, Versolato C, Miiji LO, Pereira E, Delboni MA, et al. Serum calprotectin levels correlate with biochemical and histological markers of disease activity in TNBS colitis. Cellular immunology. 2013;282(1):66-70.
93. Mowat AM, Bain CC. Mucosal macrophages in intestinal homeostasis and inflammation. Journal of innate immunity. 2011;3(6):550-64.
94. Lenglet S, Mach F, Montecucco F. Role of matrix metalloproteinase-8 in atherosclerosis. Mediators of inflammation. 2013;2013:659282.
95. Oliva N, Unterman S, Zhang Y, Conde J, Song HS, Artzi N. Personalizing Biomaterials for Precision Nanomedicine Considering the Local Tissue Microenvironment. Adv Healthc Mater. 2015;4(11):1584-99.
96. Yatvin MB, Kreutz W, Horwitz BA, Shinitzky M. pH-sensitive liposomes: possible clinical implications. Science. 1980;210(4475):1253-5.
97. Wade RJ, Bassin EJ, Rodell CB, Burdick JA. Protease-degradable electrospun fibrous hydrogels. Nat Commun. 2015;6:6639.
98. Andresen TL, Davidsen J, Begtrup M, Mouritsen OG, Jorgensen K. Enzymatic release of antitumor ether lipids by specific phospholipase A2 activation of liposome-forming prodrugs. J Med Chem. 2004;47(7):1694-703.

99. Andresen TL, Jensen SS, Kaasgaard T, Jorgensen K. Triggered activation and release of liposomal prodrugs and drugs in cancer tissue by secretory phospholipase A2. Curr Drug Deliv. 2005;2(4):353-62.
100. Ma Z, Taylor JS. Nucleic acid-triggered catalytic drug release. Proc Natl Acad Sci U S A. 2000;97(21):11159-63.
101. Torchilin V. Tumor delivery of macromolecular drugs based on the EPR effect. Advanced drug delivery reviews. 2011;63(3):131-5.
102. Peer D, Karp JM, Hong S, Farokhzad OC, Margalit R, Langer R. Nanocarriers as an emerging platform for cancer therapy. Nature nanotechnology. 2007;2(12):751-60.
103. Brannon-Peppas L, Blanchette JO. Nanoparticle and targeted systems for cancer therapy. Advanced drug delivery reviews. 2004;56(11):1649-59.
104. Xie J, Liu G, Eden HS, Ai H, Chen X. Surface-engineered magnetic nanoparticle platforms for cancer imaging and therapy. Accounts of chemical research. 2011;44(10):883-92.
105. Nam HY, Nam K, Hahn HJ, Kim BH, Lim HJ, Kim HJ, et al. Biodegradable PAMAM ester for enhanced transfection efficiency with low cytotoxicity. Biomaterials. 2009;30(4):665-73.
106. Wen Y, Guo Z, Du Z, Fang R, Wu H, Zeng X, et al. Serum tolerance and endosomal escape capacity of histidine-modified pDNA-loaded complexes based on polyamidoamine dendrimer derivatives. Biomaterials. 2012;33(32):8111-21.
107. Tian WM, YQ. Insights into the endosomal escape mechanism via investigation of dendrimer-membrane interactions. Soft Matter. 2012;8(23):6378-84.
108. Quintana A, Raczka E, Piehler L, Lee I, Myc A, Majoros I, et al. Design and function of a dendrimer-based therapeutic nanodevice targeted to tumor cells through the folate receptor. Pharmaceutical research. 2002;19(9):1310-6.
109. Thomas TP, Shukla R, Kotlyar A, Liang B, Ye JY, Norris TB, et al. Dendrimer-epidermal growth factor conjugate displays superagonist activity. Biomacromolecules. 2008;9(2):603-9.
110. She W, Pan D, Luo K, He B, Cheng G, Zhang C, et al. PEGylated Dendrimer-Doxorubicin Cojugates as pH-Sensitive Drug Delivery Systems: Synthesis and In Vitro Characterization. Journal of biomedical nanotechnology. 2015;11(6):964-78.
111. He X, Alves CS, Oliveira N, Rodrigues J, Zhu J, Banyai I, et al. RGD peptide-modified multifunctional dendrimer platform for drug encapsulation and targeted inhibition of cancer cells. Colloids and surfaces B, Biointerfaces. 2015;125:82-9.
112. van Dongen MA, Rattan R, Silpe J, Dougherty C, Michmerhuizen NL, Van Winkle M, et al. Poly(amidoamine) dendrimer-methotrexate conjugates: the mechanism of interaction with folate binding protein. Molecular pharmaceutics. 2014;11(11):4049-58.
113. Nicholson RI, Gee JM, Harper ME. EGFR and cancer prognosis. European journal of cancer. 2001;37 Suppl 4:S9-15.
114. Han CY, Yue LL, Tai LY, Zhou L, Li XY, Xing GH, et al. A novel small peptide as an epidermal growth factor receptor targeting ligand for nanodelivery in vitro. International journal of nanomedicine. 2013;8:1541-9.
115. von Minckwitz G, Martin M. Neoadjuvant treatments for triple-negative breast cancer (TNBC). Ann Oncol. 2012;23 Suppl 6:vi35-9.
116. Shen WC, Ryser HJ. cis-Aconityl spacer between daunomycin and macromolecular carriers: a model of pH-sensitive linkage releasing drug from a lysosomotropic conjugate. Biochem Biophys Res Commun. 1981;102(3):1048-54.
117. Kakinoki A, Kaneo Y, Ikeda Y, Tanaka T, Fujita K. Synthesis of poly(vinyl alcohol)-doxorubicin conjugates containing cis-aconityl acid-cleavable bond and its isomer dependent doxorubicin release. Biol Pharm Bull. 2008;31(1):103-10.
118. Hu FQ, Zhang YY, You J, Yuan H, Du YZ. pH triggered doxorubicin delivery of PEGylated glycolipid conjugate micelles for tumor targeting therapy. Mol Pharm. 2012;9(9):2469-78.

119. Zhu S, Hong M, Zhang L, Tang G, Jiang Y, Pei Y. Erratum to: PEGylated PAMAM Dendrimer-Doxorubicin Conjugates: In Vitro Evaluation and In Vivo Tumor Accumulation. Pharm Res. 2010;27(9):2030.
120. Pearson RB, JW.; Hong, S. Multifunctional Dendritic Nanocarriers: The Architecture and Applications in Targeted Drug Delivery. In: Yeo Y, editor. Nanoparticulate Drug Delivery Systems: Strategies, Technologies, and Applications: Wiley; 2013.
121. Karukstis KK, Thompson EH, Whiles JA, Rosenfeld RJ. Deciphering the fluorescence signature of daunomycin and doxorubicin. Biophys Chem. 1998;73(3):249-63.
122. Guicciardi ME, Leist M, Gores GJ. Lysosomes in cell death. Oncogene. 2004;23(16):2881-90.
123. Sheng Y, Xu J, You Y, Xu F, Chen Y. Acid-Sensitive Peptide-Conjugated Doxorubicin Mediates the Lysosomal Pathway of Apoptosis and Reverses Drug Resistance in Breast Cancer. Mol Pharm. 2015;12(7):2217-28.